Ollscoil Chathair
Bhaile Átha Cliath
Dublin City University

Dublin City University

School of Physical Sciences

Fabrication and Characterisation of Polymer Brushes for the use in Area Selective Deposition

Caitlin McFeely B.Sc.

Thesis submitted for the award of Doctor of Philosophy (Ph.D.)

August 2023

Supervised by Dr. Robert O'Connor & Professor Enda McGlynn

Declaration

I hereby certify that this material, which I now submit for assessment on the programme of study leading to the award of Ph.D. is entirely my own work, and that I have exercised reasonable care to ensure that the work is original, and does not to the best of my knowledge breach any law of copyright, and has not been taken from work of others save and to the extent that such work has been cited and acknowledged within the text of my work.

Signed: Caitlin mc Feely (Caitlin McFeely, Candidate)

ID No.:15401362

Date: 22-08-23

Acknowledgments

I would firstly like to thank my Mam, Brona McFeely, who always supported me in my dream to pursue a degree in science and then to further my education through the completion of this PhD. I would also like to thank the rest of my family and close friends – especially Kate Wood and Brian Dillion for their support over the last few years of my research.

This was a big project and because of that I was fortunate to work with a large number of passionate and talented researchers. This includes all the collaborators in the AMBER centre, particularly Pravind Yadav, whom without his knowledge of polymer chemistry and polymer fabrication, the experiments conducted within this work would never have been completed. I would also like to thank the assistance from Intel, especially to Matt Shaw and Jennifer McKenna. I was also very fortunate to work with the beamline scientists Conan Weiland and Joe Woicik at Brookhaven National Laboratory.

I would also like to thank all the amazing people I got to work with in DCU. This especially goes to my colleagues and friends Shane, Feljin and Darragh. You have all made this time so much more fun and enjoyable as well as providing invaluable help with my research. I would also like to show my gratitude to Matthew Snelgrove, who's help made this research possible. To Kyle, Pat and Des, whose ability to fix any and all problems thrown at them was so important for this work. I would also like to thank Greg Hughes for his help and guidance over the course of this work.

Lastly, I would especially like to thank my supervisors Dr. Robert O'Connor and Prof. Enda McGlynn, who gave me the opportunity to conduct this research as well as giving me the help and guidance needed to get to this stage.

Finally, I would like to acknowledge Science Foundation Ireland and Intel for the financial support of this work.

Table of Contents

List of Figures

List of Abbreviations

AFM : Atomic Force Microscopy
ALD : Atomic Layer Deposition
ALE : Atomic Layer Epitaxy
AMBER : Advanced Materials and BioEngineering Research
ASD : Area Selective Deposition
ATR : Attenuated Total Reflection
BCP : Block Copolymer
CD : Critical Dimension
CVD : Chemical Vapour Deposition
DCU : Dublin City University
DP : Degree of Polymerisation
EUV : Extreme Ultraviolet (Lithography)
FTIR : Fourier Transform Infrared Spectroscopy
FWHM : Full Width Half Maximum
GA-ATR-FTIR : Grazing Angle Attenuated Total Reflection FTIR
HAXPES : Hard X-Ray Photoelectron Spectroscopy
IC : Integrated Circuit
ICP : Inductively Coupled Plasma
IMFP : Inelastic Mean Free Path
IR : Infrared
MOSFET : Metal Oxide Field-Effect Transistor
P2VP : Poly-2-Vinyl Pyridine
PDI : Polydispersity Index
PEALD : Plasma Enhanced Atomic Layer Deposition
PEO : Polyethylene oxide
PMMA : Poly(methyl methacrylate)
PS : Polystyrene
RMS : Root Mean Square
SAM : Self Assembled Monolayer
SCCM : Standard Cubic Centimetre per Minute
TMA : Triethylaluminium
UHV : Ultra High Vacuum
UV : Ultraviolet
VPI : Vapour Phase Infiltration
XPS : X-Ray Photoelectron Spectroscopy
XRR : X-Ray Reflectivity

Publications Arising from this Work

1. **Effect of Polymer Thickness and Molecular Weight on its ability to be Infiltrated Via a Vapour Phase Process (Chapter 3 & Chapter 4)**
   C. McFeely, M. Snelgrove, D. O'Neill, S. O' Donnell, F. Jose, C. Weiland, G. Hughes, P. Yadav, J.C Woicik, M. A Morris, E. McGlynn, R. O'Connor, *In Preparation.*

2. **Rapid Area Deactivation for Blocking Atomic Layer Deposition Porcesses using Polystyrene Brush Layers (Chapter 3 & Chapter 4)**
   C. McFeely, M. Snelgrove, K.Shiel, G. Hughes, P. Yadav, R. Lundy, M. A Morris, E. McGlynn, R. O'Connor, *J.Mater.Chem.C,* 2022, **10**, 7476-7484.

Contributing Publications

1. **Fabrication of sub-5 nm Uniform Zirconium Oxide Films on Corrugated Copper Substrates by a Scalable Polymer Brush Assisted Deposition Method**
   P. Yadav, S. Singh, N. Prochukhan, A, Davó- Quiñonero, J. Conway, R. Gatensby, S. C Padmanabhan, M. Snelgrove, C. McFeely, K. Shiel, R. O'Connor, E. McGlynn, M. Turner, R. Lundy, M. A Morris, *Appl. Surf. Sci.*, 2023, **627**, 157329.

2. **Growth Chemistry of Cobalt Nitride by Plasma Enhanced Atomic Layer Deposition**
   S O'Donnell, M Snelgrove, K Shiel, C Weiland, G Hughes, J Woicik, D O'Neill, F Jose, C McFeely, R O'Connor, *Mater. Res. Express,* 2022, **9**, 106402.

3. **Growth Chemistry and Electrical Performance of Ultrathin Alumina Formed by Area Selective Vapour Phase Infiltration**
   M. Snelgrove, C. McFeely, G. Hughes, C. Weiland, J.C. Woicik, K. Shiel, P.G. Mani Gonzalez, C. Ornelas, O. Solis-Canto, K. Cherkaoui, P. K Hurley, P. Yadav, M.A. Morris, E. McGlynn, and R. O'Connor, *Microelectron. Eng.,* 2022, **266,** 111888.

4. **Fabrication of High-k Dielectric Metal Oxide Films on Topographically Patterned Substrates: Polymer Brush-Mediated Depositions**
   P. Yadav, R. Gatensby, N. Prochukhan, S. Padmanabham, A, Davó- Quiñonero, P. Darragh, R. Senthamaraikannan, B. Murphy, M. Snelgrove, C. McFeely, S. Singh, J. Conway, R. O'Connor, E. McGlynn, R. Lundy, and M. A. Morris. *ACS Appl. Mater. Interfaces,* 2022, **28,** 32729 – 32737.

5. **Titanium infiltration into ultrathin PMMA brushes**
   P. G. Mani-Gonzalez, C. McFeely, M. Snelgrove, K. Shiel, J. A. Hernandez Marquez and R. O'Connor, *J. Vac. Sci. Technol. A*, 2021, **39**, 040403.

6. **Analysing trimethylaluminum infiltration into polymer brushes using a scalable area selective vapor phase process**
   M. Snelgrove, C. McFeely, K. Shiel, G. Hughes, P. Yadav, C. Weiland, J. C. Woicik, P. G. Mani-Gonzalez, R. Lundy, M. A. Morris, E. McGlynn and R. O'Connor, *Mater. Adv.*, 2021, **2**, 769–781.

7. **Precise Definition of a "Monolayer Point" in Polymer Brush Films for Fabricating Highly Coherent TiO2 Thin Films by Vapor-Phase Infiltration**
   R. Lundy, P. Yadav, N. Prochukhan, E. C. Giraud, T. F. O'Mahony, A. Selkirk, E. Mullen, J. Conway, M. Turner, S. Daniels, P. G. Mani-Gonzalez, M. Snelgrove, J. Bogan, C. McFeely, R. O'Connor, E. McGlynn, G. Hughes, C. Cummins and M. A. Morris, *Langmuir*, 2020, **36**, 12394–12402.

8. **Aluminium oxide formation via atomic layer deposition using a polymer brush mediated selective infiltration approach**
   M. Snelgrove, C. McFeely, P. G. Mani-Gonzalez, K. Lahtonen, R. Lundy, G. Hughes, M. Valden, E. McGlynn, P. Yadav, J. Saari, M. A. Morris and R. O'Connor, *Appl. Surf. Sci.*, 2020, **515**, 145987.

Conference Proceedings*

1. **Polystyrene Brush Deactivation Layers for Area Selective Atomic Layer Deposition**
   C. McFeely, M. Snelgrove, K. Shiel, G. Hughes, P. Yadav, R. Lundy, M. A Morris, E. McGlynn and R. O'Connor
   AVS 22nd International Conference on Atomic Layer Deposition (ALD 2021) featuring the 9th International Atomic Layer Etching Workshop (ALE 2021), Oral Presentation, Ghent, 2022.

2. **Plasma Enhanced Atomic Layer Deposition of NiO from Nickelocene and Oxygen Precursors: Growth Characteristics and Photochemical Performance.**
   S. O'Donnell, D. O'Neill, K. Shiel, M. Snelgrove, F. Jose, C. McFeely and R. O'Connor
   AVS 22nd International Conference on Atomic Layer Deposition (ALD 2021) featuring the 9th International Atomic Layer Etching Workshop (ALE 2021), Poster Presentation, Ghent, 2022.

3. **Investigation into the effect of Molecular Weight on the thickness of Polymer Brush Monolayers Suitable for Area Selective Deposition**
   C. McFeely, M. Snelgrove, R. Lundy, P. Yadav, P.G. Mani-Gonzalez, G. Hughes, M.A. Morris, E. McGlynn and R. O'
   5th Area Selective Deposition Workshop, Poster Presentation Virtual Meeting, 2021.

4. **Thermal and Plasma Enhanced Atomic Layer Deposition of Ultrathin TiO_2 on Silicon from Amide and Alkoxide Precursors: Growth Characteristics and Photoelectrochemical Performance.**
   S. O'Donnell, F. Jose, K. Shiel, M. Snelgrove, C. McFeely, E. McGill and R. O'Connor.
   AVS Atomic Layer Deposition Symposium, Oral Presentation, Virtual Meeting 2020.

*Underscore Denotes Speaker

Fabrication and Characterisation of Polymer Brushes for the use in Area Selective Deposition

Caitlin McFeely

Abstract

With the constant increasing demand for faster and more efficient electronic devices, the requirement for smaller integrated circuits has grown exponentially. The current method of fabrication for these devices, known as photolithography, employs a ‘top-down’ approach using light and masks for the patterning of substrate surfaces. This method, however, is reaching its size limits and has become extremely costly to carry out. Research into the fabrication of polymer brushes for the use in area selective deposition is vital for the understanding of ‘bottom up’ lithography techniques, such as block copolymer lithography. Such methods rely on the self-assembly of polymers containing active and inactive regions and are being proposed as an alternative to the current ‘top-down’ methods used for the manufacturing of electronic devices. These self-assembled polymer patterns can be exposed to infiltrating materials via a vapour phase process thus allowing for the infiltration of the active regions while blocking deposition in the inactive areas. A major part of these fields is investigating the polymer materials that will either accept or block infiltration by different species such as metals. This work looks at developing fabrication techniques of polymer brushes with a focus on increasing the overall thickness. It then goes on to investigate the infiltration of different polymers as well as looking at the effect that thickness has on a polymers infiltration and blocking mechanisms using hard X-Ray photoelectron spectroscopy as the core analysis method alongside techniques such as ellipsometry, atomic force microscopy and X-Ray reflectivity.

1 Introduction

1.1 Current Integrated Circuit Fabrication Challenges

1.1.1 Moore's Law

When discussing the topic of area selective deposition (ASD) for the improvement of integrated circuit (IC) fabrication, we must first begin by discussing Moore's Law. In 1965, Gordon Moore made a prediction based on the manufacturing trends and computational needs at the time; he theorised that the number of transistors on an IC chip would double every year [1]. This held true until 1975, when the theory was revised, and the amount of time between each doubling was increased from one to two years [2]. Over the course of the last 50 years, this forecast became the gold standard in the semiconductor industry as the number of transistors increased at the predicted rate which was a driving force for research and innovation. Figure 1.1 depicts Moore's Law and how it has developed since its conception.

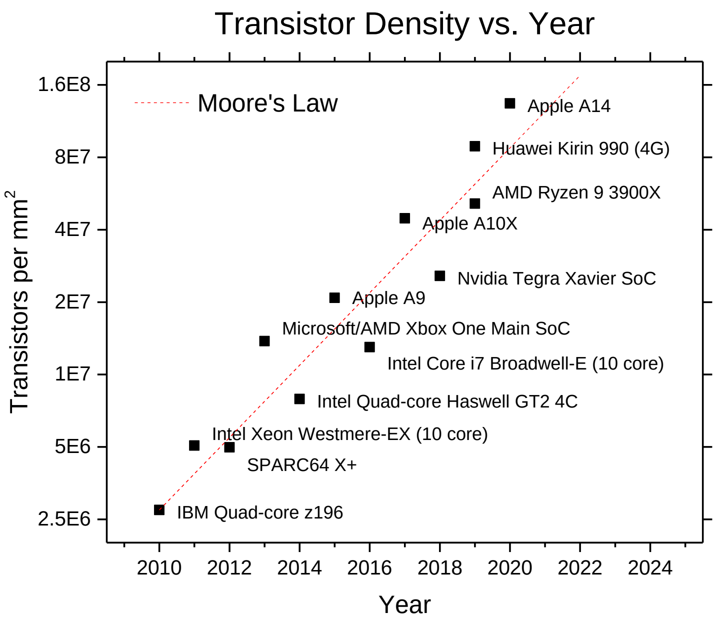

Figure 1.1 Plot illustrating a selection of microprocessors from the period 2010 – 2020. The dashed line represents Moore's law showing the transistor density for the processors doubling every two years [3].

One of the main driving factors for this miniaturisation was that with a larger amount of transistors, devices were capable of having higher processing powers with increased energy efficiency [4]. This development not only enhanced existing industries and increased productivity but also created new industries empowered by cheap and powerful computing [5]. While there are many advantages to these scaled-down ICs there also comes the disadvantage of increased fabrication costs. With this continued exponential decrease in chip size there has also been an exponential increase in the required financial investments. Current fabrication techniques, such as optical lithography, have begun to reach their size limits. The wavelengths required to create the desired dimensions are difficult and costly to produce meaning these methods are becoming unviable. There are many fields of research trying to find new fabrication techniques, two examples of these, which are the focus of this work, are ASD and block copolymer (BCP) lithography.

1.1.2 The Integrated Circuit

Put simply, an IC is a miniaturized electronic circuit that is the main component of all computing devices and one of the most fundamental products fabricated by the semiconductor manufacturing industry. They consist of multiple interconnected electronic components such as transistors, diodes, capacitors, and resistors. These are built upon a thin substrate of semiconductor material, typically silicon, and as a whole, the entire IC diameter is on the order of millimetres while the individual components on the chips are on the nanometre scale [6,7]. The small size of the chip and its parts allows not only for smaller computational devices but also allows for enhanced performance by the IC, in terms of processing speed for example.

One of the most common components seen within an IC is the metal oxide semiconductor field-effect transistor (MOSFET). They are typically used as a switch or an amplifier within the circuit [8]. MOSFETs consist of a drain, gate, source, and body terminal [9]. The arrangement of these terminals can be seen below in Figure 1.2.

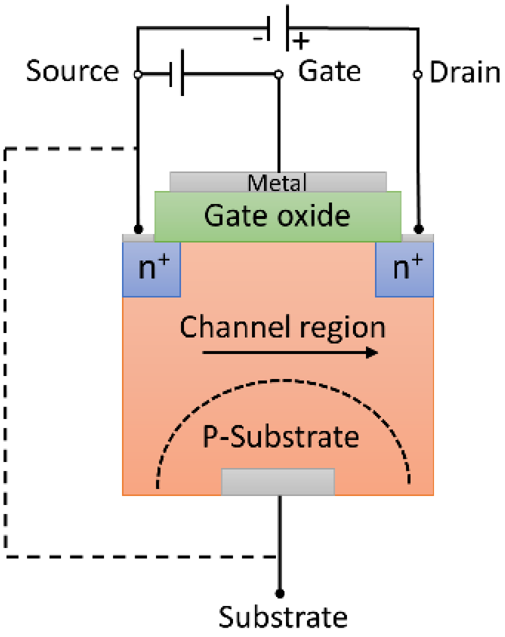

Figure 1.2 Arrangement and configuration of the drain, source and gate terminal in a n-type MOSFET device.

As seen in Figure 1.2, the source and drain terminals are connected to the ends of a channel created between two doped regions of the semiconductor material. This channel is then separated from the gate terminal by a thin layer of insulating material known as the gate oxide [10]. The gate terminal determines the functionality of the MOSFET as it controls the conductivity of the device by alternating the voltage applied to it. This is because when a voltage is applied to the gate, it creates an electric field which attracts or repels free carriers, creating or reducing the conductive channel between the source and drain [11].

There are two modes of operation for a MOSFET; these are known as depletion and enhancement mode. Depletion mode occurs when the channel between the drain and source is present without any voltage being applied to the gate terminal. The gate voltage is then used to deplete the channel of carriers and reduce the current flow. This occurs when a voltage is applied to the gate terminal and the electric field repels charge carriers in the channel region. Subsequently, a depletion region is formed, which reduces the number of free charge carriers and increases the resistance of the channel, reducing current flow. Enhancement mode on the other hand has no conductive channel present in the absence of the gate voltage. Thus, when a voltage is applied it attracts carriers in the channel allowing current to flow [9,12]. Therefore, whether the voltage applied to the gate terminal is positive or negative is determined by the (required) conductivity type (n-type or p-type) in the particular mode of operation.

For the relevance of this work a brief description of the gate oxide is needed. As stated previously the gate oxide is a thin piece of insulating material used to electrically isolate the gate terminal from the conducting channel. The ideal gate oxide is defect free and thin with a low leakage current [13]. The material that was typically used for this was SiO_2 but with the ever-decreasing size of MOSFETs, the reliability of the SiO_2 layer also decreased as electrical breakdown would occur in the films at the newly required smaller thicknesses. It is for this reason that high-k dielectrics such as Al_2O_3 are being used as gate oxides as an alternative to SiO_2 as they perform more reliably at the required thicknesses [14,15].

As stated previously, these devices are constantly becoming smaller to allow for increased computational power. As a MOSFET becomes smaller, the distance between the drain and source decreases, meaning the gate's ability to control the flow of current in the channel region reduces. This leads to larger leakage currents, which, if too high, renders the transistor inoperable. It is for this reason that the fin field-effect transistor (FinFET) was developed. This is a variation on the MOSFET where the gate is placed on multiple sides of the channel forming a multigate structure. This structure allows for enhanced electrical control which reduces the leakage current of the device [16].

1.1.3 Current Fabrication Methods and Their Limitations

Currently, the primary way in which ICs and their constituent components are patterned is through optical lithography. This is a photon-based technique that projects a pattern onto a semiconductor material, usually a silicon wafer. The design is chemically recorded on the surface of the semiconductor using a photoresist coating and light, typically in the ultraviolet (UV) range. The photoresist is a photosensitive emulsion that reacts with the light. Once the photoresist is applied to the surface of the semiconductor, an alignment mask that allows the pattern to be projected onto the surface of the substrate is used. Light is then shone through the mask and strikes the semiconductor substrate in selected areas where it reacts with the photoresist. The light causes the exposed regions to either become harder or softer through a photochemical reaction. These regions are then etched away at different rates when compared to the non-exposed areas during the subsequent etching process [17]. A schematic depiction of the fabrication process can be seen in Figure 1.3. This type of fabrication is described as a "top-down" method as it creates the pattern through the controlled and directed etching and removal of material from one large initial piece of material.

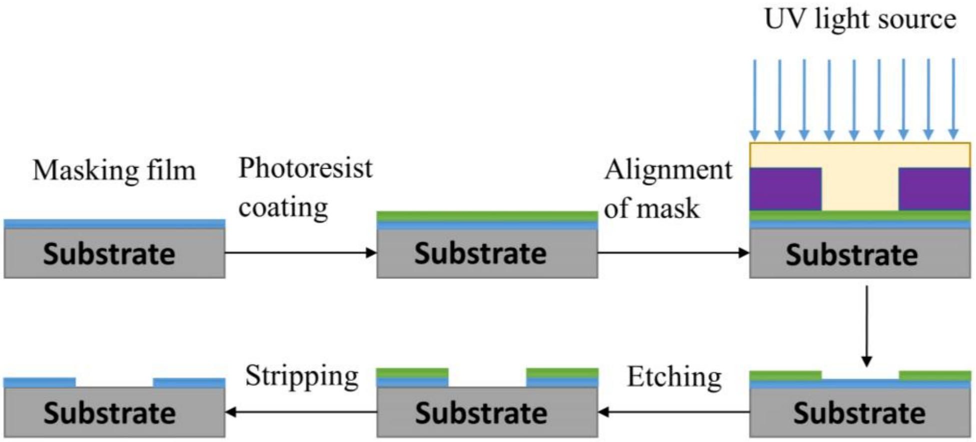

Figure 1.3 Schematic diagram which illustrates the step-by-step process of optical lithography.

These systems have been developed over the decades to enable the semiconductor device industry to keep up with the trends forecasted by Moore's law. The critical dimension (CD) of these optical lithography tools is the main aspect that determines the minimum achievable feature size [18]. The main factors which influence the CD are the wavelength of the light used, λ, the numerical aperture, *NA,* which limits the number of diffraction orders used to form an image [19], and the process-dependent resolution factor, k_1. The impact of these factors on the CD is given by [17]

$$CD = k_1 \frac{\lambda}{NA} \qquad \text{Eqn(1.1)}$$

A decrease in CD has previously been accomplished by obtaining a larger numerical aperture, which was achieved by improving the system's optics. However, this had reached its limit and in 1994 ASML began their work on decreasing the wavelength used to allow for further reduction in device size. This called for the introduction of extreme ultraviolet (EUV) lithography and in 2013 ASML produced and shipped their first EUV lithography machine [20]. Previously used wavelengths ranged between 248 nm and 193 nm; this is in contrast to EUV where wavelengths ranging between 124 nm and 10 nm, with photon energies of 10 eV and 124 eV respectively, can be achieved. However, wavelengths of this scale are not easily produced or controlled requiring an extremely high-powered laser which is both costly to make as well as to run. Unlike standard optical lithography, EUV lithography also requires a series of reflective optics to function, this includes the pattern transfer mask. This not only adds additional cost and complication, but as EUV light is so readily absorbed, the material that these optics are made from must be highly reflective. This high absorption also requires the process to be conducted in ultra-high vacuum (UHV) as EUV light is also absorbed in atmosphere. Together the standard EUV lithography system costs approximately $120 million, making this an extremely costly method to be used in research and is generally only accessible to industrial manufacturers [21].

With the cost in mind, the future for EUV lithography does not look bright as the only option for further size reduction is a further increase in the numerical aperture which is extremely difficult to achieve. This shows that the limits for optical lithography in the semiconductor industry are being reached and a new methodology is required.

1.2 New Methodology

1.2.1 Bottom-Up Vs Top-Down Fabrication

With the rising complications of the ever-decreasing transistor size, numerous efforts have been invested into the research and development of new methodologies for the fabrication of these nanoscale devices. As previously mentioned, these devices are currently being developed through optical lithography. This would be described as a 'top-down' fabrication approach. This method utilises the removal of bulk material to form the desired pattern [22]. As stated previously, this method is reaching its size limits and new methodologies are needed.

An alternative approach to device manufacturing is the so called 'bottom-up' fabrication technique. This method relies on chemical or physical forces operating at the nanoscale to self-assemble basic units into larger structures of suitable dimensions. It is then using these structures that one can create the desired patterns [22]. By using this method, the resolution of the system would no longer be determined by influences such as the wavelength of light and the overall process has the potential to be significantly cheaper. There is also the benefit of reduced edge placement error, usually associated with mask aligners, when using a bottom-up fabrication technique making device fabrication easier and more precise [23].

There are many different approaches to bottom-up fabrication, but the one that will mainly be discussed within this thesis is ASD. This is a field of research that looks at the chemical and physical processes which allow for the controllable deposition of a material onto a desired "growth" region of an exposed surface without depositing on an adjacent "nongrowth" area. These regions tend to be differentiated by the composition of the substrate material, the surface termination, the lattice structure or the physical topography [24]. This differentiation tends to be achieved through the chemical activation [25,26] or deactivation [27–29] of particular substrate regions. This area is of significant interest to the semiconductor industry due to its capacity for fabricating high-resolution patterned substrates, which has the potential to overcome the technical and financial limitations that current fabrication techniques face [30–32].

1.2.2 Atomic Layer Deposition

1.2.2.1 Fundamentals

Atomic layer deposition (ALD) is a thin film fabrication technique defined by its self-limiting growth characteristics through the sequential exposure of vapour phase precursors [33,34]. This method was first introduced by Suntola and Anston in 1977 by depositing ZnS for flat panel displays where it was first named atomic layer epitaxy (ALE) [35]. The transition from ALE to the now more commonly known ALD was due to the fact that not all films deposited through this method were epitaxial to their underlying substrates as amorphous films were also being grown [34].

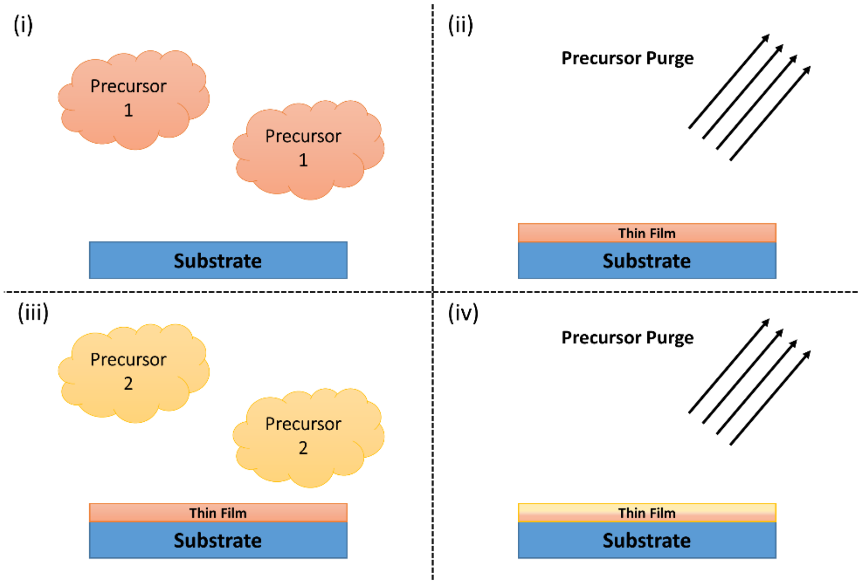

Figure 1.4 Basic step by step illustration of an ALD cycle with (i) the first chemical vapour precursor exposure, (ii) the purge of the unreacted precursor and any by-products followed by (iii) the second exposure completing the chemical reactions forming the final thin film and finally (iv) the second precursor purge.

ALD is a comparable approach for thin film fabrication to the well-known chemical vapour deposition (CVD). The major difference between these two techniques is that CVD exposes the substrate to both reacting chemical precursors at once, whereas ALD does so in a sequential process [36,37]. A schematic of a basic step-by-step ALD cycle can be seen in Figure 1.4. The first step, (i), is exposing the substrate to the first gaseous chemical precursor, which then reacts with the substrate depositing the desired material. This reaction is self-limiting, which means that once the precursor has interacted with all available reaction sites on the substrate deposition stops, leaving one monolayer of the material. Any unreacted precursor and by-products produced are then purged from the reaction chamber as seen in Figure 1.4 (ii). This is then followed by the second exposure of the co-reacting precursor, (iii), which once again is self-limiting and finishes the fabrication of the desired thin film. Finally, this precursor and any by-products are purged from the system, (iv) [38].

These four steps comprise one full cycle of an ALD process and they are then repeated until the desired thickness of the film is created. This is one of the many advantages of ALD as the layer-by-layer deposition allows for precise thickness control. The thin films produced through ALD are also highly conformal and of good quality which is required in most thin film applications [39].These advantages of ALD has led to it being used for a wide variety of applications, with the microelectronics industry being one of its biggest users. Intel introduced the use of this process in 2007 due to the increase in demand for smaller semiconductor devices [40].

1.2.2.2 Thermal ALD Vs Plasma enhanced ALD

There are two main ways in which ALD can be carried out. The first is known as thermal ALD, which uses two vapour phase precursors to fabricate the desired material. The second method is plasma enhanced ALD (PEALD), this uses plasma as the co-reactant instead of the second gaseous precursor [41]. A schematic depiction comparing these two processes can be seen in Figure 1.5.

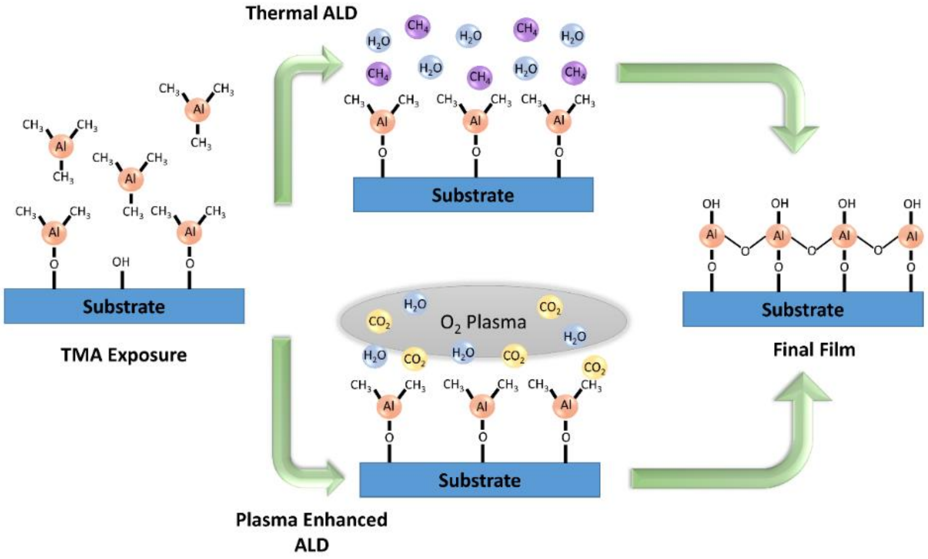

Figure 1.5 Schematic diagram of an aluminium oxide thermal ALD process compared to a PEALD process highlighting the use of water, in the case of the thermal process, and an O_2 *plasma, in the case of the PEALD process, as the different co-reactants.*

These processes can be used to fabricate films of the same chemical structure and to illustrate the differences between the two an example of fabricating aluminium oxide using the precursor trimethylaluminum (TMA) using both thermal ALD and PEALD will be shown. This material has been chosen as its deposition has been widely documented and researched [42–44].

The deposition of aluminium oxide using a thermal ALD process consists of exposing the substrate to the TMA precursor, followed by the co-reactant which in this case is water as it is commonly used for the fabrication of oxides [45]. When first exposed, the TMA interacts with the hydroxy groups present on the surface of the substrate. This allows the aluminium to bind to the surface while producing the by-product of methane gas [46]:

$$-OH^* + Al(CH_3)_3 \rightarrow -O-Al(CH_3)_2^* + CH_4 \qquad \text{Eqn(1.2)}$$

Where the asterisks show the surface species for each process step. Following this, the unreacted precursor and the methane gas is purged from the system and a subsequent water dose occurs. This allows for further reduction of the aluminium for the formation of aluminium oxide; once again, methane gas is created as a by-product of the reaction [46]

$$\text{-O-Al(CH}_3\text{)}_2^* + H_2O \rightarrow \text{-O-Al(CH}_3\text{)OH}^* + CH_4 \qquad \text{Eqn(1.3)}$$

Any excess precursor and the methane are removed from the chamber through another purge step. This leaves a single monolayer of aluminium oxide which is hydroxy terminated which facilitates further reactions to occur in subsequent ALD cycles.

Similar to the thermal ALD process, for PEALD the first stage is that the substrate is exposed to the TMA precursor which reacts with the hydroxy groups on the substrate as seen in Eqn(1.2). However, instead of exposing the sample to a water dose an oxygen plasma is used. The energetic species within the plasma facilitate the reduction of the aluminium to aluminium oxide with carbon dioxide and water produced as the by-products [47]

$$\text{-O-Al(CH}_3\text{)}_2^* + 4O \rightarrow \text{-O-Al(CH}_3\text{)OH}^* + CO_2 + H_2O \qquad \text{Eqn(1.4)}$$

One of the major advantages of using PEALD as opposed to thermal ALD is its ability to be conducted at lower temperatures. This is because the energetic species within the plasma drive the reactions and energy in the form of heat is not required unlike the thermal process. It is also a cleaner method of deposition as there are less ligands present from the second chemical precursor allowing for better elimination of impurities such as carbon. It is also easier to fabricate single element materials such as pure metals using a PEALD process [48].

1.2.2.3 Area Selective ALD

Area selective ALD combines both the methodologies of ASD and ALD for the fabrication of patterned substrates. This method of nanopatterning tends to be achieved through the area deactivation of the desired none growth regions. This is typically achieved through the use of self-assembled monolayers (SAMs). These are films that are one molecule thick which spontaneously form highly ordered large-scale structures on specific substrates. They consist of a terminal functional group, a head group, and a hydrocarbon segment. It is the head group of the SAM structure that allows for strong interaction with the substrate, leading to the formation of a stable monolayer film [49]. SAMs can selectively bind to specifically functionalised surfaces making that surface chemically uniform. These films inhibit the deposition of materials thus only allowing the fabrication of the deposited thin films in the desired growth regions while blocking deposition where the SAM is present. These can be used to form patterns as the SAMs are functionalised and will only interact with substrates containing the complementary functional group [50].

Bent and co-workers are leading experts in the use of SAMs for both ASD and area-selective ALD. An example of this would be their use of SAMs to deposit patterned aluminium oxide onto the following substrates: Cu, Co W and Ru [51]. Similarly, Chang *et al*. demonstrated the use of SAMs for the area selective ALD of Al_2O_3 onto Co [52]. Other methods of achieving area-selective ALD is through the use of polymers [53,54]. This is achieved as depending on the polymer chemistry it can be used as an activation layer [25] i.e. facilitating the deposition or a deactivation layer [55] similar to SAMs inhibiting the deposition. The details of this process will be further illustrated in section 1.2.4 and a full comparison of polymers and SAMs will be discussed in section 1.2.7.

1.2.3 Polymer Theory

A polymer is defined as a large molecule consisting of repeating subunits called monomers, these are joined together by covalent bonds [56]. Examples of the monomer structure for two of the main polymers used in this work, poly(methyl methacrylate) (PMMA) and polystyrene (PS), can be seen in Figure 1.6. Polymers can be natural or synthetic and can have a wide range of properties depending on their chemical structure and molecular weight, both of which are very important for this work and will be discussed in more detail further on [57].

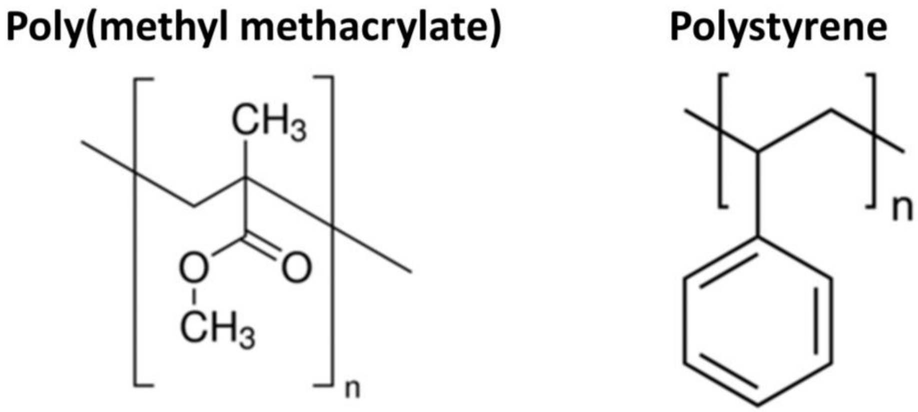

Figure 1.6 Example of the polymer structures of the two main polymers used within this work PMMA and PS.

The basic structure of a polymer consists of a chain-like configuration which is known as the polymer backbone and from this there can be protruding side groups, such as the benzene ring seen in the PS structure [58,59]. Polymerisation is the way this structure is formed and it refers to the way in which the singular monomer subunits chemically bond together [60]. This can be achieved in two different ways, addition, or condensation polymerisation.

Addition polymerisation is a type of reaction that involves the sequential addition of monomer units to the growing polymer chain and consists of three main steps. This reaction typically involves the use of an initiator, which can be a radical initiator, an anionic initiator, or a cationic initiator, that starts the reaction by generating a reactive intermediate species. This is often achieved through the application of heat, light or a catalyst. The following step is referred to as propagation, this works as the reactive monomer created in the initiation step interacts with the next monomer allowing it to bind to it and becoming a reactive intermediate species in itself. From here this process repeats itself 'adding' on more monomer units until the polymer chain is fully grown. Finally, is the termination step, here the polymerisation reaction is ended by the removal of the reactive intermediate species. This can occur through a number of mechanisms, such as the combination of two reactive intermediates to form a new bond, reaction with a chain transfer agent, or reaction with a terminating agent [61]. With condensation polymerisation there is no addition of a free radical initiator, here the monomers react with each other through condensation reactions which involve the elimination of a small molecule, such as water. This allows a covalent bond to form between the monomers. This reaction proceeds until the monomers are consumed or until the polymer reaches a desired molecular weight [59].

The total number of monomers that bind together to form the overall polymer chain is known as the degree of polymerisation (DP). This relates to the overall molecular weight of the polymer and can be calculated using the following equation [56]

$$DP = \frac{M_w}{M_m} \qquad \text{Eqn(1.5)}$$

where M_w is the total molecular weight of the polymer and M_m is the molecular weight of the monomer. Eqn(1.5) shows that with an increase in the molecular weight of the polymer there is an increase in the DP. This indicates that with a larger molecular weight the overall length of the polymer chain is larger. This is very important to note for the work discussed in Chapter 3.

Polymers tend to be made up of only one singular type of monomer, however, there can be combinations of different types of monomers which are known as copolymers. There are four basic structures in which these copolymers can be found, and a schematic representation of these can be seen in Figure 1.7. The first is the random structure which, as the name suggests, means there is an irregular pattern of monomers. Secondly, the monomers can form an alternating copolymer, where each monomer alternates with the other. The third structure is the BCP, where more complex repeating units consisting of portions of different polymer chains are connected. Finally, there is the graft copolymer meaning, in this structure, monomer chains of one type attach to an already fabricated polymer chain of a different polymer material [62].

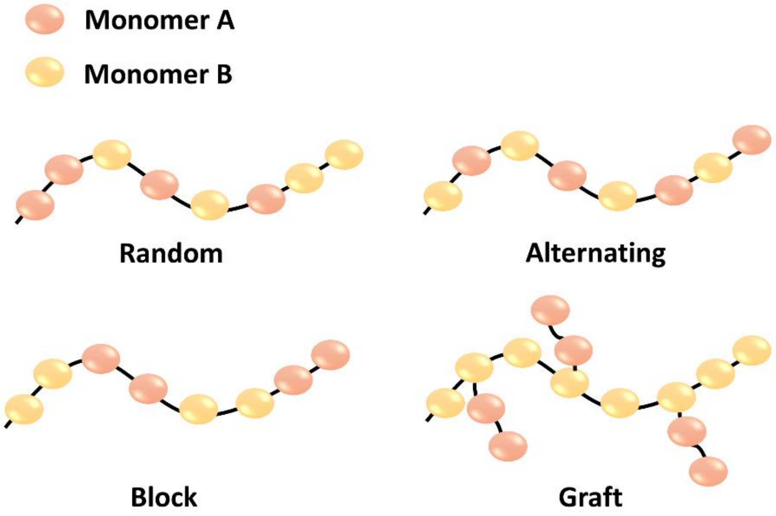

Figure 1.7 Schematic representation of the random, alternating, block and graft copolymer structures formed through the combination of two monomers.

1.2.4 Polymers in Area Selective Deposition

The use of polymers for ASD applications has become widespread in recent years due to their low price and short fabrication times [63–67]. These materials have area selective properties due to their chemistry and structure, they either facilitate infiltration by a material into their structure or they block this infiltration. For the purpose of this work polymers which accept infiltration will be referred to as active while polymers that block infiltration will be referred to as inactive.

Many reported works have demonstrated polymers' area selective properties and their effectiveness in fabricating patterned substrates. Cummins *et. al.* showed the fabrication of patterned copper and gold substrates through the use of polymer blocking. This technique uses an inactive polymer, in this case, PS, to deactivate nongrowth regions and to allow for metal deposition to occur in the adjacent growth areas. In this work, amine-terminated PS was deposited onto a patterned copper and silicon dioxide substrate. Due to the termination of the PS, it selectively grafted to the copper regions thus deactivating them. After the deposition of the PS, gold was then evaporated onto the silicon oxide regions. Using an etching process the polymer was then removed leaving the copper and gold patterned substrate [68].

As stated previously the work discussed above is an example of a deactivation process. Active polymers and their use in ASD has also been demonstrated using a similar technique as discussed above [69]. The use of polymers in the field of ASD is widely studied, however the effect that the characteristics of a polymer, for example, molecular weight, has on their infiltration and blocking mechanisms are not widely reported in the literature. This work aims to study these variables in detail.

1.2.5 Block Copolymer Lithography

As previously mentioned, a BCP can be defined as a polymer made up of two or more different polymer chains covalently bound in a repeating pattern [62]. When a BCP is formed the polymer pairs tend to be immiscible with one another, this means that for the polymer system to reduce its overall energy the different block regions try to remain physically separate from each other (i.e. they phase separate). However, this cannot occur on the macroscopic length scale due to the covalent bonds between the different blocks. Instead the polymers spontaneously form ordered structures at the molecular scale with a domain size 10 to 100 nm, which balance these two competing driving forces [70–73].

The separation and size of the nanostructures formed within a BCP structure is dependent on the Flory Huggins parameter. This parameter shows the degree of incompatibility between the two different polymers and it is this that drives the phase separation. It can be calculated as follows;

$$\chi_{AB} = \left(\frac{z}{k_B T}\right)\left[\varepsilon_{AB} - \frac{1}{2}(\varepsilon_{AA} + \varepsilon_{BB})\right] \qquad \text{Eqn(1.6)}$$

where χ_{AB} is the Flory Huggins parameter, z is the number of nearest neighbours per repeat unit in the polymer, $k_B T$ is the thermal energy, and $\varepsilon_{AB}, \varepsilon_{AA}$ and ε_{BB} are the interaction energies per repeat unit of the monomers A-B, A-A, and B-B respectively [74]. The larger the value of this parameter the more incompatible the two polymers are. This leads to the fabrication of smaller feature sizes, thus creating a higher resolution [72].

The morphology of these structures is then determined by the overall DP and the composition of the polymer within the diblock which is given by [75]

$$f_A = \frac{N_A}{DP} \qquad \text{Eqn(1.7)}$$

Where f_A is the composition and N_A is the number of A monomers per molecule. BCPs can form a variety of morphologies which include spheres, hexagonally packed cylinders, gyroid, and lamella. Which pattern the BCP forms is dependent on the interfacial energy between the two blocks, the chain stretching and the volume fraction of each of the polymers. As the self-assembly begins the polymers couple together in such a way as to minimise the surface area between them, allowing for a system that is more energetically favourable. The phase separation causes the polymers to stretch from their preferred coil configuration, the degree of which is dependent on the volume fraction. When a BCP mixture is very asymmetric the polymer in the smaller quantity begins to form spherical microdomains leaving the other to surround these spheres and form what are known as coronas. As the volume fraction becomes more equal, curved interfaces begin to form meaning that the polymers change their morphology to avoid being stretched out. This leads to the transition between the various morphologies. Figure 1.8 shows this transition from each of these structures as the volume fraction of two different polymers change [73,74,76].

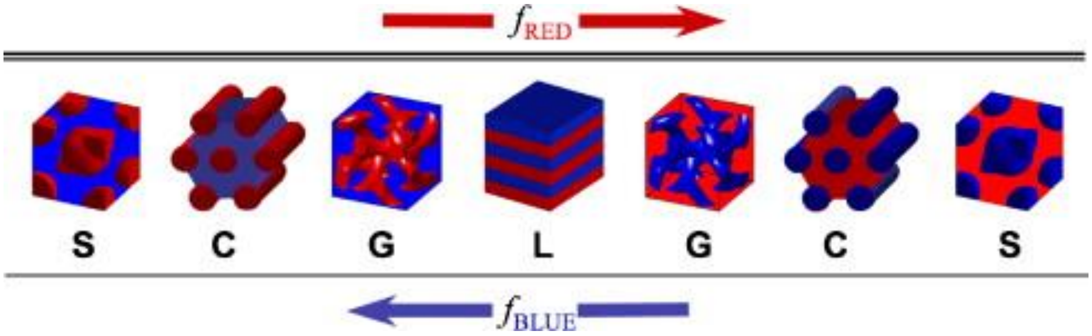

Figure 1.8 BCP morphologies as the volume fraction of polymer 1 (red) changes with respect to polymer 2 (blue). Morphologies are shown in the increasing red-block (decreasing blue) composition of a red-blue BCP. (S) sphere,(C) hexagonally packed cylinders (G) gyroid, and (L) lamellae [77].

BCPs ability to self-assemble has made them of great interest in semiconductor research. In section 1.2.4 the area selective nature that polymers have depending on their chemistry was discussed. Combining an active and inactive polymer in a BCP film would allow for the formation of a self-assembled pattern of active and inactive regions. If these films were infiltrated, it would lead to the development of a patterned substrate which is known as BCP lithography. Tseng *et. al.* demonstrated this method by fabricating an alumina nanopattern using a self-assembled block copolymer system of PMMA and PS [64]. Goshal *et. al.* also shows the use of PS-b-poly(ethylene oxide) for the fabrication of patterned silver lines and dots [78]. This method of producing metal patterns on the nanoscale is one of the many bottom-up techniques being studied, with the hope of replacing conventional methods such as optical lithography. Using a variety of different combinations of polymers, the feature size can be controlled as well as the structures created. This offers immense potential for the technique of ASD, as well as for the broader field of lithography.

1.2.6 Polymer Brush Theory

A polymer brush can be described as several polymer chains, of a sufficient density, which are tethered to the surface of a substrate; it is also known as a polymer film [79–81]. These films are a major area of research in the ASD and BCP fields, as they can be used not only for surface activation and deactivation in themselves but also allow for detailed characterisation of the polymers in different environments. For example, one could look at how certain polymers react with different infiltration materials or methods and how the polymer properties, such as molecular weight, could effect this infiltration. This information is vital for ASD and BCP lithography as it would show how each polymer block would react within different infiltration environments. It is for this reason that the characterisation of different polymer brushes and their infiltration mechanisms are a major part of this work.

For a polymer film to be considered a brush, the polymer chains must be sufficiently dense. When the polymer chains are at a high density, steric hindrance between each chain causes them to stretch from their standard coil formation [82]. This stretching is what causes the polymer brush to form. When the chains are initially tethering to the surface, the distance between attachment sites is too large for the chains to interact with each other, which causes the chains to coil and fall. This is known as the mushroom regime and this term can be used to describe a polymer film with a low grafting density [79,80,83]. From here as more chains tether to the surface and the distance between each attachment site decreases, the film transitions to a polymer brush. Figure 1.9 illustrates this density dependence and shows that if the distance between attachment sites is too large the films form the coiled mushroom regime compared to the highly dense brush regime.

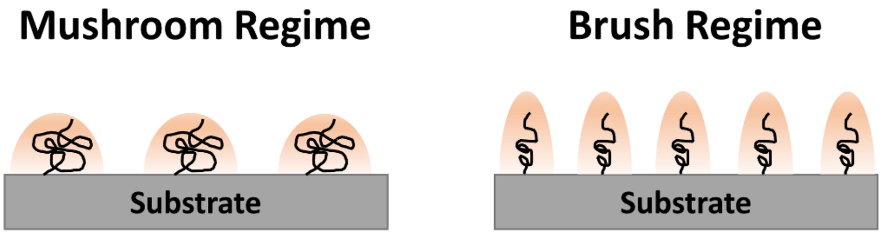

Figure 1.9 An illustration depicting the mushroom and brush regime and its dependence on chain density.

It was stated previously that with an increase in the polymer chain density there is an increase in the amount of chain stretching occurring. This means that there is a direct relationship between the density of the polymer brush and its overall thickness. This relationship is given by Eqn(1.8) [82].

$$L = N\sigma^{\frac{1}{3}} \qquad \text{Eqn(1.8)}$$

where L is the brush thickness, N is the chain length and σ is the chain density. This equation shows that for an increase in brush thickness to occur an increase in the density and chain length is required. From Figure 1.9 the difference between the brush and mushroom regime and their dependence on the polymer chain distance can be seen. From this figure, it is clear that the brush regime leads to a thicker film as the chains are experiencing greater extension due to the steric hindrance between them. This relates to Eqn(1.8) as the polymer chains have a higher density in the brush regime due to the small distance between the grafting sites, which means that the density and grafting site distance are inversely proportional. This is relevant for the work discussed in Chapter 3 as methods of increasing the overall brush thickness of the polymers PMMA and PS are explored.

1.2.6.1 Polymer Brush Fabrication

There are two main ways in which polymer chains can be tethered to a substrate, they are attached either by physisorption or chemisorption. When chains are physiosorbed to a surface, selective absorption of one block within a diblock copolymer attaches itself to the surface. This tethering is not stable and is easily reversible as no chemical bonds are formed in this process. Chemisorption, on the other hand, involves the covalent bonding of the polymer chains to the substrate. This is much more stable and is difficult to reverse making it a much more favourable option for chain tethering [83].

When fabricating a polymer brush using chemisorption two methods can be used, the “grafting from” and “grafting to” processes. A schematic representation of these techniques can be seen below in Figure 1.10. The grafting from technique involves the in-situ polymerisation of the polymer chains from the substrate surface. This is achieved through the submersion of a polymer initiator functionalised substrate in a monomer solution. This allows for the monomers to react with the initiators binding to the substrate and from here polymerisation can occur, leading to the polymer brush growing from the surface. This method allows for the fabrication of highly dense and thick polymer brushes [84]. However, it is an extremely chemically intensive method of fabrication and it can be hard to make reproducible polymer films as there is no way to characterise the polymer chains prior to the brush fabrication [80].

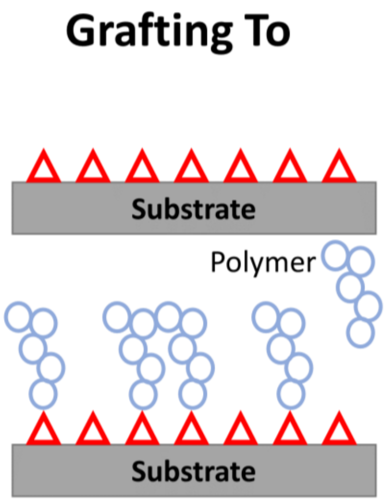

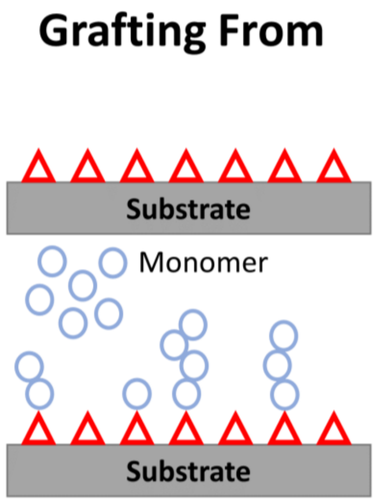

Figure 1.10 Schematic comparison of the grafting to and grafting from techniques for polymer brush fabrication.

The grafting to method on the other hand uses prefabricated polymer chains. These tend to have a functional group at the end of the chain which allows them to bond to a substrate surface with the corresponding functional group. For example, in this work polymers which have been hydroxy functionalised are used to graft to the surface of hydroxy functionalised silicon substrates. Through a condensation reaction these polymer chains can successfully graft to the silicon substrate. This method is technically simpler than the grafting from technique and is a lot less chemically intensive. It also has the added benefit of allowing for in-depth characterisation of the chains before brush fabrication which allows for very reproducible films. However, this technique does come with its disadvantages as it is hard to acquire extremely dense films thus making it harder to fabricate thicker films [85]. Despite its disadvantages, the grafting to method is favoured in this work. This method was used for its technical ease as well as its ability to facilitate rapid and reproducible brush fabrication.

1.2.7 Polymers versus Self-Assembled Monolayers

The definition of a SAM and how they are used in the field of ASD have been discussed previously in section 1.2.1. When comparing these monolayer structures to a polymer brush one of the distinct differences is that a SAM can only act as a deactivation layer, while polymers can be seen as more versatile being able to act as an activation or deactivation layer depending on the polymer's chemistry. Secondly, to fabricate a stable SAM with suitable substrate coverage requires a lot of time varying from hours to several days [86,87]. This is compared to polymer brush fabrication which can be optimised so that a brush with suitable substrate coverage can be achieved in just a few seconds [88]. Chapter 4 of this thesis demonstrates the rapid fabrication of PS brushes for the blocking of a hafnium oxide ALD process, which shows high levels of selectivity similar to those achieved using SAMs. Finally, one of the standout differences between the use of polymers and SAMs for ASD is that, as previously discussed, polymers can be used in a BCP system to self-assemble to form nanostructures. Thus, patterns can be formed without any human interaction unlike SAMs which requires specific substrate functionalisation for them to attach and form the desired pattern.

1.2.8 The Infiltration of Polymers Through ALD-based techniques

As previously discussed in section 1.2.4, polymers can accept or block infiltration based on their chemistry and chemical structure. When combining active and inactive polymers in a BCP system, one can create a patterned substrate of regions that facilitate and block infiltration simultaneously. Post infiltration, the BCP layer can then be removed using an oxygen enriched environment such as UV ozone or O_2 plasma. This then leaves a pattern of the infiltration material used on the substrate. Infiltration can be achieved in many ways; for example, Snelgrove *et. al.* demonstrated the use of a liquid phase infiltration process by which poly-2-vinylpyridine (P2VP) was infiltrated using a copper salt solution [89]. Polymer infiltration through a vapour phase infiltration (VPI) process has also been shown to be successful and is the method focused on in this work [25,26].

The basis for the VPI process has been derived from ALD techniques which has been discussed in depth in section 1.2.2. It involves the exposure of the polymer film to a vapour-phase metalorganic precursor which then infiltrates into the polymer matrix and reacts with the functional groups [90]. The main difference between ALD and VPI is the way in which the substrate interacts with the precursor. ALD relies on precursor adsorption on the substrate while VPI requires the diffusion of the precursor into the substrate i.e. the polymer [91]. A typical VPI process consists of the following steps: Firstly, the precursor is pulsed into the chamber, which is known as the dose step and is controlled by the chamber pressure, carrier gas flow, precursor temperature and the time the precursor admittance valve is open. Following this the chamber is held under static vacuum for a period of time ranging from seconds to minutes, which is referred to as the hold step. This is done as it allows for adequate time for the precursor to interact and infiltrate the polymer. The chamber is then purged to remove any of the unreacted precursor and the process can then repeat itself. A co-reactant can be used but is often not essential; in the case where it is used there would be another dose step, hold step and purge for the co-reactant following on from the precursor.

There are different ways in which VPI can be achieved these include semi-static sequential infiltration synthesis (SIS), flow mode SIS, multiple pulsed infiltration (MPI) and sequential vapor infiltration (SVI). In the case of the semi-static SIS mode, the precursor and co-reactant undergo static-hold steps after which the chamber is fully evacuated back to vacuum. The flow mode SIS and the MPI processes are effectively identical; unlike in static mode SIS the chamber is never evacuated to baseline vacuum in these processes. Finally the SVI process repeatedly delivers the same precursor via multiple dose steps before exposing the co-reactant and the hold steps are much shorter (typically only 30 to 60 seconds long) [92].

1.3 Overview of the Results Presented

The results presented in this thesis have come from a collaborative project between the author's own affiliation, the School of Physical Sciences at Dublin City University (DCU), and the Centre for Advanced Materials and BioEngineering Research (AMBER) at Trinity College Dublin (TCD). This project was supported by Intel and Science Foundation Ireland (SFI).

The AMBER centre's focus of research was the development of a rapid polymer brush fabrication process utilising the grafting to method, as discussed in section 1.2.6.1, as well as the infiltration of these polymers via a liquid phase approach. One of the research objectives of DCU and therefore this thesis was to further the development of this process for the fabrication of thicker polymer brushes and then to characterise these films in detail. This was achieved mainly using techniques available at DCU with complementary resources at synchrotron laboratories. The details of these techniques are outline in Chapter 2. Additionally, using ALD infrastructure present in DCU, the vapour phase infiltration of these polymers was investigated focusing on both the effect of increased thickness as well as polymer type.

The main results arising from this thesis are split into 3 chapters, each with the overall objective of gaining an understanding into the way in which the polymer properties such as molecular weight effects the thickness of the resulting brush and therefore how this change in thickness effects the polymers ability to be infiltrated or act as a deactivation layer.

The experimental work focuses upon four covalently grafted polymer brushes developed at DCU: PMMA, PS, poly-2-vinyl pyridine (P2VP) and polyethylene oxide (PEO). The monomer structure for each of these polymers can be seen below in Figure 1.11. The method of brush fabrication used allows for the polymers to be ASD compatible and can be patterned via conventional lithography or by tailoring the functional end groups of the polymer.

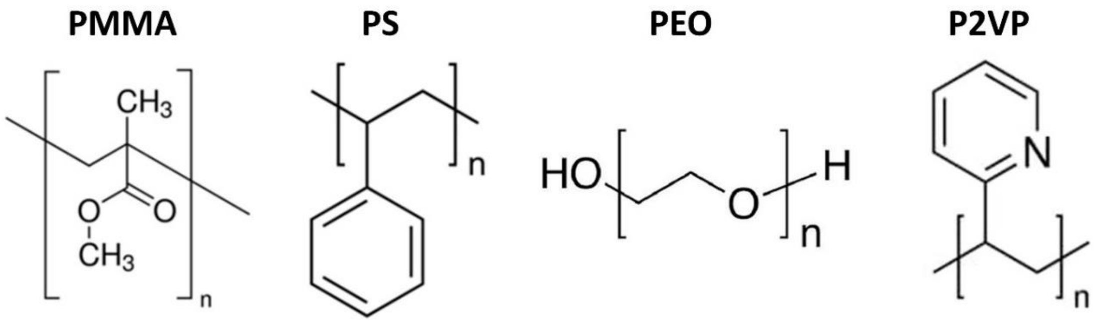

Figure 1.11 Monomer structures for the four polymers PMMA, PS, PEO and P2VP used in this work.

PS and PMMA are well known polymers for their ability to achieve area deactivation and activation respectively [55,93]. It is for this reason that they are such a large focus of this work due to their shown success in previous studies. P2VP and PEO are also investigated due to their large Flory Huggins parameter when placed in a BCP system with PS. This allows for small feature sizes to be achieved in the BCP pattern than that created when using PMMA.

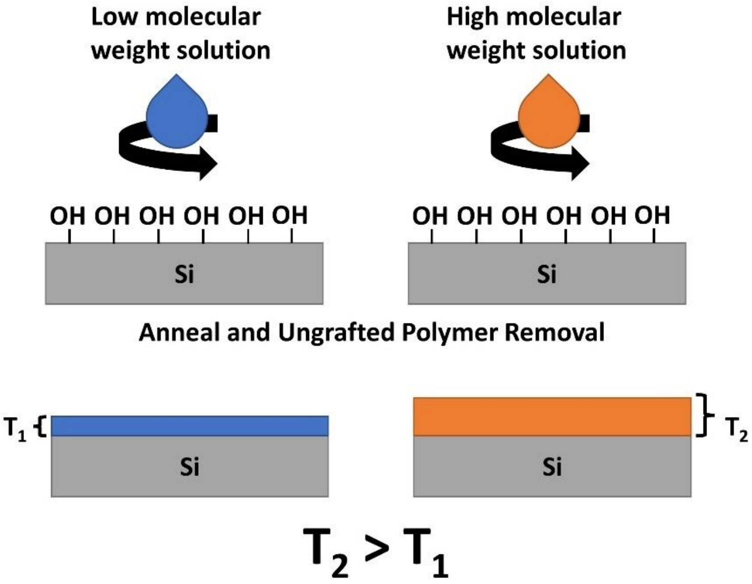

Figure 1.12 Graphical abstract of experiments outlined in chapter 3. Brushes were fabricated using different molecular weight polymer solutions at varying solution concentrations for the making of thicker polymer brush.

The first of the experimental results shown in Chapter 3, Figure 1.12, investigates two methods for the fabrication of thicker PMMA and PS brushes while using the grafting to approach. The first illustrated the effect that increasing the fabricating solution concentration as well of the molecular weight of the polymer had on its resulting thickness. It was seen for both polymers that an increase in both parameters led to an overall thicker brush that was of good quality. Following on from this a stepwise approach for the fabrication of thicker PS films was studied. This looked at the potential of functionalising a PS brush through the use of an O_2 plasma process, which was achieved using a Henniker benchtop plasma system, to allow for a second application of the PS solution. This process was shown to be unsuccessful as while there was an overall increase in the brush thickness, it was not significant enough to warrant the extra time required for this type of fabrication.

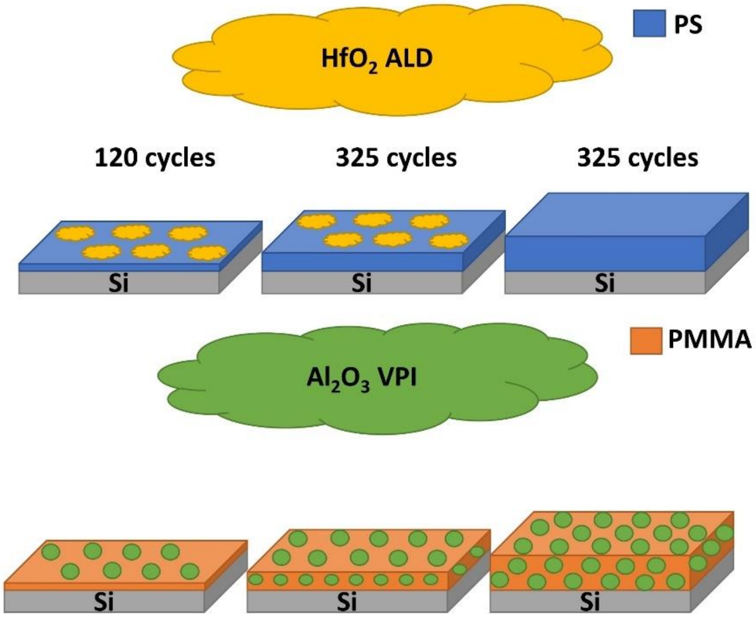

Figure 1.13 Graphical abstract representing the results of seen in chapter 4. PS brushes of differing thicknesses were exposed to a hafnium oxide ALD process over a number of cycles as well as PMMA brushes of varying thicknesses exposed to an aluminium oxide VPI process.

Chapter 4, Figure 1.13, then continues on from the results presented in Chapter 3 and looks at how this thickness increase in the PS and PMMA brushes effects their properties as an inactive and active polymer. Firstly, it was shown through the exposure of three PMMA brushes of varying thicknesses to an aluminium oxide VPI process that with an increase in brush thickness there was a slight increase in the amount of infiltrated aluminium. The use of a UV ozone and an O_2 plasma process, which was conducted in an inductively coupled plasma (ICP) source within the ALD chamber used for infiltration, for the removal of the polymer films as well as the oxidation of the infiltrated aluminium was then compared. It was shown that the O_2 plasma was more efficient and the oxide films fabricating using the thicker PMMA brushes were thicker than that of the ones fabricated using the thinner PMMA films. This chapter then shows the way in which the thickness of a PS brush effects its ability to block a hafnium oxide ALD process. By exposing three PS brushes of varying thickness to a number of ALD cycles it was shown that the efficacy of the PS at inhibiting deposition decreased with the thickness of the film.

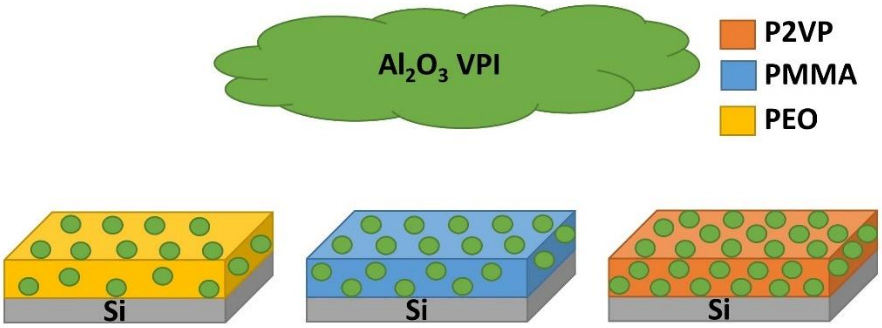

Figure 1.14 Graphical representation of the results shown in chapter 5. P2VP, PMMA and PEO brushes of the same molecular weight were exposed to an aluminium oxide VPI process showing a larger amount of precursor uptake within the P2VP film followed by the PMMA film and finally the PEO brush.

The final results shown in Chapter 5, Figure 1.14, looks at comparing the infiltration mechanisms as well as the precursor uptake of the three polymers PMMA, P2VP and PEO. Polymer brushes fabricated using the same solution concentration and molecular weight for all three tested polymers were exposed to an aluminium oxide VPI process. Through the use of HAXPES it was shown that the infiltrated P2VP had the largest aluminium uptake followed by the PMMA and finally the PEO. Then through the use of an ICP O_2 plasma process the polymer films were subsequently removed. It was then confirmed that the infiltrated P2VP brush resulted in the thickest oxide film which was determined to be down to its efficient infiltration mechanism.

Chapter 6 concludes with a summation of the main findings from the results presented in this work, with a description on the possible future research that could be conducted on the infiltration of polymer brushes which are of relevance to ASD and BCP research.

1.4 References

(1) Moore, G. E. Cramming More Components onto Integrated Circuits . *Electronics* **1965**, *38* (8).

(2) Moore's law | computer science | Britannica https://www.britannica.com/technology/Moores-law (accessed Apr 28, 2021).

(3) Snelgrove, M. Characterising Infiltration Techniques in Polymer Selective Deposition, Dublin City University, 2022.

(4) How to squeeze billions of transistors onto a computer chip | IBM https://www.ibm.com/thought-leadership/innovation-explanations/mukesh-khare-on-smaller-transistors-analytics (accessed Apr 17, 2023).

(5) Over 50 Years of Moore's Law https://www.intel.com/content/www/us/en/silicon-innovations/moores-law-technology.html (accessed Apr 28, 2021).

(6) integrated circuit | Types, Uses, & Function | Britannica https://www.britannica.com/technology/integrated-circuit (accessed Apr 29, 2021).

(7) Integrated Circuits : Design, Working, Advantages & Disadvantages https://www.elprocus.com/how-integrated-circuits-work-physically/ (accessed Apr 29, 2021).

(8) How Does an INtegrated Circuit Work | ASIC Chips | Linear MIcroSystems https://linearmicrosystems.com/integrated-circuit-work/ (accessed Apr 29, 2021).

(9) What is the MOSFET: Basics, Working Principle and Applications https://www.elprocus.com/mosfet-as-a-switch-circuit-diagram-free-circuits/ (accessed May 7, 2021).

(10) Power Electronics - MOSFET https://www.tutorialspoint.com/power_electronics/power_electronics_mosfet.htm (accessed Mar 25, 2023).

(11) Sedra, A. S.; Smith, K. C. (Kenneth C. Microelectronic Circuits. **1987**.

(12) What is MOSFET: Symbol, Working, Types & Different Packages https://components101.com/articles/mosfet-symbol-working-operation-types-and-applications (accessed May 17, 2021).

(13) Gate Oxide Studies - The Nanoscale Materials and Device Group https://www.boisestate.edu/nano/research-areas/gate-oxide-studies/ (accessed Mar 25, 2023).

(14) Chau, R.; Brask, J.; Datta, S.; Dewey, G.; Doczy, M.; Doyle, B.; Kavalieros, J.; Jin, B.; Metz, M.; Majumdar, A.; Radosavljevic, M. Application of High-κ Gate Dielectrics and Metal Gate Electrodes to Enable Silicon and Non-Silicon Logic Nanotechnology. *Microelectron. Eng.* **2005**, *80* (SUPPL.), 1–6. https://doi.org/10.1016/J.MEE.2005.04.035.

(15) Schlom, D. G.; Guha, S.; Datta, S. Gate Oxides Beyond SiO2. *MRS Bull.* **2008**, *33* (11), 1017–1025. https://doi.org/10.1557/MRS2008.221.

(16) FinFET Design, Manufacturability, and Reliability

https://www.synopsys.com/designware-ip/technical-bulletin/finfet-design.html (accessed Aug 23, 2021).

(17) Naulleau, P. Optical Lithography. In *Comprehensive Nanoscience and Nanotechnology*; Elsevier, 2019; Vol. 1–5, pp 387–398. https://doi.org/10.1016/B978-0-12-803581-8.10433-3.

(18) May, G. S.; Spanos, C. J. Fundamentals of Semiconductor Manufacturing and Process Control. **2006**, 463.

(19) The Numerical Aperture https://spie.org/publications/fg06_p16_na?SSO=1 (accessed May 7, 2021).

(20) Making EUV: from lab to fab – Stories | ASML https://www.asml.com/en/news/stories/2022/making-euv-lab-to-fab (accessed Jun 6, 2023).

(21) How does the laser technology in EUV lithography work? | Laser Focus World https://www.laserfocusworld.com/blogs/article/14039015/how-does-the-laser-technology-in-euv-lithography-work (accessed May 7, 2021).

(22) Hobbs, R. G.; Petkov, N.; Holmes, J. D. Semiconductor Nanowire Fabrication by Bottom-Up and Top-Down Paradigms. **2012**. https://doi.org/10.1021/cm300570n.

(23) Building patterns from the bottom: a complementary approach to lithography https://www.imec-int.com/en/articles/building-patterns-from-the-bottom-a-complementary-approach-to-lithography (accessed Aug 20, 2021).

(24) Parsons, G. N.; Clark, R. D. Area-Selective Deposition: Fundamentals, Applications, and Future Outlook. *Chemistry of Materials*. American Chemical Society June 23, 2020, pp 4920–4953. https://doi.org/10.1021/acs.chemmater.0c00722.

(25) Snelgrove, M.; McFeely, C.; Shiel, K.; Hughes, G.; Yadav, P.; Weiland, C.; Woicik, J. C.; Mani-Gonzalez, P. G.; Lundy, R.; Morris, M. A.; McGlynn, E.; O'Connor, R. Analysing Trimethylaluminum Infiltration into Polymer Brushes Using a Scalable Area Selective Vapor Phase Process. *Mater. Adv.* **2021**, *2* (2), 769–781. https://doi.org/10.1039/d0ma00928h.

(26) Lundy, R.; Yadav, P.; Prochukhan, N.; Giraud, E. C.; O'Mahony, T. F.; Selkirk, A.; Mullen, E.; Conway, J.; Turner, M.; Daniels, S.; Mani-Gonzalez, P. G.; Snelgrove, M.; Bogan, J.; McFeely, C.; O'Connor, R.; McGlynn, E.; Hughes, G.; Cummins, C.; Morris, M. A. Precise Definition of a "Monolayer Point" in Polymer Brush Films for Fabricating Highly Coherent TiO<inf>2</Inf> Thin Films by Vapor-Phase Infiltration. *Langmuir* **2020**, *36* (41). https://doi.org/10.1021/acs.langmuir.0c02512.

(27) Jiang, X.; Bent, S. F. Area-Selective ALD with Soft Lithographic Methods: Using Self-Assembled Monolayers to Direct Film Deposition. *J. Phys. Chem. C* **2009**, *113* (41), 17613–17625. https://doi.org/10.1021/jp905317n.

(28) Chen, R.; Kim, H.; Mcintyre, P. C.; Bent, S. F. Investigation of Self-Assembled Monolayer Resists for Hafnium Dioxide Atomic Layer Deposition. **2005**. https://doi.org/10.1021/cm0486666.

(29) Zhang, Z.; Dwyer, T.; Sirard, S. M.; Ekerdt, J. G. Area-Selective Atomic Layer Deposition of Cobalt Oxide to Generate Patterned Cobalt Films . *J. Vac. Sci. Technol. A* **2019**, *37*, 20905. https://doi.org/10.1116/1.5066437.

(30) Carlsson, J. O. Selective Vapor-Phase Deposition on Patterned Substrates. *Crit. Rev. Solid State Mater. Sci.* **1990**, *16* (3), 161–212. https://doi.org/10.1080/10408439008244628.

(31) Singh, J. A.; Thissen, N. F. W.; Kim, W. H.; Johnson, H.; Kessels, W. M. M.; Bol, A. A.; Bent, S. F.; MacKus, A. J. M. Area-Selective Atomic Layer Deposition of Metal Oxides on Noble Metals through Catalytic Oxygen Activation. *Chem. Mater.* **2018**, *30* (3), 663–670. https://doi.org/10.1021/acs.chemmater.7b03818.

(32) Vos, M. F. J.; Chopra, S. N.; Verheijen, M. A.; Ekerdt, J. G.; Agarwal, S.; Kessels, W. M. M.; Mackus, A. J. M. Area-Selective Deposition of Ruthenium by Combining Atomic Layer Deposition and Selective Etching. *Chem. Mater.* **2019**, *31* (11), 3878–3882. https://doi.org/10.1021/acs.chemmater.9b00193.

(33) Johnson, R. W.; Hultqvist, A.; Bent, S. F. A Brief Review of Atomic Layer Deposition: From Fundamentals to Applications. *Mater. Today* **2014**, *17* (5), 236–246. https://doi.org/10.1016/J.MATTOD.2014.04.026.

(34) George, S. M. Atomic Layer Deposition: An Overview. *Chem. Rev.* **2010**, *110* (1), 111–131. https://doi.org/10.1021/cr900056b.

(35) Suntola, T.; Anston, J. Method for Producing Compound Thin Films. 4058430, November 1977.

(36) Jones, A. C.; Hitchman, M. L. Overview of Chemical Vapour Deposition. *R. Soc. Chem.* **2009**, 1–36.

(37) Ritala, M.; Niinistö, J. *Chemical Vapour Deposition: Precursors, Processes and Applications*; Royal Society of Chemistry, 2008. https://doi.org/10.1039/9781847558794-00158.

(38) Richey, N. E.; De Paula, C.; Bent, S. F. Understanding Chemical and Physical Mechanisms in Atomic Layer Deposition. *J. Chem. Phys* **2020**, *152*, 40902. https://doi.org/10.1063/1.5133390.

(39) Elliott, S. D.; Dey, G.; Maimaiti, Y. Classification of Processes for the Atomic Layer Deposition of Metals Based on Mechanistic Information from Density Functional Theory Calculations. *J. Chem. Phys.* **2017**, *146* (5), 052822. https://doi.org/10.1063/1.4975085.

(40) Mistry, K.; Allen, C.; Auth, C.; Beattie, B.; Bergstrom, D.; Bost, M.; Brazier, M.; Buehler, M.; Cappellani, A.; Chau, R.; Choi, C.-H.; Ding, G.; Fischer, K.; Ghani, T.; Grover, R.; Han, W.; Hanken, D.; Hattendorf, M.; He#, J.; Hicks, J.; Huessner, R.; Ingerly, D.; Jain, P.; James, R.; Jong, L.; Joshi, S.; Kenyon, C.; Kuhn, K.; Lee, K.; Liu, H.; Maiz#, J.; Mcintyre, B.; Moon, P.; Neirynck, J.; Pae, S.; Parker, C.; Parsons, D.; Prasad#, C.; Pipes, L.; Prince, M.; Ranade, P.; Reynolds, T.; Sandford, J.; Shifren°, L.; Sebastian, J.; Seiple, J.; Simon, D.; Sivakumar, S.; Smith, P.; Thomas, C.; Troeger, T.;

Vandervoorn, P.; Williams, S.; Zawadzki, K. A 45nm Logic Technology with High-K+Metal Gate Transistors, Strained Silicon, 9 Cu Interconnect Layers, 193nm Dry Patterning, and 100% Pb-Free Packaging. **2007**. https://doi.org/10.1109/IEDM.2007.4418914.

(41) George, S. M. Atomic Layer Deposition: An Overview. *Chem. Rev.* **2010**. https://doi.org/10.1021/cr900056b.

(42) Potts, S. E.; Schmalz, L.; Fenker, M.; Díaz, B.; Swiatowska, J.; Maurice, V.; Seyeux, A.; Marcus, P.; Radnóczi, G.; Tóth, L.; Kessels, W. M. M. Ultra-Thin Aluminium Oxide Films Deposited by Plasma-Enhanced Atomic Layer Deposition for Corrosion Protection. *J. Electrochem. Soc.* **2011**, *158* (5), 132–138. https://doi.org/10.1149/1.3560197.

(43) Temperton, R. H.; Gibson, A.; O'shea, J. N. In Situ XPS Analysis of the Atomic Layer Deposition of Aluminium Oxide on Titanium Dioxide. *Phys. Chem. Chem. Phys* **2019**, *21*, 1393. https://doi.org/10.1039/c8cp06912c.

(44) Rai, V. R.; Vandalon, V.; Agarwal, S. Influence of Surface Temperature on the Mechanism of Atomic Layer Deposition of Aluminum Oxide Using an Oxygen Plasma and Ozone. **2012**, *28*, 350–357. https://doi.org/10.1021/la201136k.

(45) Barbos, C.; Blanc-Pelissier, D.; Fave, A.; Blanquet, E.; Crisci, A.; Fourmond, E.; Albertini, D.; Sabac, A.; Ayadi, K.; Girard, P.; Lemiti, M. Characterization of Al2O3 Thin Films Prepared by Thermal ALD. *Energy Procedia* **2015**, *77*, 558–564. https://doi.org/10.1016/J.EGYPRO.2015.07.080.

(46) Dillon, A. C.; Ott, A. W.; Way, J. D.; George, S. M. Surface Chemistry of Al2O3 Deposition Using Al(CH3)3 and H2O in a Binary Reaction Sequence. *Surf. Sci.* **1995**, *322* (1–3), 230–242. https://doi.org/10.1016/0039-6028(95)90033-0.

(47) Heil, S. B. S.; Van Hemmen, J. L.; Van De Sanden, M. C. M.; Kessels, W. M. M. Reaction Mechanisms during Plasma-Assisted Atomic Layer Deposition of Metal Oxides: A Case Study for Al2O3. *J. Appl. Phys.* **2008**, *103* (10), 103302. https://doi.org/10.1063/1.2924406.

(48) Musschoot, J. Advantages and Challenges of Plasma Enhanced Atomic Layer Deposition. **2011**.

(49) Ratner, B. D.; Hoffman, A. S. Physicochemical Surface Modification of Materials Used in Medicine. In *Biomaterials Science: An Introduction to Materials: Third Edition*; Elsevier Inc., 2013; pp 259–275. https://doi.org/10.1016/B978-0-08-087780-8.00027-9.

(50) Mandler, D.; Turyan, I. Applications of Self-Assembled Monolayers in Electroanalytical Chemistry. *Electroanalysis* **1996**, *8* (3), 207–213. https://doi.org/10.1002/ELAN.1140080302.

(51) Bobb-Semple, D.; Nardi, K. L.; Draeger, N.; Hausmann, D. M.; Bent, S. F. Area-Selective Atomic Layer Deposition Assisted by Self-Assembled Monolayers: A Comparison of Cu, Co, W, and Ru. *Chem. Mater.* **2019**, *31* (5), 1635–1645.

https://doi.org/10.1021/acs.chemmater.8b04926.

(52) Chang, C.-W.; Hsu, H.-H.; Hsu, C.-S.; Chen, J.-T. Achieving Area-Selective Atomic Layer Deposition with Fluorinated Self-Assembled Monolayers . *J. Mater. Chem. C* **2021**, *9*, 14589. https://doi.org/10.1039/d1tc04015d.

(53) Pattison, T. G.; Hess, A. E.; Arellano, N.; Lanzillo, N.; Nguyen, S.; Bui, H.; Rettner, C.; Truong, H.; Friz, A.; Topuria, T.; Fong, A.; Hughes, B.; Tek, A. T.; DeSilva, A.; Miller, R. D.; Qiao, G. G.; Wojtecki, R. J. Surface Initiated Polymer Thin Films for the Area Selective Deposition and Etching of Metal Oxides. *ACS Nano* **2020**, *14* (4), 4276–4288. https://doi.org/10.1021/ACSNANO.9B09637.

(54) Yadav, P.; Gatensby, R.; Prochukhan, N.; C. Padmanabhan, S.; Davó-Quiñonero, A.; Darragh, P.; Senthamaraikannan, R.; Murphy, B.; Snelgrove, M.; McFeely, C.; Singh, S.; Conway, J.; O'Connor, R.; McGlynn, E.; Lundy, R.; Morris, M. A. Fabrication of High-κ Dielectric Metal Oxide Films on Topographically Patterned Substrates: Polymer Brush-Mediated Depositions. *ACS Appl. Mater. Interfaces* **2022**, *14* (28), 32729–32737. https://doi.org/10.1021/ACSAMI.2C07966/ASSET/IMAGES/LARGE/AM2C07966_0009.JPEG.

(55) Mcfeely, C.; Snelgrove, M.; Shiel, K.; Hughes, G.; Yadav, P.; Lundy, R.; Morris, M. A.; Mcglynn, E.; O'connor, R. Rapid Area Deactivation for Blocking Atomic Layer Deposition Processes Using Polystyrene Brush Layers. *J. Mater. Chem. C* **2022**, *10*, 7476. https://doi.org/10.1039/d2tc00577h.

(56) Odian, G.; Group, F. Principles of Polymerization, 4th Edition. *Mech. Eng.* **2004**, 832.

(57) J. Brandrup, E. H. I. and E. A. G. Polymer Handbook 2 Volumes Set. **1999**, 2366.

(58) Gad, S. E. Polymers. In *Encyclopedia of Toxicology: Third Edition*; Elsevier, 2014; pp 1045–1050. https://doi.org/10.1016/B978-0-12-386454-3.00912-X.

(59) P.Steven, M. *Polymer Chemistry: An Introduction*, Second Edi.; Oxford University Press, 1990.

(60) Sperling, L. H. *Introduction to Physical Polymer Science*, Fourth.; John Wiley & Sons, Inc.: Hoboken, NJ, 2006.

(61) YOUNG, R. J.; LOVELL, P. A. *INTRODUCTION TO POLYMERS, THIRD EDITION.*; CRC Press, 2011.

(62) Basic Polymer Structure | MATSE 81: Materials In Today's World https://www.e-education.psu.edu/matse81/node/2210 (accessed May 24, 2021).

(63) Pattison, T. G.; Hess, A. E.; Arellano, N.; Lanzillo, N.; Nguyen, S.; Bui, H.; Rettner, C.; Truong, H.; Friz, A.; Topuria, T.; Fong, A.; Hughes, B.; Tek, A. T.; DeSilva, A.; Miller, R. D.; Qiao, G. G.; Wojtecki, R. J. Surface Initiated Polymer Thin Films for the Area Selective Deposition and Etching of Metal Oxides. *ACS Nano* **2020**, *14* (4), 4276–4288. https://doi.org/10.1021/acsnano.9b09637.

(64) Tseng, Y. C.; Peng, Q.; Ocola, L. E.; Elam, J. W.; Darling, S. B. Enhanced Block Copolymer Lithography Using Sequential Infiltration Synthesis. *J. Phys. Chem. C*

2011, *115* (36), 17725–17729. https://doi.org/10.1021/jp205532e.

(65) Peng, Q.; Tseng, Y. C.; Darling, S. B.; Elam, J. W. A Route to Nanoscopic Materials via Sequential Infiltration Synthesis on Block Copolymer Templates. *ACS Nano* **2011**, *5* (6), 4600–4606. https://doi.org/10.1021/nn2003234.

(66) Tseng, Y. C.; Peng, Q.; Ocola, L. E.; Czaplewski, D. A.; Elam, J. W.; Darling, S. B. Enhanced Polymeric Lithography Resists via Sequential Infiltration Synthesis. *J. Mater. Chem.* **2011**, *21* (32), 11722–11725. https://doi.org/10.1039/c1jm12461g.

(67) Peng, Q.; Tseng, Y. C.; Long, Y.; Mane, A. U.; DiDona, S.; Darling, S. B.; Elam, J. W. Effect of Nanostructured Domains in Self-Assembled Block Copolymer Films on Sequential Infiltration Synthesis. *Langmuir* **2017**, *33* (46), 13214–13223. https://doi.org/10.1021/acs.langmuir.7b02922.

(68) Cummins, C.; Weingärtner, T.; Morris, M. A. Enabling Large-Area Selective Deposition on Metal-Dielectric Patterns Using Polymer Brush Deactivation. *J. Phys. Chem. C* **2018**, *122* (26), 14698–14705. https://doi.org/10.1021/acs.jpcc.8b04092.

(69) Cummins, C.; Shaw, M. T.; Morris, M. A. Area Selective Polymer Brush Deposition. *Macromol. Rapid Commun.* **2017**, *38* (16), 1700252. https://doi.org/10.1002/marc.201700252.

(70) What Is a Block Copolymer? https://www.thoughtco.com/definition-of-block-copolymer-604834 (accessed Mar 11, 2020).

(71) Black, C. T.; Ruiz, R.; Breyta, G.; Cheng, J. Y.; Colburn, M. E.; Guarini, K. W.; Kim, H. C.; Zhang, Y. Polymer Self Assembly in Semiconductor Microelectronics. *IBM Journal of Research and Development*. 2007, pp 605–633. https://doi.org/10.1147/rd.515.0605.

(72) Stoykovich, M. P.; Nealey, P. F. Block Copolymers and Conventional Lithography. *Mater. Today* **2006**, *9* (9), 20–29. https://doi.org/10.1016/S1369-7021(06)71619-4.

(73) Mai, Y.; Eisenberg, A. Self-Assembly of Block Copolymers. *Chem. Soc. Rev.* **2012**, *41* (18), 5969–5985. https://doi.org/10.1039/c2cs35115c.

(74) BATES, F. S. Polymer-Polymer Phase Behavior. *Science (80-.).* **1991**, *251* (4996), 898–905. https://doi.org/10.1126/science.251.4996.898.

(75) Bates, F. S.; Fredrickson, G. H. Block Copolymers—Designer Soft Materials. *Phys. Today* **1999**, *52* (2). https://doi.org/10.1063/1.882522.

(76) Bates, F. S.; Fredrickson, G. H. Block Copolymers—Designer Soft Materials. *Phys. Today* **1999**, *52* (2), 32–38. https://doi.org/10.1063/1.882522.

(77) Lynd, N. A.; Meuler, A. J.; Hillmyer, M. A. Polydispersity and Block Copolymer Self-Assembly. *Progress in Polymer Science (Oxford)*. Pergamon September 1, 2008, pp 875–893. https://doi.org/10.1016/j.progpolymsci.2008.07.003.

(78) Ghoshal, T.; Cruz-Romero, M. C.; Kerry, J. P.; Morris, M. A. Nanosize and Shape Effects on Antimicrobial Activity of Silver Using Morphology-Controlled Nanopatterns by Block Copolymer Fabrication. *ACS Appl. Nano Mater.* **2019**, *2* (10), 6325–6333. https://doi.org/10.1021/ACSANM.9B01286.

(79) Li, F.; Pincet, F. Confinement Free Energy of Surfaces Bearing End-Grafted Polymers in the Mushroom Regime and Local Measurement of the Polymer Density. *Langmuir* **2007**, *23* (25), 12541–12548. https://doi.org/10.1021/la7021374.

(80) Brittain, W. J.; Minko, S. A Structural Definition of Polymer Brushes. *J. Polym. Sci. Part A Polym. Chem.* **2007**, *45* (16), 3505–3512. https://doi.org/10.1002/pola.22180.

(81) Liu, G.; Ji, S.; Stuen, K. O.; Craig, G. S. W.; Nealey, P. F.; Himpsel, F. J. Modification of a Polystyrene Brush Layer by Insertion of Poly(Methyl Methacrylate) Molecules. *J. Vac. Sci. Technol. B Microelectron. Nanom. Struct.* **2009**, *27* (6), 3038–3042. https://doi.org/10.1116/1.3253607.

(82) Auroy, P.; Auvray, L.; Léger, L. Characterization of the Brush Regime for Grafted Polymer Layers at the Solid-Liquid Interface. *Phys. Rev. Lett.* **1991**, *66* (6), 719–722. https://doi.org/10.1103/PhysRevLett.66.719.

(83) Azzaroni, O.; Szleifer, I. *Polymer and Biopolymer Brushes: For Materials Science and Biotechnology*; 2017. https://doi.org/10.1002/9781119455042.

(84) Edmondson, S.; Osborne, V. L.; Huck, W. T. S. Polymer Brushes via Surface-Initiated Polymerizations. *Chem. Soc. Rev.* **2004**, *33* (1), 14–22. https://doi.org/10.1039/B210143M.

(85) Zdyrko, B.; Luzinov, I. Polymer Brushes by the “Grafting to” Method. *Macromolecular Rapid Communications*. June 16, 2011, pp 859–869. https://doi.org/10.1002/marc.201100162.

(86) de Paula, C.; Bobb-Semple, D.; Bent, S. F. Increased Selectivity in Area-Selective ALD by Combining Nucleation Enhancement and SAM-Based Inhibition. *J. Mater. Res.* **2021**, *36* (3), 582–591. https://doi.org/10.1557/S43578-020-00013-4.

(87) Bobb-Semple, D.; Zeng, L.; Cordova, I.; Bergsman, D. S.; Nordlund, D.; Bent, S. F. Substrate-Dependent Study of Chain Orientation and Order in Alkylphosphonic Acid Self-Assembled Monolayers for ALD Blocking. **2020**. https://doi.org/10.1021/acs.langmuir.0c01974.

(88) Lundy, R.; Yadav, P.; Selkirk, A.; Mullen, E.; Ghoshal, T.; Cummins, C.; Morris, M. A. Optimizing Polymer Brush Coverage To Develop Highly Coherent Sub-5 Nm Oxide Films by Ion Inclusion. *Chem. Mater.* **2019**, *31* (22), 9338–9345. https://doi.org/10.1021/acs.chemmater.9b02856.

(89) Snelgrove, M.; Mani-Gonzalez, P. G.; Bogan, J.; Lundy, R.; Rueff, J. P.; Hughes, G.; Yadav, P.; McGlynn, E.; Morris, M.; O’Connor, R. Hard X-Ray Photoelectron Spectroscopy Study of Copper Formation by Metal Salt Inclusion in a Polymer Film. *J. Phys. D. Appl. Phys.* **2019**, *52* (43). https://doi.org/10.1088/1361-6463/AB35B2.

(90) Peng, Q.; Tseng, Y. C.; Darling, S. B.; Elam, J. W. Nanoscopic Patterned Materials with Tunable Dimensions via Atomic Layer Deposition on Block Copolymers. *Adv. Mater.* **2010**, *22* (45), 5129–5133. https://doi.org/10.1002/ADMA.201002465.

(91) Subramanian, A.; Tiwale, N.; Nam, C. Y. Review of Recent Advances in Applications of Vapor-Phase Material Infiltration Based on Atomic Layer Deposition. *JOM* **2019**,

71 (1), 185–196. https://doi.org/10.1007/S11837-018-3141-4.

(92) Leng, C. Z.; Losego, M. D. Vapor Phase Infiltration (VPI) for Transforming Polymers into Organic–Inorganic Hybrid Materials: A Critical Review of Current Progress and Future Challenges. *Mater. Horizons* **2017**, *4* (5), 747–771. https://doi.org/10.1039/C7MH00196G.

(93) Biswas, M.; Libera, J. A.; Darling, S. B.; Elam, J. W. New Insight into the Mechanism of Sequential Infiltration Synthesis from Infrared Spectroscopy. *Chem. Mater.* **2014**, *26* (21), 6135–6141. https://doi.org/10.1021/cm502427q.

2 Principles of Experimental Techniques

The results presented in this work use a wide variety of experimental techniques and the following chapter outlines the theoretical and mechanical principles of each of the different techniques employed.

When investigating the chemical properties of the fabricated films – such as chemical bonding and elemental makeup, the photoemission techniques of X-ray photoelectron spectroscopy (XPS) and hard X-ray photoelectron spectroscopy (HAXPES) were used. These techniques allowed for the determination of polymer growth, successful polymer infiltration, material deposition as well as an assessment of the infiltrated materials post polymer removal. This was complemented using grazing angle attenuated total reflection Fourier transform infrared spectroscopy (GA-ATR-FTIR) for the determination of polymer deposition through organic bond vibrations.

Film thicknesses were determined through the use of ellipsometry which was vital for many aspects of the work presented. This was complemented through the use of X-ray reflectivity (XRR) which not only provided film thickness measurements but it also showed film density and film roughness. Assessing the film quality as well as surface roughness was also determined through the use of atomic force microscopy (AFM) once again providing very important information for the conducted work as high-quality films were of top priority. Finally, the use of contact angle was employed for the determination of surface functionalisation.

2.1 Grazing Angle Attenuated Total Reflection Fourier Transform Infrared Spectroscopy

2.1.1 Basic Theory

GA-ATR-FTIR is a characterisation method that allows for the arrangement of atoms and their associated chemical bonds to be analysed within a thin film [1,2]. This technique is based on the characteristic absorption of infrared (IR) light by specific molecules [3]. The frequency at which the IR light is absorbed is dependent on the effective mass of the molecule, $m_{eff,}$ as well as the bond strength between the atoms, k, which can be seen in the following;

$$\tilde{v} = \frac{1}{2\pi c}\left(\frac{k}{m_{eff}}\right)^{\frac{1}{2}} \qquad \text{Eqn(2.1)}$$

$$m_{eff} = \frac{m_1 m_2}{m_1 + m_2} \qquad \text{Eqn(2.2)}$$

Eqn(2.1) illustrates the oscillation frequency, $\tilde{v}$, of a molecule and shows its relationship to the bond strength and its effective mass [4]. It is this value that is used to determine the types of molecules present within a material as it is unique for each molecule and the environment it is in. Eqn(2.2) then shows an example calculation of the effective mass of a diatomic molecule, where m_1 and m_2 are the respective masses of the atoms present within the molecule. This highlights the dependence that the oscillation frequency has on the type of molecule and the atoms present within it. Using these equations an expected value for the frequency of IR light that would be absorbed can be determined. This is needed for the characterisation of materials as it allows for the chemical structure of a material to be established.

Upon absorption of IR radiation, bonds become excited and the molecule reaches a higher vibrational energy level. The energy of the vibrational levels for a given molecule can then be found as follows;

$$E_v = \left(n + \frac{1}{2}\right)\tilde{v} \qquad \text{Eqn(2.3)}$$

Where E_v is the energy value of the level and n is the energy level index (i.e. an integer starting at zero). Eqn(2.3) describes a bond as if it were behaving like a quantum harmonic oscillator. However, in a real-world case, a bond shows anharmonicity as there is a point in which the bond will break due to over stretching [5]. This means that Eqn(2.3) must be altered to reflect this anharmonicity,

$$E_v = \left(n + \frac{1}{2}\right)\tilde{v} - \left(n + \frac{1}{2}\right)^2 \chi_e\tilde{v} \qquad \text{Eqn(2.4)}$$

where χ_e is the anharmonicity constant. This shows that with increasing energy level the difference in the energy value between adjacent levels decreases [5]. Using these equations, the frequency of light required to excite a molecule into a higher energy level can be determined. This is required for the acquisition of an IR spectrum.

For the vibration of a molecule to be seen in an IR spectrum, there are two selection rules which must be obeyed otherwise the molecule will not absorb IR light and there would not be a change in vibrational state, causing no visible difference on an IR spectrum. These are as follows:

- The gross selection rule states for a molecule to change vibrational level by the absorption of electromagnetic radiation the electric dipole moment of that molecule must also change when the atoms are displaced relative to one another [4].

- The second selection rule, once the gross selection rule is met, is that there must be a change in the vibrational energy levels of +/-1.

Homonuclear molecules will not appear on an IR spectrum as their dipole moment does not change with atomic displacement. Thus, the molecule must be heteronuclear for there to be a change in dipole moment.

It is clear that each bond between different atoms will absorb IR light at different frequencies depending on the bond type, as well as the atoms within the molecule. This is what makes IR spectroscopy useful as it not only gives the chemical composition of a material but it also gives its molecular structure.

2.1.2 Technical Details

There are many differences between a standard IR grating spectrometer system and a Fourier transform infrared spectroscopy (FTIR) system, the main one being the inclusion of a Michelson Interferometer.

2.1.2.1 The Michelson Interferometer

The Michelson Interferometer is at the heart of any FTIR system. It consists of four main arms as can be seen in Figure 2.1. The first contains the IR source and a collimating mirror, which ensures that all light beams are parallel with each other. The second is a moving mirror, which is used to alter the distance travelled by the light going to it, and the light travelling to the fixed mirror which is on the third arm. The final arm has the sample being analysed and the detector. In the centre of all this is a beamsplitter which is the point where the IR light is separated allowing it to travel to both the fixed and moving mirrors. This is achieved by allowing a portion of the light to be reflected and the other transmitted [3].

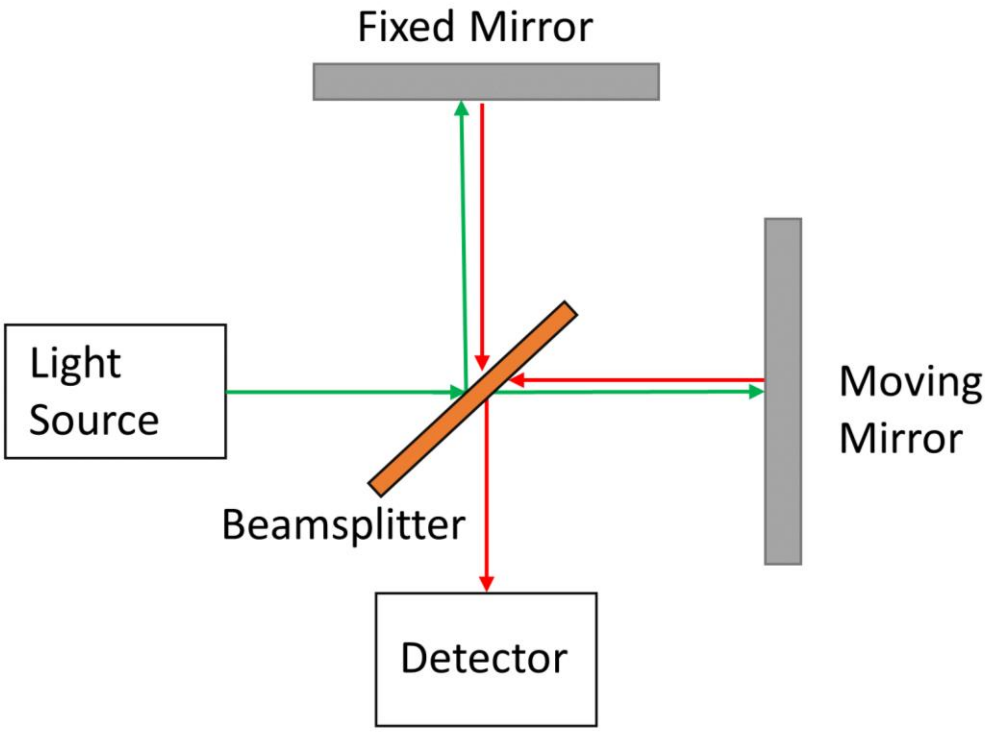

Figure 2.1 Schematic diagram of the parts within a Michelson interferometer including the fixed mirror, moving mirror, beamsplitter, light source and detector.

After the beams have been initially separated, they travel to the two mirrors. In the case of the fixed mirror, the beam always travels the same distance meaning its phase stays consistent. However, in the case of the moving mirror, this distance can be altered. This alteration changes the phase of the light meaning that when the two beams recombine, they interfere. The nature of this interference is dependent on the distance that the movable mirror is set from the beamsplitter.

The interference pattern formed in the recombination creates a cosine intensity wave. The superposition of these patterns is then taken by the detector to obtain what is known as the interferogram of the spectrometer. The Fourier Transform comes into play at this point, as Fourier's theorem states that mathematical functions can be expressed as a superposition of sine and cosine waves [6]. So, in this case, the Fourier transform is applied to the interferogram to obtain its corresponding mathematical function which is observed as an absorbance spectrum. The effect of placing a sample before the detector simply alters the intensities of the interferogram. As the sample selectively absorbs the various wavelengths, which in turn are causing bond vibrations, the Fourier transform is then altered. An example of this would be if a Fourier transform was taken of a laser, a single line would be obtained at the wavenumber of that laser. If a sample was placed between the laser and the detector which absorbed this radiation there would no longer be a line present [3]. This is how absorbance spectra are created using a FTIR system.

2.1.2.2 Grazing Angle Attenuated Total Reflection Attachments.

There can be many attachments added to an FTIR system to change its functionality, making it suitable for different types of materials. An attenuated total reflection (ATR) attachment makes obtaining the FTIR spectra of thin films possible.

This works by passing IR light through an optically dense crystal, such as germanium or diamond, which has a high refractive index. This is then placed on top of a lower refractive index sample. The angle of incidence of the IR light must be at or above the critical angle of the system to ensure that internal total reflection can occur [7]. The total internal reflection in the optically dense crystal leads to the formation of what is known as an evanescent wave in the lower index sample [3]. The interaction with the evanescent wave means that the sample can absorb the IR radiation, if the frequency matches a vibrational transition, causing the bonds within to vibrate. The presence of multiple "bounces" (reflections) as the wave propagates along the higher index ATR crystal can lead to higher absorption levels, and the geometry of the system means that no additional sample preparation is required.

Obtaining a spectrum using an ATR attachment is similar to that of a normal FTIR system. As stated previously the sample must be placed on the surface of the crystal. To allow for sufficiently close contact, large mechanical pressure must be applied to the sample. Once internal reflection conditions are satisfied the evanescent wave enters the sample, and (depending on the material) the reflected wave in the higher index material attenuates. This attenuation is measured once the wave is reflected back into the system, reaching the detector. As stated above the absorbance of the wave alters the interferogram giving a characteristic spectrum [7]. A schematic showing the ATR setup can be seen below in Figure 2.2.

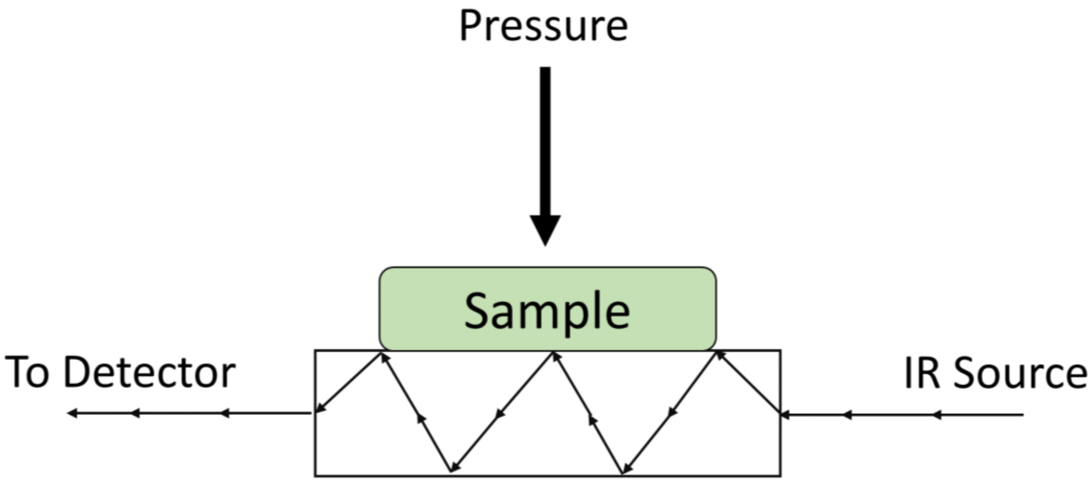

Figure 2.2 Basic illustration of how IR light travels through the optically dense crystal as well as a sample in an ATR-FTIR setup.

This technique is suitable for the analysis of thin films and is convenient since no additional sample preparation is required. In normal transmission IR spectroscopy, the amount of absorbance is dependent on the thickness of the material; the thicker it is the more bonds that are present giving larger absorbance intensities. Thus, using a normal FTIR system for thin films is not possible, as it is difficult to obtain suitable intensities within the spectrum. Using an ATR system, this thickness dependence can be overcome since the key parameter is the decay length of the evanescent wave (roughly the same order of magnitude as the optical wavelength). But when films reach ultrathin thicknesses (much less than the wavelength) the sample thickness is a limiting factor. It has been shown a significant enhancement of the absorption levels can be obtained through a specific arrangement of materials within an ATR system. Firstly, the optically dense material must be a very high refractive index material (in our case germanium) since a high critical angle is required. Secondly, the substrate the film is deposited on must be another material of higher refractive index than the sample (in our case silicon is ideal), as this allows for the creation of an optical cavity in which the analysis material is located. Finally, the angle of incidence must be above the critical angle of 60^o. The Fresnel equations in such a configuration indicate a large enhancement of the intensity of the evanescent wave in the sample material, due to phase effects which lead to electric field addition in the cavity due to the boundary conditions at the two interfaces. The field enhancement can easily be a factor of seven or more, and consequently ~ a factor of fifty in magnitude for the intensity, for very thin samples (in fact the field enhancement is larger for thin samples within a certain thickness range). The field enhancement means a consequent absorbance enhancement can be seen which allows for the analysis of such ultrathin films [1]. Since such a large angle of incidence is required this technique is known as grazing angle ATR[1,8] (sometimes called GA-ATR). When used in conjunction with an FTIR spectrometer, it is referred to as GA-ATR-FTIR.

2.2 X-Ray Photoelectron Spectroscopy

2.2.1 Basic Principle

XPS is a useful characterisation method that can provide both quantitative and qualitative information about the chemical composition of a material. It allows for the elements that a material is made of to be determined, as well as providing an understanding of the chemical environment the element is in [9].

XPS works based on the principle of the photoelectric effect. This occurs when an X-ray of sufficient energy is irradiated onto a material's surface and causes ionisation, which leads to the emission of a photoelectron. A schematic of this can be seen below in Figure 2.3.

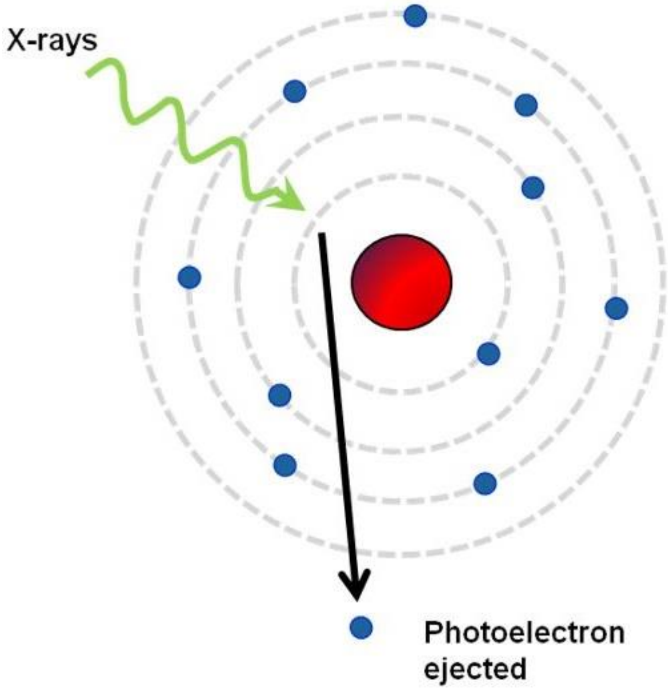

Figure 2.3 Illustration of the ionisation, and thus the creation of a photoelectron, of an atom caused by X-ray radiation [10].

Electron emission can only occur if the X-ray energy is greater than that of the binding energy of the electron. If the energy is sufficient and an electron is emitted, the ejected particle travels with kinetic energy, E_{kin}, which can be calculated as follows:

$$E_{kin} = hv - E_B - \phi \qquad \text{Eqn(2.5)}$$

where hv is the energy of the incident X-ray, ϕ is the work function of the spectrometer and E_B is the binding energy of the emitted electron [11]. A spectrometer measures the kinetic energy of these electrons and using Eqn(2.5) and the equivalent binding energy can then be determined. It is this binding energy that is used in the elemental characterisation of a material and is plotted against the number of electrons emitted at that binding energy otherwise known as the counts in an XPS spectrum.

2.2.2 Technical Details

2.2.2.1 Theoretical Basis

It is known that every electron within an atom has a specific binding energy, the value of which is dependent on several different factors. Firstly, the location of the electron within an atom influences its binding energy as electrons within the inner shells, such as the 1s, have a higher binding energy than those in the outer core levels [12]. A good example of this is comparing the binding energies of the electrons from the Al1s and the Al2p core levels as they have the binding energies of 1560 eV and 73 eV respectively [13]. It is clear from this comparison that the electrons in the inner core levels have a higher binding energy than those in the outer shells. It is also dependent on the element that it is being emitted from as the higher the atomic number of an element the larger the resulting binding energy [14]. For example, when comparing the binding energy of the Al2p and the Si2p emission lines they have binding energies of 73 eV and 99.4 eV respectively. It is this difference in both the binding energy of each core level and the element from which it comes from which allows for the detailed analysis of the elemental composition of a material.

The binding energy of an electron is also dependent on the chemical environment that the element is in. For example, the binding energy of the Si2p signal when silicon atoms are bonded to silicon atoms is 99.4 eV. Whereas the binding energy of the Si2p core level when silicon is bound to oxygen is 103.5 eV. This is due to the higher electronegativity that oxygen has over silicon which causes a shift in the electron density from the silicon towards the oxygen. This shift in electron density is known as the chemical shift. Since it is clear that the binding energy is dependent on its chemical environment this allows for detailed analysis not only of the chemical makeup of a material but also the bond interactions between each of the elements within it. This is achieved through peak fitting which will be discussed more in depth in section 2.2.3

2.2.2.2 Experimental Setup

Due to the nature of XPS, it is required to conduct these measurements in a UHV system with a pressure of up to $5x10^{-8}$ mbar. This is because key aspects of XPS analysis involve electron energy measurements and electron counting thus, conducting the experiment in a UHV environment allows for an increased mean free path for the emitted electrons.

The main components which make up an XPS system can be seen below in Figure 2.4. The X-ray source consists of tungsten filaments and an anode from which the X-rays are produced. This anode is typically made from Mg or Al which emit Kα X-rays with energies of 1253 eV and 1486 eV respectively [15]. The X-rays are generated through electron impact ionisation of the anode and these electrons are created from the filaments through thermionic emission. These electrons are accelerated towards the anode across a potential difference of approximately 14 kV allowing for the electrons to have sufficient energy for X-ray production.

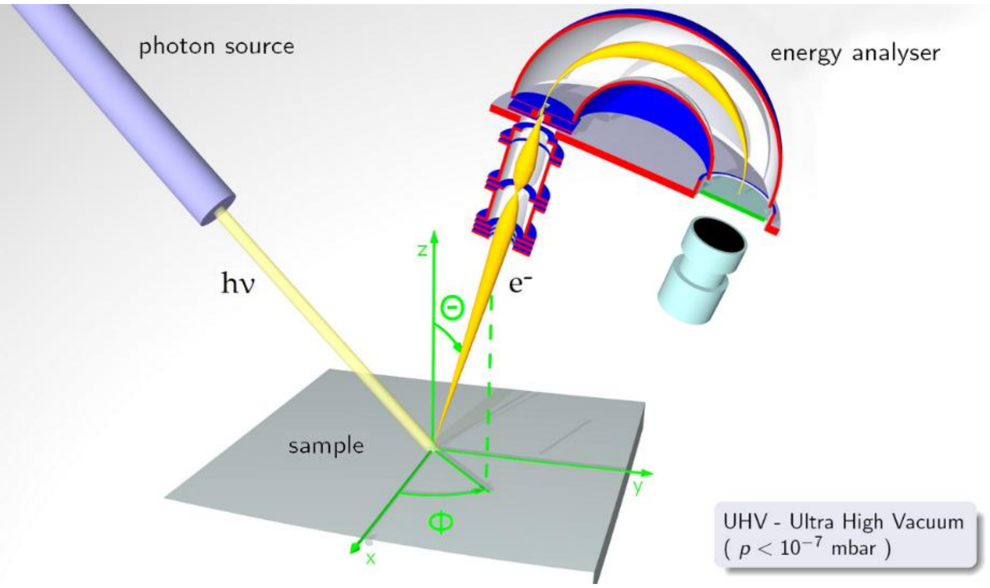

Figure 2.4 Configuration of components within an XPS system showing the X-ray source and the hemispherical analyser [16].

Once the generated X-rays impinge on a sample the photoelectrons produced are directed towards the energy analyser using a configuration of electron optics. The main component of these optics is the collector lens. This controls the area of analysis and the angle at which the electrons are accepted. After the collector lens, there are various lenses in place which lower the E_{kin} of the electrons before they enter the analyser at a fixed energy, which is known as the pass energy [9].

One of the final components of an XPS is the electron energy analyser. This analyser consists of two separate spheres which are held at different voltages. This creates a radially symmetric electric field which helps direct the electrons towards the detector. As previously mentioned, before entering the analyser the electrons are either accelerated or decelerated to a user-defined pass energy. This is the energy the electron has as it passes through the analyser. Altering the pass energy allows for changes in resolution. The lower the pass energy the higher the resolution. This has its disadvantages though since having a lower pass energy can reduce the electron counts [15].

2.2.3 XPS Data Analysis

2.2.3.1 Analysis Depth

XPS is widely known as being a very surface sensitive technique, analysing approximately the first 10 nm of a material [17]. This is due to the fact that the photoelectrons that are ejected from atoms deeper within a material have a larger distance, *d*, to travel to escape the sample surface. In doing so these electrons tend to undergo inelastic collisions, recombination, and recapture in various excited states within the material, all of which reduce the number of escaping electrons from the bulk. These effects appear as an exponential attenuation function as the depth increases and can be represented in the Beer's law equation;

$$I_k = I_0 e^{(-d/\lambda_{IMFP} \cos\theta)} \qquad \text{Eqn(2.6)}$$

Where I_k and I_0 are the final and initial photoemission intensity respectively, λ_{IMFP} represents the inelastic mean free path (IMFP) which determines the distance travelled by a photoelectron within a solid before undergoing an inelastic collision and finally θ, which is the angle of emission with respect to the normal [18]. From this equation it is clear that when d is large enough the value of I_k becomes too small to measure confirming the surface sensitivity of XPS.

2.2.3.2 Elemental Compositions

One of the main ways in which XPS is used is to determine the elemental composition of a material. This shows the percentage amount of each element present within a material as the intensity of each core level peak correlates to the amount of that element that is present. The intensity, I , of a photoelectron peak from a homogenous solid is given by;

$$I = J\rho\sigma K\lambda \qquad \text{Eqn(2.7)}$$

Where J is the photon flux, ρ is the concentration of the atom in the solid, σ is the photoelectron cross section, K is a term which covers all instrumental factors and λ is the electron attenuation length. By assuming that the photon flux is constant, the σ, K, and λ terms can be incorporated into a single sensitivity factor, with each core level of each element having its own unique value. From these assumptions and ensuring that the film is homogenous the atomic percentage of each element within a material can be calculated as follows;

$$\%(A) = \left\{ \frac{I_A / F_A}{\Sigma(I/F)} \right\} \qquad \text{Eqn(2.8)}$$

Where $\%(A)$ is the percentage of element A within a material, I_A is the intensity of that element and F_A is the sensitivity factor [19]. This is very important and useful information that can be obtained from an XPS spectrum as in the field of surface science one can track the elemental changes of a material after exposure of various processes such as ALD.

2.2.3.3 Peak Fitting

Peak fitting is another extremely important form of data analysis when it comes to XPS. As previously discussed in section 2.2.2.1 the binding energy of an electron is influenced by the chemical environment that the element is in. The peaks within an XPS spectrum can be deconvoluted and ‘fitted’ to determine the chemical states that the given element is in. Figure 2.5 shows the fits of the C1s spectra for the polymers PS and PMMA. From this figure the clear chemical differences between the two polymers can be seen and determined through the fits applied.

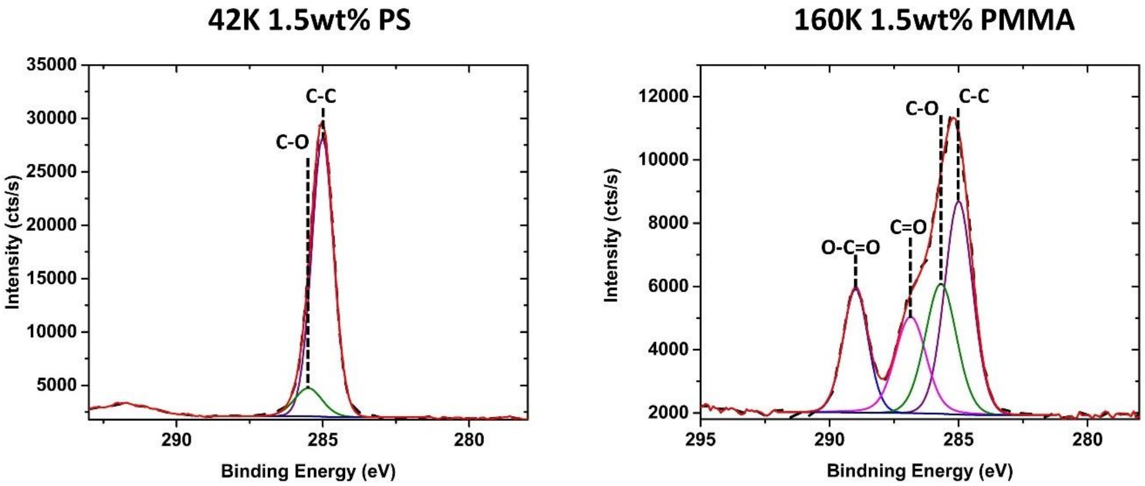

Figure 2.5 XPS C1s spectra for a 42K 1.5 wt% PS and a 160K 1.5 wt% PMMA and showing their applied fits. This illustrates the different chemical states that the carbon atoms are in within both of the polymer films.

Firstly, when looking at fitting an XPS spectrum, one has to take into account that each peak has a specific lineshape. This can be shown mathematically through a Voigt curve which is a combination of a Lorentzian and Gaussian function [20]. The equation for this is as follows;

$$\boldsymbol{\Gamma}_V = \sqrt{\boldsymbol{\Gamma}_{Gaussian}^2 + \boldsymbol{\Gamma}_{Lorentzian}^2}$$

Eqn(2.9)

Where $\boldsymbol{\Gamma}$ represents the full width half maximum (FWHM) of the peak. Both the Gaussian and Lorentzian FWHM values provide important information about each individual XPS peak.

Gaussian broadening is determined by several factors, including photon broadening and the non-perfect resolution of the photoemission analyser [21]. Gaussian broadening can be calculated using the following;

$$\boldsymbol{\Gamma}_{\boldsymbol{Gaussian}} = \sqrt{\boldsymbol{\Gamma}_c^2 + \boldsymbol{\Gamma}_a^2 + \boldsymbol{\Gamma}_p^2}$$

Eqn(2.10)

Where $\boldsymbol{\Gamma}_{\boldsymbol{c}}$, $\boldsymbol{\Gamma}_{\boldsymbol{a}}$ and $\boldsymbol{\Gamma}_{\boldsymbol{p}}$ are the FWHM values which account for the photon broadening. $\boldsymbol{\Gamma}_{\boldsymbol{a}}$ also takes into account the non-perfect resolution of the photoemission analyser and finally $\boldsymbol{\Gamma}_{\boldsymbol{p}}$

represents the spectral line width of the incident X-rays. Due to the fact that this broadening is influenced by system parameters it is therefore dependent on the individual tool being used. Lorentzian broadening on the other hand is determined solely by chemical effects within the element. From Heisenberg's uncertainty principle the emission of a photoelectron from an element creates a core-hole. The time in which it takes for this core-hole to be filled by an electron from another shell, otherwise known as its lifetime, determines the amount of Lorentzian broadening occurring. The Lorentzian FWHM can therefore be calculated using the following equation;

$$\Gamma_{Lorentzian} = \frac{h}{\tau} \qquad \text{Eqn(2.11)}$$

Where h is Planck's constant and τ is the core-hole lifetime. From Eqn(2.11) it is clear that the shorter the lifetime of a core-hole the larger amount of Lorentzian broadening experienced. The lifetime of these core-holes is influenced by the core in which it is created as inner shells have shorter lifetimes. Also, elements with larger atomic numbers have shorter core-hole lifetimes as they have more electrons present to fill these holes [22].

Another factor to consider when fitting XPS data is the background of the spectra, which refers to the parts of the spectrum which do not contain any photoemission peaks. The intensity of the background is generated from photoelectrons which have lost kinetic energy due to inelastic scattering events. XPS fitting software applies one of the following three options, the Tougaard, linear and Shirley backgrounds examples of which can be seen below in Figure 2.6.

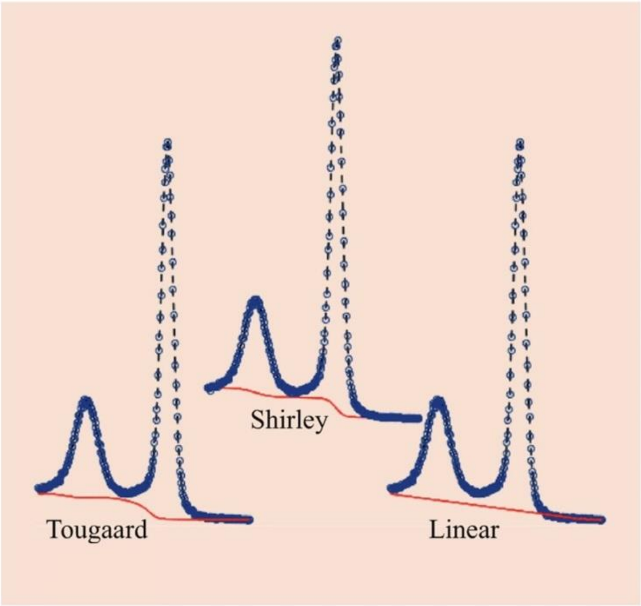

Figure 2.6 Graphical example of the Tougaard, Shirley and Linear backgrounds [23].

The linear background, as expected, applies a horizontal or sloped straight line from two points within the spectra. However, this is not ideal for detailed XPS fitting as the background is very rarely a straight line. The Tougaard background on the other hand is a mathematical model which takes into account the inelastic scattering of the background photoelectrons. This model works best when analysing larger regions but tends not to work with smaller more high-resolution areas. Finally, the Shirley background assumes that the background intensity at any given binding energy is proportional to the integrated intensity of the peak at lower binding energies. This was then further developed to create what is known as the Shirley-Sherwood background which performs iterations of the fitting process for further accuracy. This method is the best for analysing spectrally narrower regions [24].

2.3 Hard X-ray Photoelectron Spectroscopy

2.3.1 Basic Overview

HAXPES is an extension of the previously discussed XPS. It employs the same basic principles of XPS as it studies the electronic structure of solid materials through the use of the photoelectric effect. The main difference between HAXPES and XPS is the X-rays that are used. XPS uses what are known as soft X-rays whereas HAXPES uses higher energy hard X-rays ranging from 2 keV to 10 keV. The way in which these X-rays are produced are therefore also different with the soft X-rays being generated in an X-ray tube and the hard X-rays being created in a storage ring using synchrotron radiation [25].

2.3.2 Technical Details

As previously stated HAXPES uses X-rays generated via synchrotron radiation. This is produced when electrons are accelerated to relativistic speeds within a circular path. This radiation can be used for many purposes which include the generation of photons in the hard X-ray regime. An example of synchrotron ring can be seen in Figure 2.7 below.

Figure 2.7 Example of a synchrotron ring [26].

These particles are produced using an electron gun, with an energy of approximately 100 MeV, which are injected into a booster ring where they are brought up to 2.75 GeV. The electrons are then brought into a storage ring where they are guided by a series of magnets to maintain their circular trajectory. As the electrons move along the storage ring, they experience centripetal acceleration due to the magnetic fields. This acceleration causes the electrons to emit electromagnetic radiation tangentially to their path. It is this radiation that can then be used for the various analysis techniques such as HAXPES [25].

2.3.3 HAXPES Advantages

As mentioned in section 2.2.3.1, XPS is an extremely surface sensitive technique, with an analysis depth of approximately 10 nm which is down to the lower energy X-rays used in conventional XPS. Since HAXPES uses hard X-rays in the range of 2 keV to 10 keV a larger penetration depth is achievable. This is due to the fact that the photoelectrons emitted from a sample have a higher E_{kin} when produced with higher energy X-rays. From Eqn(2.6) the correlation between the E_{kin} of a photoelectron and the IMFP can be seen. It shows that with the large E_{kin} value the IMFP increases, thus allowing for photoelectrons deeper within the bulk to escape a material's surface without energy loss for analysis.

The use of the higher energy electrons as well as the larger penetration depth achieved by HAXPES allows for it to have many advantages over conventional XPS. Firstly, it permits for a greater amount of information to be obtained from the sample as a whole since more bulk signal is provided. It also allows for greater peak intensities to be obtained as a larger number of photoelectrons are able to escape allowing for higher resolution spectra. The tuneable X-ray energies of HAXPES allows for depth profiling analysis to be conducted as a change in the photon energy changes the sampling depth of the system. Finally, the use of higher energy X-rays allows for the extraction of more core level information. This is very useful as in some cases core levels can overlap between different elements or there are cases where one core level is easier to fit and deconvolute when compared to another. An example of this is the Al2p and Al1s signals. The Al2p is very weak and difficult to study, when compared the Al1s on the other hand which is much easier to fit but due to its higher binding energy value it can only be obtained with HAXPES and not conventional XPS.

2.4 Contact Angle

2.4.1 Basic Theory

Obtaining the contact angle of a material is a method used to determine its wettability. This refers to how a liquid deposited on a substrate acts, whether it spreads over the surface forming a thin layer or whether it makes a boundary, creating a droplet like structure. The wettability of a material is dependent on the surface tension between substrate, liquid and vapour as well as the attractive and repulsive forces between the liquid and the solid surface [27,28]. This translates to surface wettability, as for a material to be highly wetting the surface energy must be greater than the cohesive forces of the liquid thus causing it to spread out over the surface. Similarly, this applies to surfaces that are not wetting, where the cohesive forces of the liquid are stronger than the surface energy of the material meaning that the liquid forms the aforementioned droplet like structure [28].

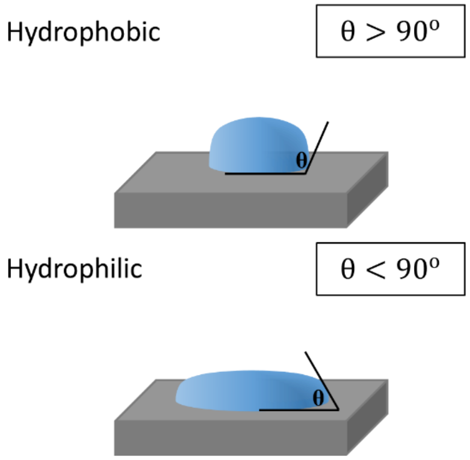

Figure 2.8 Schematic representation of the contact angles of a hydrophobic and hydrophilic surface.

Determining the wettability through contact angle is done by measuring the value of the angle formed by the line tangential to the droplet surface. If the angle is less than 90° then the material is considered highly wetting, otherwise known as hydrophilic. If the angle is greater than 90° the material is non wetting, otherwise known as hydrophobic. An example of the contact angles of a hydrophilic and hydrophobic surface can be seen in Figure 2.8.

2.4.2 Angle Determination

The contact angle of a material is determined by the geometry of a liquid droplet on a solid surface, specifically, the angle made between the line tangential to the edge of the liquid droplet and the applied surface. This can be seen above in Figure 2.8. As previously stated, the contact angle can be determined through the surface tension between the liquid-vapour interface, solid vapour interface and the liquid-solid interface. This can be seen through Young's equation;

$$\cos\theta = \frac{\sigma_{sv} - \sigma_{sl}}{\sigma_{lv}} \qquad \text{Eqn(2.12)}$$

Where θ is the contact angle, σ_{lv} is the surface tension of the liquid and vapour, σ_{sv} is the surface tension of the solid and vapour, and σ_{sl} is the surface tension of the solid and liquid [29]. Using Young's equation various surface tension values can be determined for a particular material or liquid if the angle is known.

Measuring the contact angle of a material can be highly useful in the field of materials research. This is due to the fact that the surface energy of a material can be altered using methods such as a plasma treatment or through the use of piranha solution. These can be done to increase the wetting of the material thus increasing its surface energy. The change in contact angle can therefore be used to determine the effectiveness of these treatments in terms of surface functionalisation. The same can be done for the analysis of thin films. In the case of polymer brushes, the addition of this layer alters the surface energy of the substrate making it the surface energy of the polymer. If a good quality and continuous film is in place the contact angle should be that of the polymer itself [30].

2.5 Atomic Force Microscopy

2.5.1 Basic Theory

AFM is a widely used method for the analysis of thin film surface morphology in three-dimensional detail [31]. In AFM, imaging the surface is not characterised in the same way as optical microscopy, through shadows or reflections, but rather for each point on the surface, a height measurement is made using a solid force probe [32]. The main components of an AFM are a flexible cantilever with the aforementioned solid force probe attached, a laser source and a four-quadrant photodiode. The configuration of these components can be seen below in Figure 2.9.

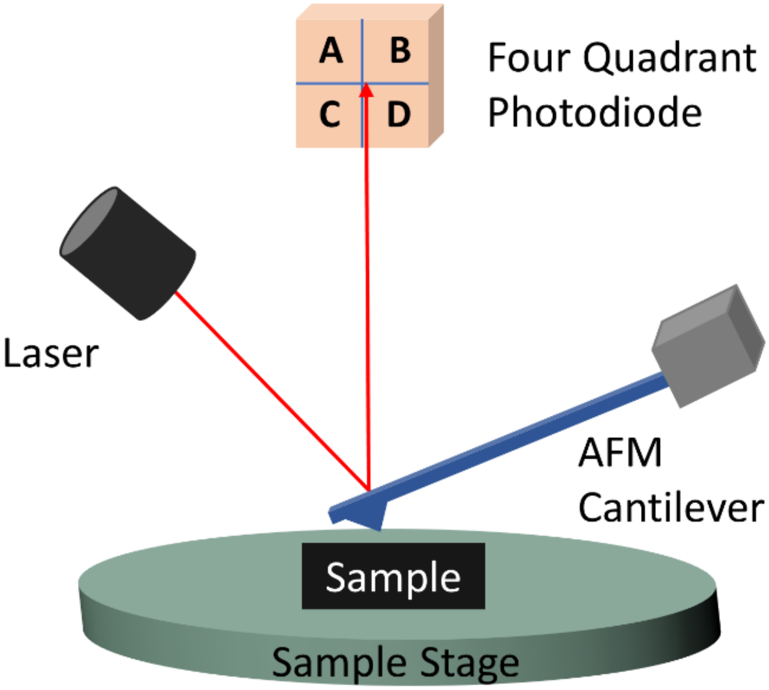

Figure 2.9 Basic structure of an AFM setup including the laser, cantilever and four quadrant photodiode.

This arrangement works to provide height information, as the laser is shone onto the cantilever and then is reflected to the photodiode. The probe is then traced over the surface of the substrate in a raster scanning process. As the probe moves across the surface the cantilever is moved up and down depending on the surface morphology. This movement alters the reflection of the laser light onto the photodiode thus allowing the surface to be mapped and imaged. The force that causes this movement can be described using Hooke's Law,

$$F = -kx \qquad \text{Eqn(2.13)}$$

where F is the force, k is the spring constant and x is the cantilever deflection. This force is used to produce a three-dimensional image of the material by tracking the deflection of the cantilever.

2.5.2 Modes of Operation

There are three main operational modes used in AFM imaging these are contact mode, tapping mode and non-contact mode.

2.5.2.1 Contact Mode

As the name suggests, in contact mode the probe is constantly in contact with the surface of the sample, meaning that whenever there is a change in height the cantilever will bend thus changing the value of the force. This alteration in the force value is what allows for an image to be obtained [32]. Contact mode is the most useful for fast image capturing however, with the probe being in constant close proximity to the surface, both the sample surface and the probe run the risk of being damaged. That is why this mode is used for harder and more robust surfaces which have a lower risk of being damaged.

2.5.2.2 Tapping Mode

In tapping mode, the cantilever is excited to its resonant frequency by a piezo driver at a larger distance away from the sample surface. In this mode, the tip does come into contact with the surface for very short periods of time in a tapping like motion. When the probe interacts with the surface, the absolute value of both the resonant frequency and its amplitude is changed. The image data is then acquired by keeping the frequency constant while the probe is passing over the sample surface and measuring the changes in height needed to ensure a constant frequency[33].

As well as the basic height images, the amplitude and phase images can also be obtained. Amplitude imaging can provide high contrast between the various surface features. It is mapped by tracking the voltage change required to keep the amplitude of the cantilever constant. Phase imaging can provide information on the chemical composition of the material allowing the various areas that are made up of different materials to be mapped. This information is obtained by measuring the phase difference between the driven oscillation of the cantilever [34]. This makes tapping mode one of the most used modes in AFM imaging as it provides various pieces of information besides just the height image. It also is suitable to use with more delicate materials as it is only in contact with the sample surface for a short time thus causing little to no damage.

2.5.2.3 Non-Contact Mode

In this mode, the cantilever oscillates at its resonant frequency near the surface of the sample but it never comes into direct contact with the sample, unlike the contact and tapping modes. The repulsive nature between the surface and the probe causes the deflection of the cantilever which can be monitored as the probe is scanned, which allows for the formation of an image.

The spatial resolution of this mode is lower compared to contact and tapping mode due to the larger separation between the surface and the probe. This mode is only used in the case of extremely deformable surfaces.

2.5.3 Roughness Calculations

One of the most important pieces of information concerning this work that AFM images can provide is surface roughness. This information is used to determine the quality of the polymer brush layers. The software used in this work for this calculation is Gwyddion [35].

The main value for roughness used is the root mean square (RMS) roughness which represents the standard deviation of the surface heights;

$$RMS = \sqrt{\frac{1}{N}\sum_{j=1}^{N} r_j^2} \qquad \text{Eqn(2.14)}$$

This value provides a measurement sensitive to the peaks and valleys in a sample surface making it very useful in the determination of film quality [34,36].

2.6 Ellipsometry

2.6.1 Basic Theory

Ellipsometry is a powerful characterisation method that allows the thickness of thin films on reflective surfaces, such as silicon, to be determined [37]. This method works based on the change in the polarisation of a light beam as it travels through a thin film and is reflected off the substrate surface. This is represented as an amplitude ratio, ψ, and a phase difference, Δ, which is dependent on both the thickness of the thin film as well as its optical constants [38,39]. The ellipsometer measures this ratio and using a mathematical model the thickness of these films can then be calculated.

The polarisation of light describes the electric field behaviour of the beam. If the electric field has completely random orientation and phase, it is described as unpolarised. Whereas if two orthogonal light waves are in phase the light is then described as being linearly polarised. If the waves are 90^{o} out of phase but are equal in amplitude then the light is circularly polarised. Finally, the most common form of polarised light, and the light that is used in the case of ellipsometry, is elliptically polarised. This combines the characteristics of both linearly and circularly polarised light as it has both arbitrary phase and amplitude [39]. When the light is polarised, it consists of s and p polarised light and it is these components in which ellipsometry is mainly interested.

An ellipsometer consists of the following major parts: light source, polarisation generator, sample, polarisation analyser and detector. The optical equipment, which is designed to alter and measure the polarisation of the light consists of polarisers, compensators and phase modulators [39]. The arrangement of these components can be seen below in Figure 2.10.

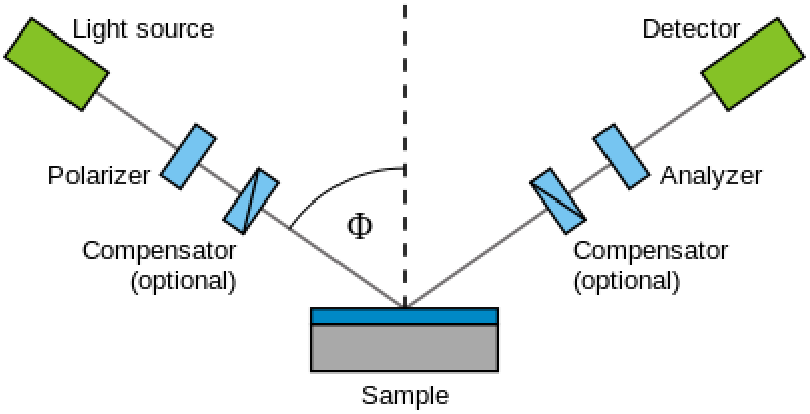

Figure 2.10 Schematic setup of an ellipsometers components [40].

2.6.2 Ellipsometry Models

Ellipsometry measurements alone tend not to yield much information and it is for this reason that a model of the materials system is needed to determine the desired quantities. The model works by calculating a predicted response of a materials system (single layer or multi-layer) based on Fresnel's equations, which describe each material with its thickness and optical constants. The information required for the thickness calculation of a specific material is the light path length and the refractive index of the material [38].

Figure 2.11 shows the schematics of light reflecting from a sample surface within an ellipsometer setup. The light beam is incident upon the sample surface with angle Φ which is equal to the angle of the reflected beam [41].

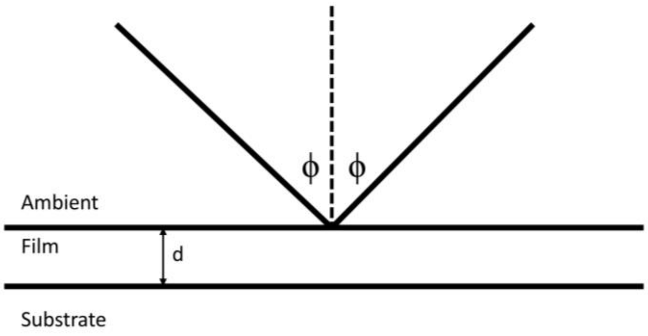

Figure 2.11 Schematic representation of light reflecting through the surface of a thin film in an ellipsometer setup.

If the sample surface is isotropic (i.e. having no film layer on top of it) then one can use the Maxwell equations to calculate the complex reflection coefficients,

$$r_p = \frac{n_s \cos(\phi_0) - n_0 \cos(\phi_s)}{n_s \cos(\phi_0) + n_0 \cos(\phi_s)} \qquad \text{Eqn(2.15)}$$

$$r_s = \frac{n_0 \cos(\phi_0) - n_s \cos(\phi_s)}{n_0 \cos(\phi_0) + n_s \cos(\phi_s)} \qquad \text{Eqn(2.16)}$$

where r_p and r_s represents the complex reflection coefficients which are p and s polarised respectively. The s polarisation refers to the polarisation of the wave's electric field normal to the plane of incidence and the p polarisation refers to the polarisation of the electric field in the plane of incidence. n_0 and n_s are the complex indices of refraction for the ambient and the substrate, respectively. If the sample consists of a single thin film atop a reflective substrate the complex reflection coefficients are written as follows:

$$r_{s,p} = \frac{r_{1s,p} + r_{2s,p} e^{-2ib}}{1 + r_{1s,p} r_{2s,p} e^{-2ib}} \qquad \text{Eqn(2.17)}$$

$$b = \frac{2\pi \mathrm{d} n_f \cos(\phi_f)}{\lambda} \qquad \text{Eqn(2.18)}$$

where d is the film thickness, n_f is the complex refractive index of the film and ϕ_f is the complex angle within the film. The quantities $r_{1s,p}$ and $r_{2s,p}$ are the complex reflection coefficients calculated using Eqn(2.15) and Eqn(2.16) for the air-film interface and the film-substrate interface respectively [41]. By using these equations and fitting experimental ellipsometry data with the refractive indices and layer thicknesses as fit parameters, an ellipsometer is capable of measuring the thickness of a thin polymer film on top of a silicon substrate.

2.7 X-ray Reflectivity

2.7.1 Basic Principle

XRR is an analysis technique used for the detailed study of surface properties of a material. It works through the measurement of reflected X-ray intensities from a sample surface. This technique can be used to obtain information about a material such as thin film thickness, surface roughness and density [42].

XRR works through the measurement of reflected X-rays as a function of incidence angle over a range of different angles that are close to the critical angle of the material. This is heavily dependent of the refractive index of a material which in the case of X-ray radiation is slightly less than one [43]. When electromagnetic radiation passes from air, which has a refractive index of one to a reflecting material with a refractive index of less than one, it is possible for total external reflection to occur if the angle is smaller than the critical angle [44]. If the surface is not perfectly smooth then the reflected intensity will deviate from what is predicted using Fresnel's equation. In this case the X-ray reflectivity can be approximated as follows [45];

$$R(Q)/R_F(Q) = \left|\frac{1}{\rho}\int_{-\infty}^{\infty} e^{iQz}\left(\frac{d\rho_e}{dz}\right)dz\right|^2 \qquad \text{Eqn(2.19)}$$

Where $\rho_e(z)$ is the average electron density, $R(Q)$ is the reflectivity, $Q = 4\pi sin(\theta)/\lambda$, λ is the X-ray wavelength, ρ_∞ is the density deep within the material and θ is the angle of incidence. When analysing a material which has an ideally flat surface the reflectivity of the material suddenly decreases when the angle of incidence rises above the critical angle. This is due to a larger number of X-rays penetrating deeper into the sample rather than being reflected from the surface. When the sample surface is rougher the reflectivity of the surface decreases more rapidly with the rise in incident angle. This means that within an XRR graph the slope of the graph indicates the roughness of the sample with a larger slope being attributed to a larger roughness value [46].

At every interface of individual films where there is a change in electron density only parts of the X-ray beam are reflected. This change in electron density causes the reflected X-rays to interfere with each other. This happens as when the X-rays are reflected from the different surfaces, they travel different distances thus having different phases. This interference can happen either constructively or destructively and this phenomenon is what creates the oscillation pattern, known as Kiessig fringes, seen in data analysis. The vertical properties of the spectrum indicate the thickness of the material through the periodicity of the oscillation pattern. While the depth of the oscillations indicates the films density [47]. An example of an XRR spectrum showing the results taken from a 1.5 wt% 160K PMMA sample and the information that can be drawn from it can be seen below in Figure 2.12.

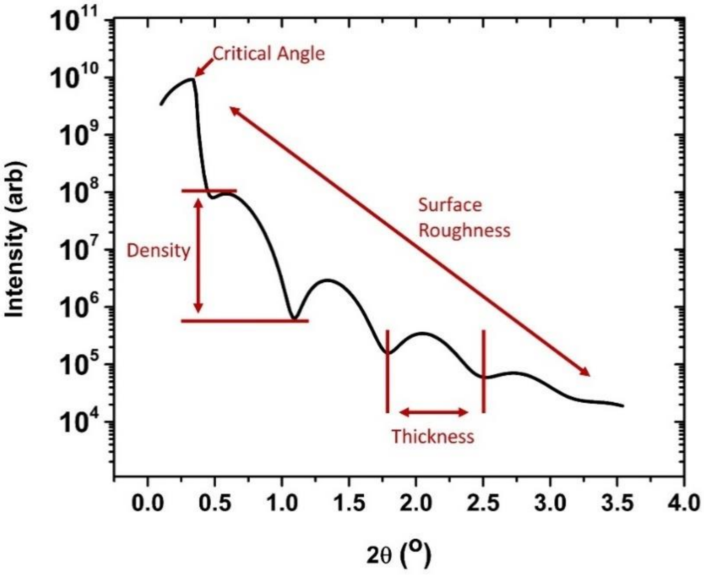

Figure 2.12 XRR spectrum of a 1.5 wt% 160K PMMA sample highlighting the information one can take from an XRR spectrum.

2.8 References

(1) Milosevic, M. Grazing Angle ATR (GAATR) Spectroscopy. In *Internal Reflection and ATR Spectroscopy*; John Wiley & Sons, Inc., 2012; pp 136–146. https://doi.org/10.1002/9781118309742.ch13.

(2) Chapter 3 Theory of Infrared Spectroscopy. *Comprehensive Analytical Chemistry*. Elsevier January 1, 2001, pp 19–40. https://doi.org/10.1016/S0166-526X(01)80006-4.

(3) Smith, B. C. *Fundamentals of Fourier Transform Infrared Spectroscopy, Second Edition*, Second.; CRC Press: London, 2011.

(4) Atkins, P.; de Paula, J. Atkins' Physical Chemistry. In *Atkins' Physical Chemistry*; Oxford University Press: Great Britain, 2006; pp 452–457.

(5) Banwell, C. N.; McCash, E. M. *Fundamentals of Molecular Spectroscopy*, 4th Editio.; McGraw Hill: London, 1994.

(6) Fourier Series -- from Wolfram MathWorld https://mathworld.wolfram.com/FourierSeries.html (accessed Jun 10, 2021).

(7) FTIR Sample Techniques: Attenuated Total Reflection (ATR) - IE.

(8) Milosevic, M. Internal Reflection and ATR Spectroscopy. https://doi.org/10.1081/ASR-200030195.

(9) van der Heide, P. *X-Ray Photoelectron Spectroscopy: An Introduction to Principles and Practices*; John Wiley and Sons: Hoboken, NJ, USA, 2011. https://doi.org/10.1002/9781118162897.

(10) Understanding Surface Properties Using XPS https://www.mccrone.com/mm/surface-properties-using-xps/ (accessed Jun 10, 2021).

(11) Hüfner, S. Introduction and Basic Principles; 2003; pp 1–60. https://doi.org/10.1007/978-3-662-09280-4_1.

(12) Electron binding energy | Radiology Reference Article | Radiopaedia.org https://radiopaedia.org/articles/electron-binding-energy (accessed Jul 28, 2021).

(13) Fadley, C. S. X-Ray Photoelectron Spectroscopy: Progress and Perspectives. *J. Electron Spectros. Relat. Phenomena* **2010**, *178–179* (C), 2–32. https://doi.org/10.1016/j.elspec.2010.01.006.

(14) Shpatakovskaya, G. V.; Karpov, V. Y. Atomic Number Scaling of Electron Spectra in the Free Atoms. *J. Phys. Conf. Ser.* **2016**, *774* (1), 012002. https://doi.org/10.1088/1742-6596/774/1/012002.

(15) Photoelectron Spectroscopy: Application - Chemistry LibreTexts https://chem.libretexts.org/Bookshelves/Physical_and_Theoretical_Chemistry_Textbook_Maps/Supplemental_Modules_(Physical_and_Theoretical_Chemistry)/Spectroscopy/Photoelectron_Spectroscopy/Photoelectron_Spectroscopy%3A_Application (accessed Apr 27, 2021).

(16) 5.3: Photoelectron Spectroscopy - Chemistry LibreTexts

https://chem.libretexts.org/Bookshelves/Physical_and_Theoretical_Chemistry_Textbook_Maps/Book%3A_Surface_Science_(Nix)/05%3A_Surface_Analytical_Techniques/5.03%3A_Photoelectron_Spectroscopy (accessed Jun 10, 2021).

(17) Dwyer, V. M.; Richards, J. M. The Depth Distribution Function in Auger/XPS Analysis. *Surf. Interface Anal.* **1992**, *18* (7), 555–560. https://doi.org/10.1002/SIA.740180717.

(18) Katona, L.; Bianchi, D.; Brenner, J.; Vorlaufer, G.; Vernes, A.; Betz, G.; Werner, W. S. M. Effect of Surface Roughness on Angle-Resolved XPS †. **2012**. https://doi.org/10.1002/sia.4886.

(19) Watts, J. F.; Wolstenholme, J. An Introduction to Surface Analysis by XPS and AES.

(20) Major, G. H.; Fernandez, V.; Fairley, N.; Smith, E. F.; Linford, M. R. Guide to XPS Data Analysis: Applying Appropriate Constraints to Synthetic Peaks in XPS Peak Fitting. *J. Vac. Sci. Technol. A* **2022**, *40* (6), 063201. https://doi.org/10.1116/6.0001975/2844339.

(21) Major, G. H.; Fairley, N.; Sherwood, P. M. A.; Linford, M. R.; Terry, J.; Fernandez, V.; Artyushkova, K. Practical Guide for Curve Fitting in X-Ray Photoelectron Spectroscopy. *J. Vac. Sci. Technol. A* **2020**, *38*, 61203. https://doi.org/10.1116/6.0000377.

(22) Vickerman, J. C.; Gilmore, I. S. Surface Analysis - The Principal Techniques: Second Edition. *Surf. Anal. - Princ. Tech. Second Ed.* **2009**, 1–666. https://doi.org/10.1002/9780470721582.

(23) Simon, P.; Baldovino-Medrano, V. G.; Wojcieszak, R. X-Ray Photoelectron Spectroscopy (XPS): Principles and Application for the Analysis of Photoactive Materials. *Springer Handbooks* **2022**, 249–271. https://doi.org/10.1007/978-3-030-63713-2_10/COVER.

(24) Tougaard, S. Practical Guide to the Use of Backgrounds in Quantitative XPS. *J. Vac. Sci. Technol. A* **2021**, *39*, 11201. https://doi.org/10.1116/6.0000661.

(25) *Hard X-Ray Photoelectron Spectroscopy (HAXPES)*; Woicik, J., Ed.; Springer Series in Surface Sciences; Springer International Publishing: Cham, 2016; Vol. 59. https://doi.org/10.1007/978-3-319-24043-5.

(26) Synchrotron - GISAXS http://gisaxs.com/index.php/Synchrotron (accessed May 15, 2023).

(27) Thomas Young, B.; For Sec, M. D. III. An Essay on the Cohesion of Fluids. *Philos. Trans. R. Soc. London* **1805**, *95*, 65–87. https://doi.org/10.1098/rstl.1805.0005.

(28) Kles, K. Contact Angles - Chemistry LibreTexts https://chem.libretexts.org/Bookshelves/Physical_and_Theoretical_Chemistry_Textbook_Maps/Supplemental_Modules_(Physical_and_Theoretical_Chemistry)/Physical_Properties_of_Matter/States_of_Matter/Properties_of_Liquids/Contact_Angles (accessed Feb 9, 2021).

(29) Cheng, P.; Quan, X.; Gong, S.; Liu, X.; Yang, L. Recent Analytical and Numerical

Studies on Phase-Change Heat Transfer. *Adv. Heat Transf.* **2014**, *46*, 187–248. https://doi.org/10.1016/bs.aiht.2014.08.004.

(30) Lundy, R.; Yadav, P.; Selkirk, A.; Mullen, E.; Ghoshal, T.; Cummins, C.; Morris, M. A. Optimizing Polymer Brush Coverage To Develop Highly Coherent Sub-5 Nm Oxide Films by Ion Inclusion. *Chem. Mater.* **2019**, *31* (22), 9338–9345. https://doi.org/10.1021/acs.chemmater.9b02856.

(31) Fundamental Theory of Atomic Force Microscopy http://www.nanoscience.gatech.edu/zlwang/research/afm.html (accessed Mar 11, 2020).

(32) Haugstad, G. *Atomic Force Microscopy Understanding Basic Modes and Advanced Applications*; 2012.

(33) Aliano, A.; Cicero, G.; Nili, H.; Green, N. G.; García-Sánchez, P.; Ramos, A.; Lenshof, A.; Laurell, T.; Qi, A.; Chan, P.; Yeo, L.; Friend, J.; Evander, M.; Laurell, T.; Lenshof, A.; Laurell, T.; Chen, J.; Lacroix, J. C.; Martin, P.; Randriamahazaka, H.; Barnes, W. J. P.; Hoogenboom, B. W.; Fukuzawa, K.; Hölscher, H.; Hölscher, H.; Bottos, A.; Astanina, E.; Primo, L.; Bussolino, F.; Gao, X.; Phan, V.-N.; Nguyen, N.-T.; Yang, C.; Abgrall, P.; Barth, F. G.; Gurman, P.; Rosen, Y.; Auciello, O.; Kähler, C. J.; Cierpka, C.; Rossi, M.; Bhushan, B.; Palacio, M. L. B.; Dezelah, C. L. AFM, Tapping Mode. In *Encyclopedia of Nanotechnology*; Springer Netherlands, 2012; pp 99–99. https://doi.org/10.1007/978-90-481-9751-4_33.

(34) De, R. R. L.; Albuquerque, D. A. C.; Cruz, T. G. S.; Yamaji, F. M.; Leite, F. L. Measurement of the Nanoscale Roughness by Atomic Force Microscopy: Basic Principles and Applications. In *Atomic Force Microscopy - Imaging, Measuring and Manipulating Surfaces at the Atomic Scale*; InTech, 2012. https://doi.org/10.5772/37583.

(35) Gwyddion – Free SPM (AFM, SNOM/NSOM, STM, MFM, …) data analysis software http://gwyddion.net/ (accessed Mar 29, 2021).

(36) Gadelmawla, E. S.; Koura, M. M.; Maksoud, T. M. A.; Elewa, I. M.; Soliman, H. H. Roughness Parameters. *J. Mater. Process. Technol.* **2002**, *123* (1), 133–145. https://doi.org/10.1016/S0924-0136(02)00060-2.

(37) Grainger, D. W.; Castner, D. G. Surface Analysis and Biointerfaces: Vacuum and Ambient in Situ Techniques. In *Comprehensive Biomaterials*; Elsevier, 2011; Vol. 3, pp 1–22. https://doi.org/10.1016/b978-0-08-055294-1.00082-9.

(38) What is Ellipsometry? - J.A. Woollam https://www.jawoollam.com/resources/ellipsometry-tutorial/what-is-ellipsometry?gclid=EAIaIQobChMIp_WNz52F5wIVCLrtCh1AowHkEAAYASAAEgIahPD_BwE (accessed Jan 15, 2020).

(39) Hilfiker, J. N.; Woollam, J. A. Instrumentation: Ellipsometry. In *Encyclopedia of Modern Optics, Five-Volume Set*; Elsevier Inc., 2004; pp 297–307. https://doi.org/10.1016/B0-12-369395-0/00833-2.

(40) File:Ellipsometry setup.svg - Wikimedia Commons https://commons.wikimedia.org/wiki/File:Ellipsometry_setup.svg (accessed Jun 10, 2021).

(41) Jellison, G. E. Ellipsometry. In *Encyclopedia of Spectroscopy and Spectrometry*; Elsevier, 1999; pp 402–411. https://doi.org/10.1006/rwsp.2000.0070.

(42) XRR: X-ray Reflectivity - - Diamond Light Source https://www.diamond.ac.uk/Instruments/Techniques/Diffraction/XRR.html (accessed Jan 10, 2023).

(43) Parratt, L. G. Surface Studies of Solids by Total Reflection of X-Rays. *Phys. Rev.* **1954**, *95* (2), 359–369. https://doi.org/10.1103/PHYSREV.95.359.

(44) Bracco, G.; Holst, B. Surface Science Techniques. *Springer Ser. Surf. Sci.* **2013**, *51* (1). https://doi.org/10.1007/978-3-642-34243-1.

(45) Als-Nielsen, J. (Jens); McMorrow, D. Elements of Modern X-Ray Physics. **2011**, 419.

(46) Pelliccia, D.; Kandasamy, S.; James, M. Characterization of Thin Films for X-Ray and Neutron Waveguiding by X-Ray Reflectivity and Atomic Force Microscopy. https://doi.org/10.1002/pssa.201330113.

(47) Miller, A. M.; Lemon, M.; Choffel, M. A.; Rich, S. R.; Harvel, F.; Johnson, D. C. Extracting Information from X-Ray Diffraction Patterns Containing Laue Oscillations. *Zeitschrift fur Naturforsch. - Sect. B J. Chem. Sci.* **2022**, *77* (4–5), 313–322. https://doi.org/10.1515/ZNB-2022-0020/PDF.

3 Investigation on the Variation of Polymer Brush Thickness through Various Methods

3.1 Introduction

The work presented in this chapter investigates two methods by which the thickness of polymer brushes composed of both PMMA, an active polymer, and PS, an inactive polymer, are varied. Both methods employed the grafting to approach for the fabrication process, details of which have been discussed in Section 1.2.6.1. As previously mentioned this method of brush fabrication has been shown to not yield as thick or as dense a polymer brush compared to the grafting from technique [1]. However, it is a much faster and less chemically intensive method of fabrication and it is for this reason a method for optimising the polymer film density and thickness is studied.

The motivation behind the desire for increased polymer film thicknesses using the grafting to approach is to further investigate the effect that thickness has on the infiltration and blocking properties of PMMA and PS respectively. For example, by achieving a very thick PMMA brush and exposing it to an infiltration process one could determine whether infiltration is occurring throughout the film or if the infiltrating material only penetrates the first few nanometres. This information would be vital for the understanding of how these polymers work in a BCP system for the fabrication of patterned substrates. Achieving this increased thickness using a simpler approach, such as the grafting to technique, allows for faster brush fabrication as well as making it more desirable to industry partners encouraging its further study.

The first process by which the polymer brush thickness was varied was based on changing the polymer molecular weight, which increased the length of the polymer chains, and the concentration of the solution, which increased the number of chains available for grafting, used to fabricate the brushes. Ellipsometry was used to determine the polymer brush thickness while GA-ATR-FTIR was used to look at the bond interactions as well as the chemical composition of these films to ensure sufficient polymer grafting. Finally, AFM was used to determine film quality by calculating the surface roughness of the brushes as well as imaging the surface. In the case of the PMMA brushes XRR was used to determine the density of the films as well as to confirm the film thickness and surface roughness. The results confirmed that with an increase in both the molecular weight and solution concentration there was an increase in the overall brush thickness.

The second method that was explored to vary the PS brush thickness employed a stepwise grafting to approach. This was achieved by combining the grafting to method with an O_2 plasma process post-film fabrication which was carried out using a Henniker bench top plasma system. This would achieve hydroxy termination of the polymer brush allowing for a second layer of PS to be applied. Achieving this stepwise process had its challenges as an O_2 plasma process is known not only to achieve hydroxy functionalisation but also for its ability to break down and remove polymer films [2–4]. An extremely gentle plasma process was used to obtain maximum functionalisation with minimal polymer breakdown, contact angle and ellipsometry measurements were used to show that this was achieved. GA-ATR-FTIR and AFM were then used to examine whether any chemical changes occurred within the film post plasma treatment as well as to determine film quality. Once a desirable process was found, a second layer was applied and ellipsometry was used to determine if further brush growth had occurred. It was seen that while the plasma process was able to successfully functionalise the polymer surface with minimal polymer removal there was no significant growth in film thickness once the second layer of the polymer solution was applied.

3.2 Experimental Details

3.2.1 Materials

Blanket silicon with native oxide was provided by our industrial collaborators (Intel). The polymers, hydroxy-terminated polystyrene (PS-OH) (of two molecular weights, specifically Mw = 16 kg mol^{-1} (16K) , PDI = 1.09 and Mw = 42 kg mol^{-1} (42K), PDI = 1.06) and hydroxy-terminated poly(methyl methacrylate) (PMMA-OH) (of three molecular weights, specifically Mw = 6 kg mol^{-1} (6K), PDI = 1.25; Mw = 45 kg mol^{-1} (45K) , PDI = 1.15 and Mw = 160 kg mol^{-1} (160K) , PDI = 1.15) were purchased from Polymer Source Inc. Canada and used as received. Toluene (anhydrous, 99.8%) and isopropyl alcohol (≥ 99.7%, FCC, FG) were purchased from Sigma Aldrich and used as received. Deionized water (resistivity = 18.2 MΩ cm) was also used.

3.2.2 Polymer Brush Fabrication

Silicon wafers were cleaved into 2 cm^2 pieces. They were ultrasonicated in isopropyl alcohol for 30 minutes to remove any residual dirt and dust. Once clean, the samples were dried using an N_2 gas stream. The silicon was hydroxy functionalised using a 3-minute O_2 plasma treatment conducted in a Henniker Plasma HPT-200 benchtop plasma treater. Both PS and PMMA were dissolved in toluene. These solutions ranged in concentration from 0.2-2 weight percent (wt%) and were left stirring overnight. After functionalisation, the polymer solutions were spin casted onto the silicon substrates. This was done at 3000 rpm for 30 seconds. Both PS molecular weights and 6K PMMA samples were then annealed on a hot plate at 200°C. The higher molecular weight PMMA was annealed at a higher temp of 230°C. Annealing temperatures were determined using the work conducted by Lundy *et. al.* which showed that samples needed to be annealed at or above the glass transition temperature of the polymer [5].

Samples were annealed at a range of times from 0.5 to 6 hours. Once annealed each sample was sonicated in toluene for 2 x 12-minute sonication periods. This was done to ensure all ungrafted polymer chains were removed making the polymer brush a monolayer. The samples were once again dried using an N_2 gas stream.

3.2.3 Plasma Processing

42K PS brushes were fabricated, using a 1.5 wt% solution, as described in section 3.2.2. Once the films were made, they were exposed to a variety of oxygen plasma processes in a Henniker Plasma HPT-200 benchtop plasma treater with an oxygen flow of 9 sccm. Plasma power levels of 200 W and 150 W were investigated. Process times were varied between 1 and 30 seconds. This was done to find the optimum plasma process which sufficiently functionalised the polymer surface while not breaking down the film. Once the optimal process was determined a second layer of PS was applied. The solution used was the same as the one used to fabricate the initial films. Application of the solution to the sample, as well as the annealing and sonicating processes, were consistent with the processes used to make the initial film. The annealing time and temperature, however, were varied to ensure optimal grafting. The temperatures and times were as follows, 200ºC, 230ºC and 250ºC for 0.5 hrs, 2 hrs and 6 hrs. All temperatures used, however, are below the degradation temperature of PS, being between 300ºC and 400 ºC [6], so there was no polymer breakdown.

3.2.4 Characterisation

Ellipsometry data was recorded using a J.A. Woolam XLS-100 ellipsometer. All data analysis was performed with the CompleteEASE software using a multi-layer model. This type of modelling was used to not only take into account the polymer films but also the silicon substrate as well as the silicon oxide intermediate layer. Within this model three layers were inputted, the silicon substrate, a 2 nm silicon oxide layer and finally the respective polymer layer. The optical constants for each layer were obtained from the CompleteEase software from pre-determined models as the films in this study are all well-known and analysed. In all cases, three measurements were taken from different points on the sample and an average of these was calculated. The standard error of this was also determined.

GA-ATR-FTIR was performed using a Nicolet iS50 FTIR Spectrometer with a Harrick VariGATR attachment with a germanium crystal. Before sample analysis, the crystal was cleaned using butanone to remove any dust from its surface. A background of the atmosphere was then taken. Each sample was placed face down onto the crystal and a force of approximately 600 N was applied, this was to ensure sufficient crystal sample contact. The sample was then scanned at an unpolarised angle of incidence of 65° for a total of 128 scans at 8 cm^{-1} resolution. Data analysis was conducted using OriginPro 2015. The main peaks seen within the two polymers studied and their associated bonds can be seen below in Table 3.1 [7,8].

Table 3.1 Main bonds detected within the polymer films investigated and their associated wavenumbers.

Bond	**Movement**	**Wavenumber (cm^{-1})**
O-H	Stretching	3550-3200
C-H	Stretching	2929, 1450
C=O	Stretching	1735
C=C	Stretching	1600
C-H	Bending	900
C-O	Stretching	1234

AFM images were obtained using a Bruker Icon AFM, using tapping mode with the Tap300 Al-G tips with a resonant frequency of 300 kHz and a force constant of 40 N/m. Image analysis and roughness calculations were then performed using Gwyddion.

XRR measurements took place at the I07 beamline of Diamond Light Source, Didcot, UK. An X-ray beamline with an energy of 10keV (λ = 1.241Å) and a spot size of 68 x 221 μm was used. Samples were mounted on the diffractometer stage enclosed in a plastic bag filled with argon to prevent surface damage by oxygen and ozone. All data analysis was then completed using the GenX software.

Finally, contact angle measurements were conducted using a Dataphysics OCA 15EC contact angle device, and the angles were then calculated using the Dataphysics SCA20 software.

3.2.5 Acknowledgements

The author would like to acknowledge that the sample preparation technique was acquired and developed by collaborators at the AMBER Institute, Trinity College Dublin [5]. The author would also like to thank the assistance given by Dr James Conway from the DCU School of Physical Sciences and NCPST in the plasma process design for this work.

3.3 Results

3.3.1 Poly(methyl methacrylate) Results

3.3.1.1 Ellipsometry

At the beginning of this work, the main focus was optimising the temperature and time used in the anneal step of the polymer brush fabrication process. This was done not only to fabricate the thickest brush possible for each of the solution combinations, but also to do so in a short period of time.

When fabricating the 6K PMMA a temperature of 200ºC was used for all weight percentages and the samples were annealed for 0.5, 2, and 6 hours. This temperature was used based on work conducted by collaborators at Trinity College Dublin who found it to be the most effective for the lower molecular weight PMMA. Figure 3.1 shows the ellipsometry results for the 6K PMMA brushes, illustrating the film thickness at a range of solution concentrations.

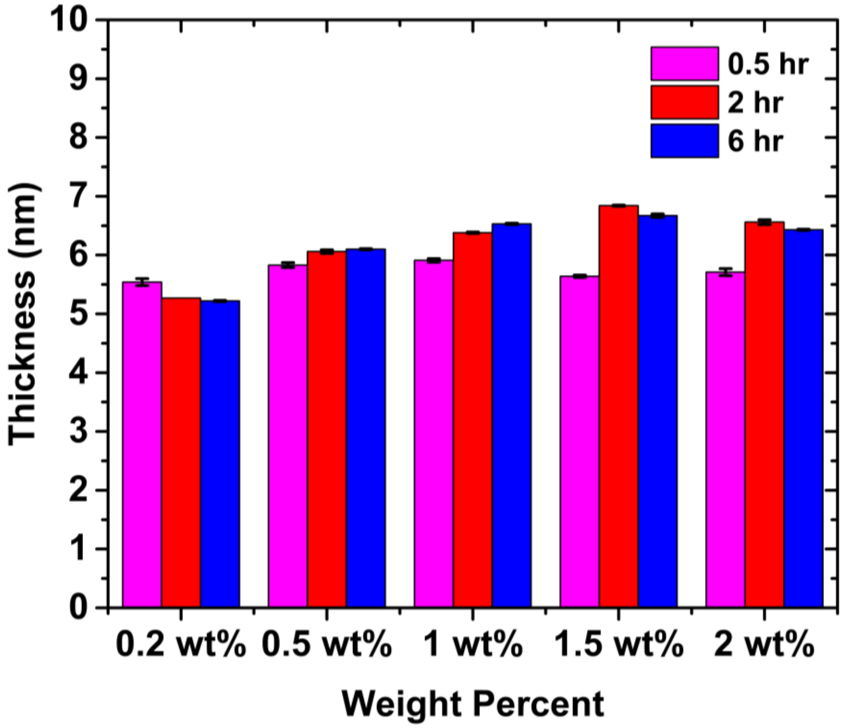

Figure 3.1 Ellipsometry results for the 6K PMMA samples over a range of weight percentages annealed for 0.5 hr, 2 hr and 6 hr. The error for each data set was determined through the calculation of the standard error of the mean value.

From the ellipsometry data, there was an increase in brush thickness with respect to solution concentration for the samples annealed for 2 and 6 hours. However, this increase stops at the 1.5 wt% sample as it can be seen that there is a small drop in thickness with the 2 wt% sample. It is proposed that this is due to the fact that there are too many chains present within the solution causing steric hinderance at the grafting sites, thus inhibiting polymer chain attachment. Overall, these results agree with the theory that with an increase in the solution concentration there should be an increase in grafting density, which is due to the larger amount of polymer chains available for attachment. However, this relationship is not observed for the samples annealed for 0.5 hours. This is due to an insufficient anneal time for the temperature used which led to poor grafting. While there is an increase in thickness it is obvious that there is not a large difference in these values. The thickest film obtained whilst using this annealing temperature was the 1.5 wt% sample which was annealed for 2 hours yielding a thickness of 6.84±0.08 nm. A brush this thin was expected as with lower molecular weight polymers, the chain length is significantly smaller leading to thinner brushes. An example of an ellipsometric fit for the 1.5 wt% film can be seen below in Figure 3.2 . This shows the goodness of the fit.

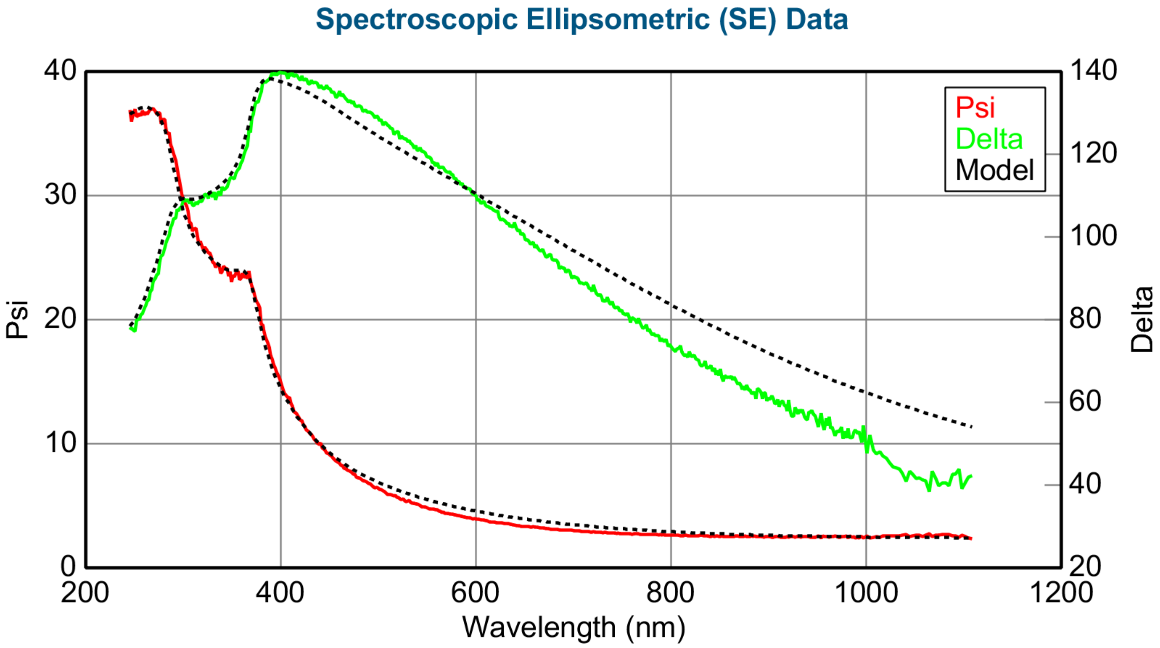

Figure 3.2 Ellipsometric fit for the 6K 1.5 wt% PMMA film.

Following the 6K study, brushes were fabricated using 45K PMMA to try to obtain thicker films. For these experiments, the annealing temperature was increased to 230°C. This was required, as in the literature it is shown that with an increase in molecular weight there is also an increase in the glass transition temperature, and as previously stated the annealing temperature must be above the glass transition temperature of the polymer [9]. The same range of annealing times was used as for the 6K PMMA. Figure 3.3 shows the ellipsometry results for the brushes fabricated using the higher molecular weight PMMA.

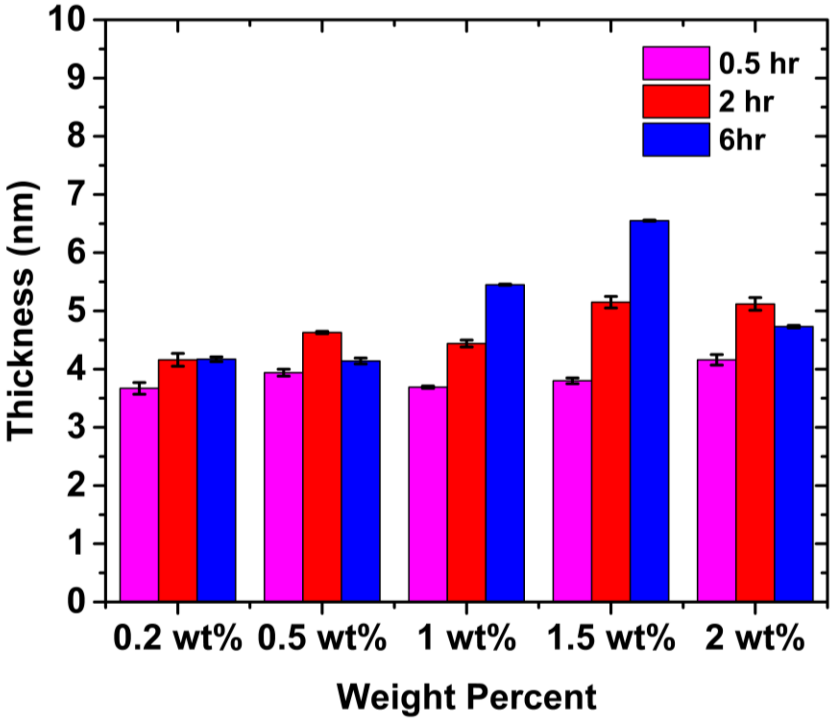

Figure 3.3 45K PMMA ellipsometry results over a range of solution concentrations, annealed for 0.5hr, 2hr and 6hr. From this data it can be seen that the films fabricated using the 1.5 wt% solution and annealed for 6 hours yielded the thickest brush.

From the results, there is not a large variance in thickness with respect to annealing time in the lower weight percent cases. As the solution concentration increases, however, there is a distinct increase in brush thickness with the annealing time. This can be seen, especially, in the 1.5 wt% case, where the sample annealed for 6 hours is thicker than the samples annealed for less time with a thickness of 7.92±0.13 nm. This indicates a better grafting density which is allowing the polymer chains to extend forming the thicker brushes. When comparing the thicknesses obtained with the 6K polymer and the 45K, there is not a large difference. This shows that the polymer chains were not extending as expected, this may be due to the grafting density as well as the physical properties of the PMMA [10]. While the increase in solution concentration allows for a larger amount of polymer chains to graft (which can be seen in Figure 3.1 and Figure 3.3) to the surface of the silicon, it is not sufficient for a full extension of the polymer chains. PMMA is also a very flexible polymer meaning chains could be potentially bending over and therefore creating a thinner brush. For this reason, a larger molecular weight was employed to investigate whether a larger increase in thickness could be achieved. An example of an ellipsometric fit for the 1.5 wt% film can be seen below in Figure 3.4. This shows the goodness of the fit.

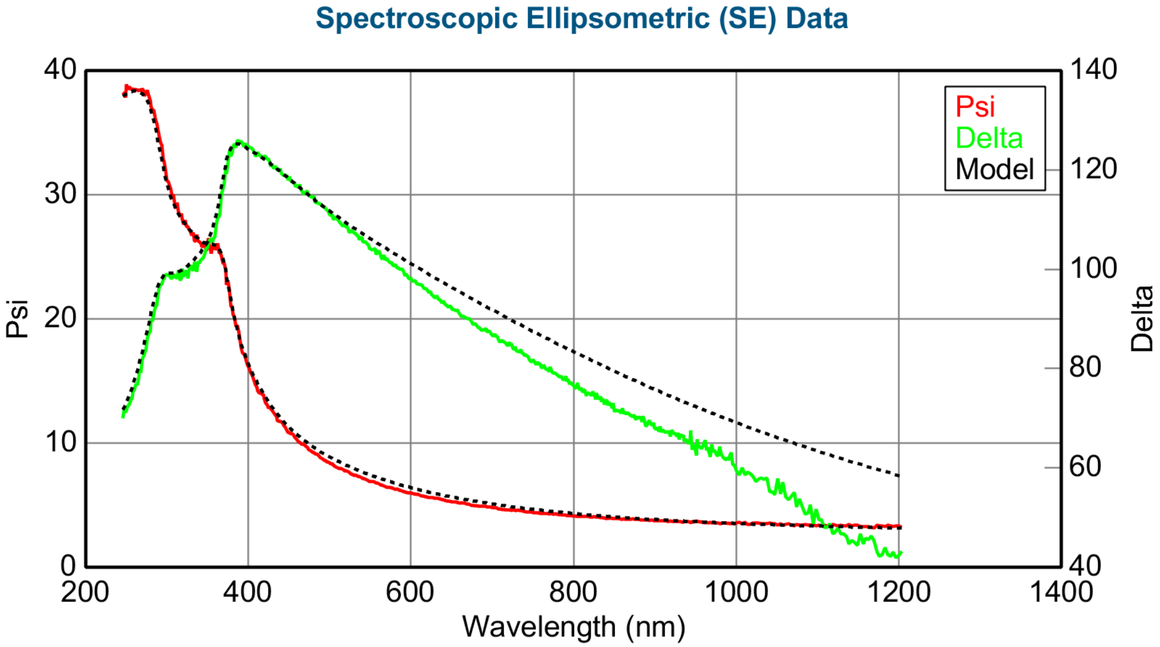

Figure 3.4 Ellipsometric fit for the 45K 1.5 wt% PMMA film.

The final molecular weight investigated for the PMMA study was 160K. This molecular weight was chosen as it was shown in Figure 3.3 that an increase of approximately 40K in molecular weight did not produce the film thickness expected. For these brushes, a range of temperatures was investigated. This was done as mentioned previously the molecular weight of a polymer influences its glass transition temperature [9]. In this study, the temperatures used were 150°C, 175°C, 200°C, and 230°C. This range was picked as it explicitly showed that the larger molecular weight required a higher temperature. Once again, the annealing times were varied from 0.5, 2 and 6 hours. Figure 3.5 shows the thickness values obtained for the range of solution concentrations over the different annealing temperatures and times.

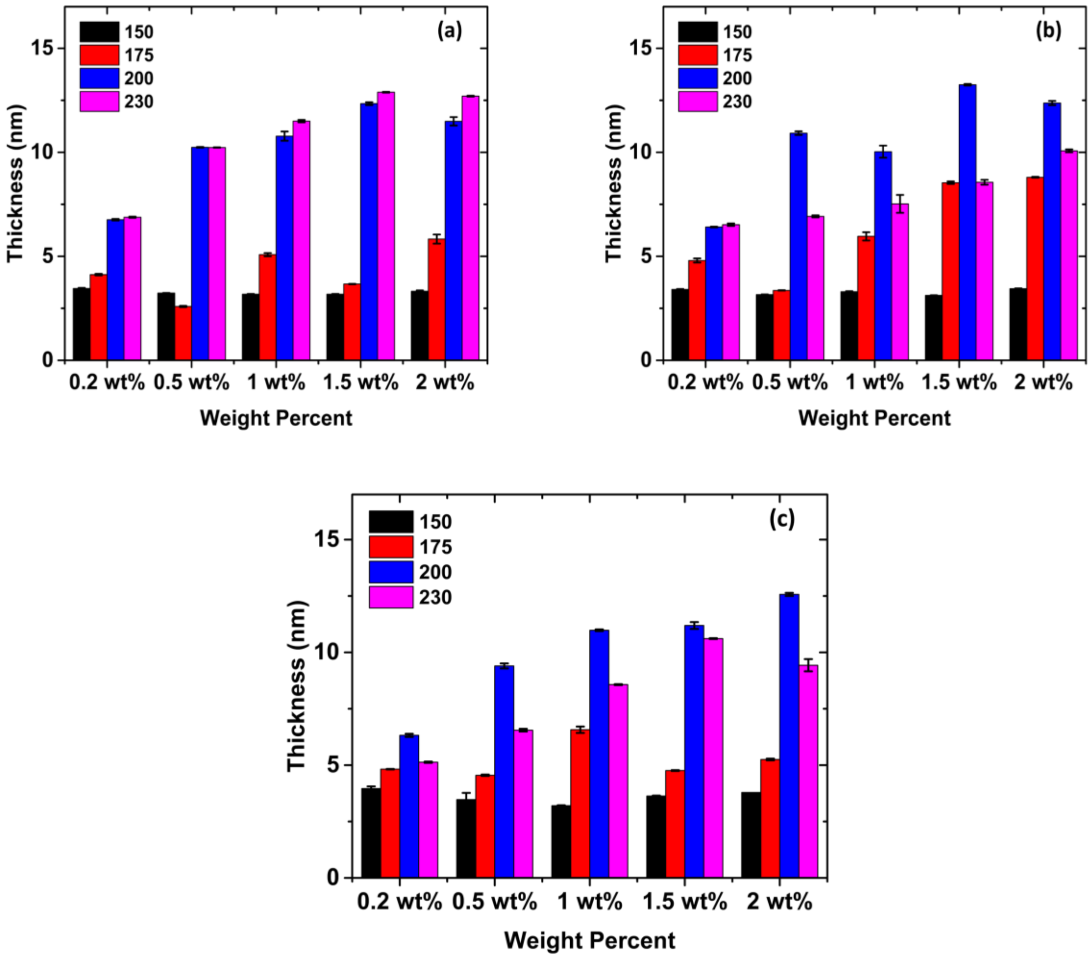

Figure 3.5 Ellipsometry results for the 160K PMMA samples, annealed at a range of temperatures for (a) 0.5 hr, (b) 2 hr, and (c) 6 hr. This data clearly shows that the increase in temperature lead to an overall increase in the thickness of the polymer brush.

The data illustrated in Figure 3.5 clearly shows that for all times the samples annealed at the lower temperatures are thinner than those annealed at the higher temperatures. This is because the lower temperatures do not allow for sufficient polymer grafting. Due to these low densities, the polymer chains do not extend enough yielding thinner films. When the annealing temperature reached 200°C there is a clear increase in the thickness of the polymer films for all annealing times. This can be also seen for the brushes annealed at 230°C, however samples annealed for 2 and 6 hours at this temperature show a drop in thickness compared to the 0.5 hour anneal. It was believed that this was occurring due to polymer film breakdown which was caused by the films being at such a high temperature for a long period of time. For optimisation purposes, it was decided that using the higher temperature of 230ºC was the most useful as it yielded the thickest film at the lowest anneal time of 0.5 hours.

When comparing the thickness of the films with respect to the solution concentration, for each temperature and anneal time, there was a clear increase in thickness with the increase in weight percent. The thickest film obtained, with an anneal temperature of 230ºC and annealed for 0.5 hours, was the 1.5 wt% solution with a thickness of approximately 13 nm. When comparing this to the lower molecular weight films, there was also a clear rise in the brush thickness for the 160K PMMA. This shows that for the case of PMMA the higher the molecular weight, as well as the higher the solution concentration, yielded an overall thicker polymer brush. An example of an ellipsometric fit for the 1.5 wt% film resulting in the thickest brush can be seen below in Figure 3.6. This illustrates the goodness of the fit.

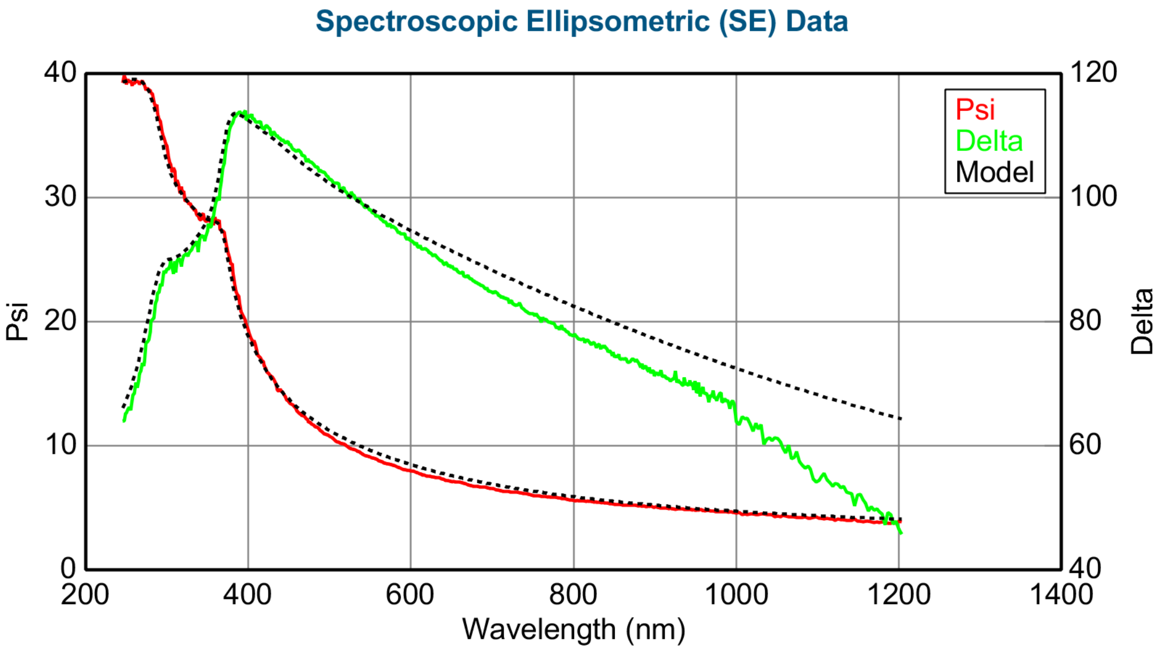

Figure 3.6 Ellipsometric fit for the 160K 1.5 wt% PMMA film.

3.3.1.2 GA-ATR-FTIR

Once ellipsometry was completed and the thickest films were identified, GA-ATR-FTIR was conducted on all samples to ensure that the PMMA was grafted to the surface of the substrate. This method also shows a relationship between peak intensity and film thickness which allowed further comparisons to be made with the ellipsometry results.

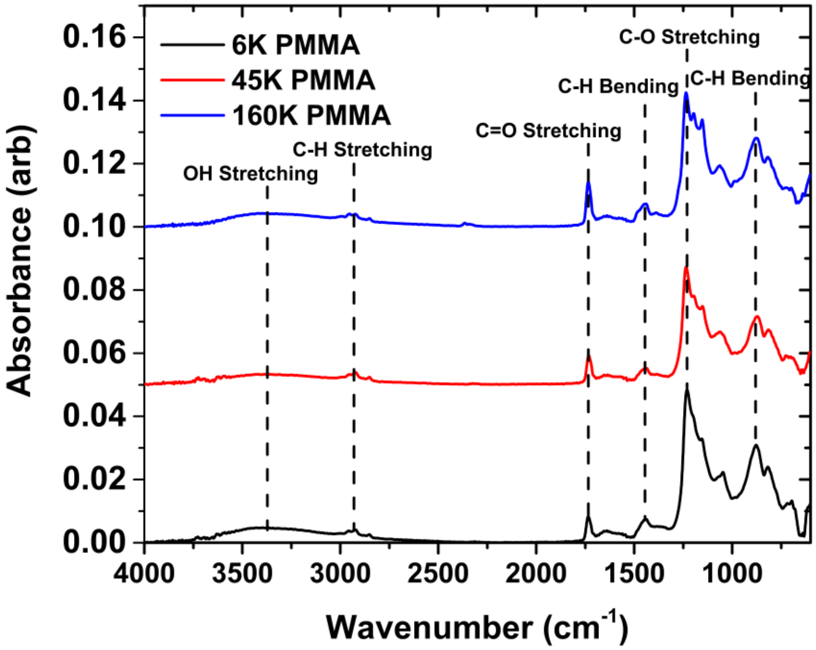

Figure 3.7 GA-ATR-FTIR spectra for the thickest brushes obtained for the 6K, 45K and 160K PMMA. These spectra show all associated bonds with the PMMA structure, with an increase in the intensity of these bonds with respect to the film thicknesses.

Figure 3.7 shows the GA-ATR-FTIR spectra for the thickest brushes obtained for all molecular weights. Note that each brush shown was fabricated with a 1.5 wt% solution but the annealing time and temperature varies depending on the molecular weight. Within the figure, all major bond vibrations associated with the PMMA structure, which can be seen in Figure 1.11, are labelled. Peaks seen at 292 cm^{-1} , 900 cm^{-1} and 1450 cm^{-1} correlate with the various bending and stretching modes of the C-H bonds. These are mainly present within the polymer backbone but they are seen within the side chains also. The peak at 1735 cm^{-1} shows the bond C=O which can be seen in all the molecular weight cases. This was the main band that indicated the presence of PMMA as it was the major unique feature of the polymer structure. When comparing the intensity of this peak across the molecular weights there was a slight increase in absorbance with the rise in brush thickness, with the 160K PMMA having the largest value. This was because there was a larger amount of C=O in the thicker polymer films which led to a higher absorbance value. This agreed with the ellipsometry results seen as the thickest brush layer fabricated was the 160K film. Finally, the band appearing at 1234 cm^{-1} shows the presence of C-O which was mainly seen within the polymer structure. But it also appears at the polymer silicon interface as it was the bond that was formed when the polymer chains grafted to the substrate surface [7,8].

From the GA-ATR-FTIR results and observed behaviour of the peak intensities, it was clear that PMMA was present on all substrate surfaces for all molecular weight cases, in agreement with ellipsometry results discussed in section 3.3.1.1.

3.3.1.3 AFM

AFM was then conducted to ensure that the polymer films formed were of good quality, i.e. continuous, and smooth and to insure that no islanding had occurred. The roughness of each film was also calculated to confirm that the films were smooth, which is important when using these brushes for the fabrication of good quality metal oxide films. Figure 3.8 shows the AFM images of the thickest films obtained for each of the molecular weights. From these images, it was clear that each of the films were extremely smooth and no distinct islanding had occurred. The RMS roughness of the 6K brush was 0.2 nm, the 45K brush was 0.3 nm and the 160K brush was 0.4 nm. These values for roughness were very low, which confirmed that the brushes were extremely smooth and were of good quality.

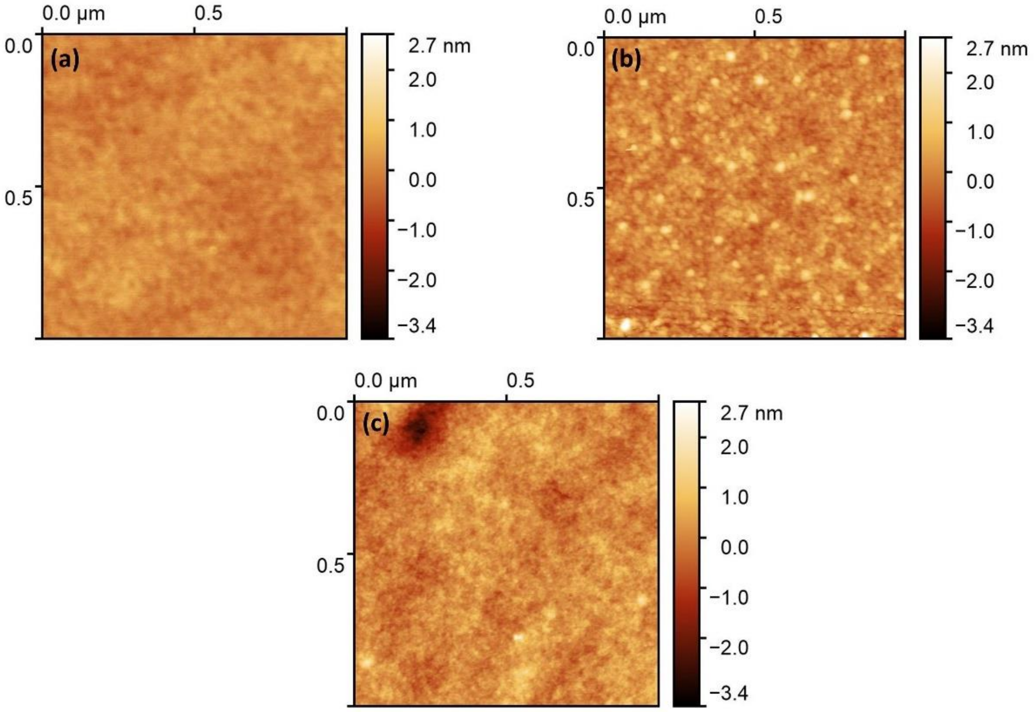

Figure 3.8 AFM images of (a) 1.5 wt% 6K PMMA, (b) 1.5 wt% 45K PMMA and (c) 1.5 wt% 160K PMMA. From these images it is clear that all PMMA brushes were extremely smooth and of good quality.

3.3.1.4 X-Ray Reflectivity

XRR was conducted on the thickest brushes obtained for the three different molecular weight PMMA samples. This was done to not only determine the density of the brush films but also to once again confirm the increase in brush thickness as well as showing that the films were smooth and of good quality. Figure 3.9 shows the XRR experimental data as well as the simulated fits for the 6K, 45K and 160K PMMA films once again made using a 1.5 wt% solution.

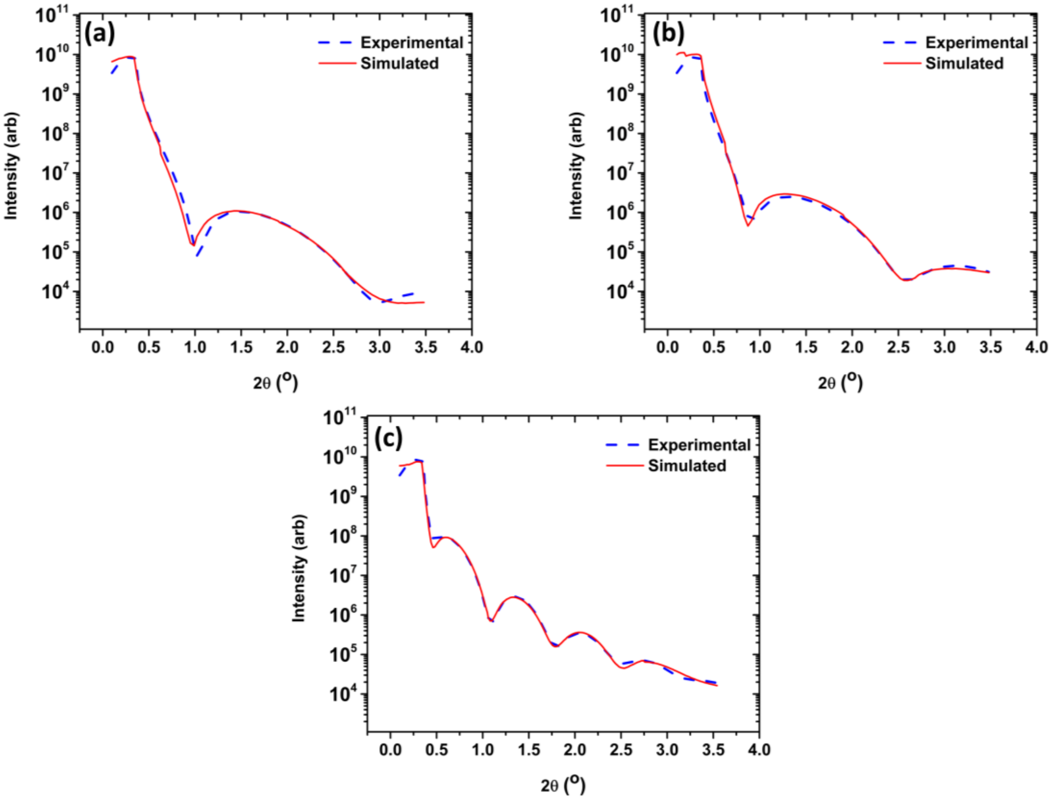

Figure 3.9 XRR results showing the experimental and simulated data for the (a) 6K, (b) 45K and (c) 160K PMMA 1.5 wt% samples. Through the increased number of oscillations, it can be determined that 160K PMMA was the thickest film observed agreeing with the previously recorded ellipsometry.

From Figure 3.9 the first point to note is that with an increase in the polymer molecular weight there is an increase in the number of oscillations within the spectra. This essentially represents an increase in the thickness of the sample, with more oscillations corresponding to an overall thicker film. The quantitative thickness values obtained through the fit can be seen below in Table 3.2.

Table 3.2 Quantitative results of the density, thickness, and roughness for the PMMA brush samples determined from the simulated fit.

Sample	***Density (g/cm^3)***	***Error (min/max)***	***Thickness (nm)***	***Error (min/max)***	***Roughness (nm)***	***Error (min/max)***
6K PMMA	1.28	-0.02, 0.3	3.50	-0.45, 0.36	0.63	-0.17, 0.21
45K PMMA	1.00	-0.02, 0.03	4.09	-0.25, 0.36	0.52	-0.38, 0.48
160K PMMA	0.98	-0.02, 0.02	9.97	-0.60, 0.47	0.81	-0.49, 0.43

While there is an increase in the brush thickness with respect to the molecular weight of the PMMA, the exact thickness values do not agree with the ones seen in section 3.3.1.1. Error analysis was conducted on the fit however the error does not cross over with the thickness values seen from the ellipsometry data. This discrepancy could be due to inconsistent heating in the anneal step across the samples when they were fabricated. It is also to note that the manufacturers of the software state that this error analysis is not a strictly valid statistical estimation as the systematic error when recording X-Ray data makes it very difficult for accurate error bar calculation [11]. This however was the best and most realistic fit achieved. Also seen in Table 3.2 the roughness of each sample is very low, this agrees with the AFM data seen in section 3.3.1.3 and confirms that each of the PMMA brushes are continuous and smooth for all molecular weight values.

Finally, Table 3.2 shows the density values for each molecular weight film. It can be seen that with an increase in the molecular weight there appears to be a decrease in the film density. This may be due to chain bending in the higher molecular weight films, where the polymer chains have not fully extended away from the silicon substrate, they bend over blocking potential grafting sites. This effect is not seen to the same extent in the 6K PMMA films as they overall chain length is shorter thus allowing for a higher grafting density. Despite this it is still clear that the higher molecular weight film still yields an overall thicker polymer brush.

3.3.2 Polystyrene Results

3.3.2.1 Ellipsometry

When studying the effect of molecular weight and solution concentration on the thickness of PS brushes an annealing temperature of 200°C was chosen. Unlike the study involving PMMA, there was no variation in annealing temperature, this was because from the literature it was noted that for the molecular weights being studied a temperature of 200°C was suitable [5].

Figure 3.10 shows the ellipsometry results for the brushes fabricated using the 16K and 42K PS at a range of solution concentrations. When looking at the films fabricated using the 16K PS, seen in Figure 3.10 (a), it was clear in the 0.5 hour case that there is an increase in thickness for increasing solution concentration. There was more variation in thickness for the 16K brushes annealed for 2 and 6 hours across the solution concentrations. This may have been due to inconsistent annealing temperatures across the surface of the hot plate. However, when comparing the films fabricated using the 1.5 wt% solution to the ones fabricated using the 0.2 wt% solution there was a distinct increase in the thickness with the higher solution concentration. These results confirmed that in the case of the 16K PS there was an increase in thickness with respect to the solution concentration.

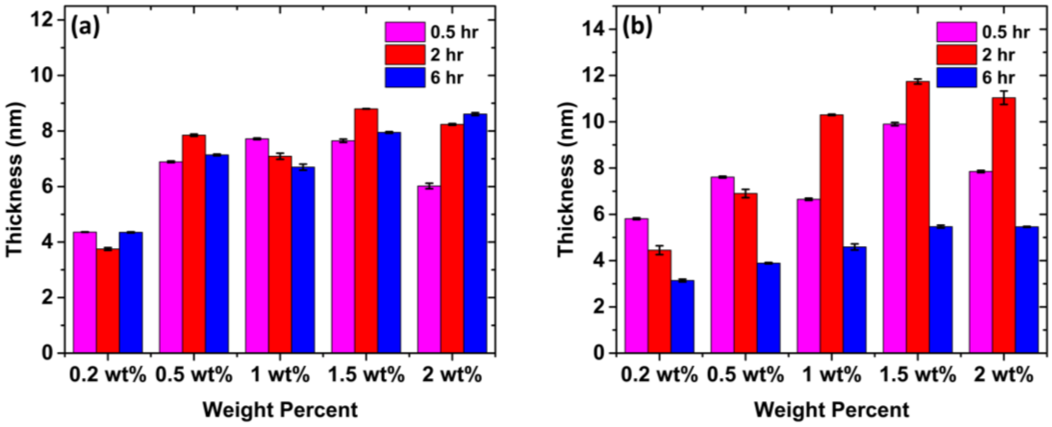

Figure 3.10 Ellipsometry results for (a) 16K and (b) 42K PS fabricated using a range of solution concentrations and annealed for 0.5hr, 2hr and 6hr. These graphs show that there is an increase in thickness with respect to solution concentration for both molecular weights.

For the samples fabricated using the 42K PS, shown in Figure 3.10 (b), there was an increase in thickness for increasing solution concentration, particularly for the samples annealed for 2 hours. The 0.5 hour case showed more variation in thickness across the solution concentrations but once again when comparing a high solution concentration, such as the 1.5 wt%, to a lower concentration, such as 0.2 wt%, there was a distinct increase in thickness. The samples annealed for 6 hours appeared to have a significant decrease in thickness. This may be because the samples were at too high a temperature for too long which caused the samples to breakdown. Once again it was clear that there was an increase in thickness with respect to an increase in solution concentration.

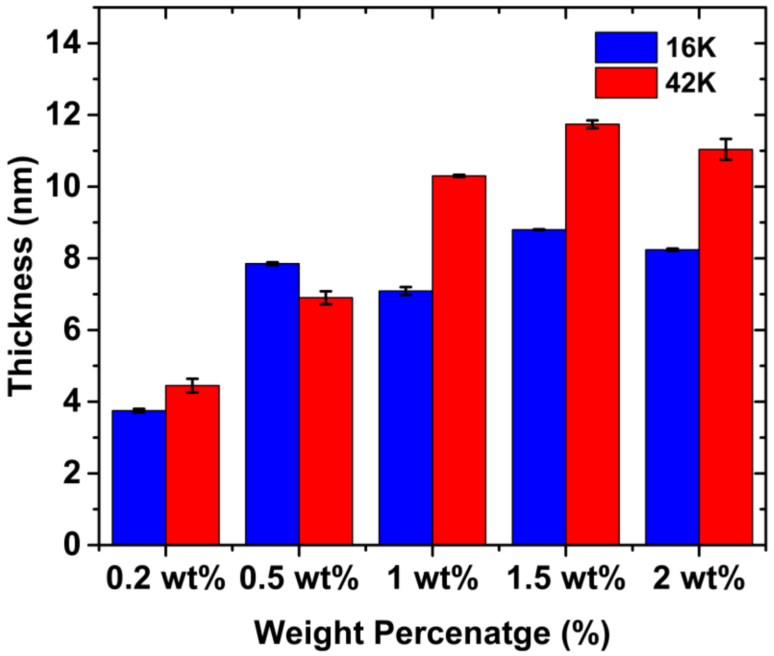

Figure 3.11 Direct comparison of ellipsometry results for the 16K and 42K PS at a range of solution concentrations. This data shows that with the increased molecular weight there was also an increase in thickness for most solution concentrations.

Figure 3.11 shows a direct comparison of the ellipsometry results for both molecular weights at the anneal times which resulted in the thickest films. As previously discussed, there was an increase in the brush thickness with respect to the solution concentration which can be seen in the figure above. It was also clear from Figure 3.11 that the higher molecular weight of 42K yielded a thicker polymer brush than the films made with 16K PS. This was expected as the longer chains of the higher molecular weight polymer led to a thicker film. Note that for the 16K PS there appears to be a thickness saturation of approximately 8 nm from 0.5 wt% on. This is compared to the thickness saturation of approximately 12 nm for the 42K films, reached at 1.5 wt%. This could be due to the shorter chain length of the 16K PS as the increase in the solution concentration made little difference to the thickness for the higher cases. From these results, it can be said that overall, an increase in solution concentration and molecular weight leads to a thicker polymer brush. Figure 3.12 shows an example of the ellipsometric fits obtained for the 42K 1.5 wt% PS brush. This illustrates the goodness and suitability of the fits obtained for this study.

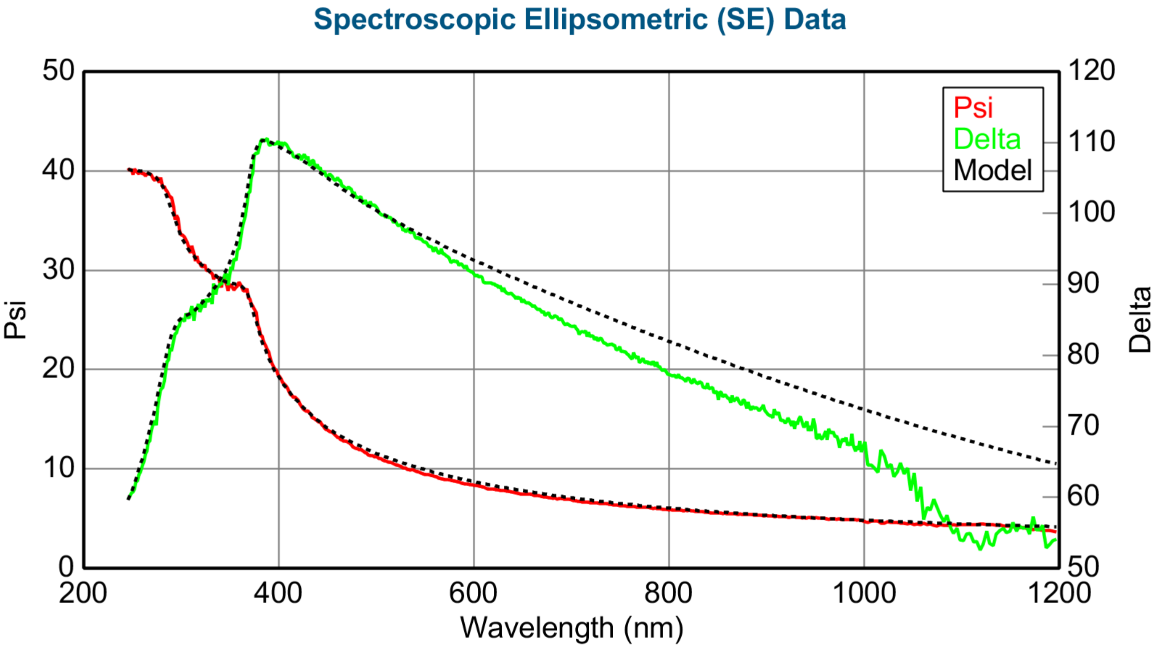

Figure 3.12 Ellipsometric fit for the 42K 1.5 wt% film. This shows an example of the fits conducted as well as illustrating the goodness of the fit.

3.3.2.2 GA-ATR-FTIR

Once the thickness of the PS brushes was confirmed GA-ATR-FTIR was conducted to confirm the presence of the polymer on the surface of the substrates. Figure 3.13 shows the GA-ATR-FTIR spectra for the thickest films obtained for each of the molecular weights. From these results, all peaks associated with the PS structure, seen in Figure 1.11, can be seen.

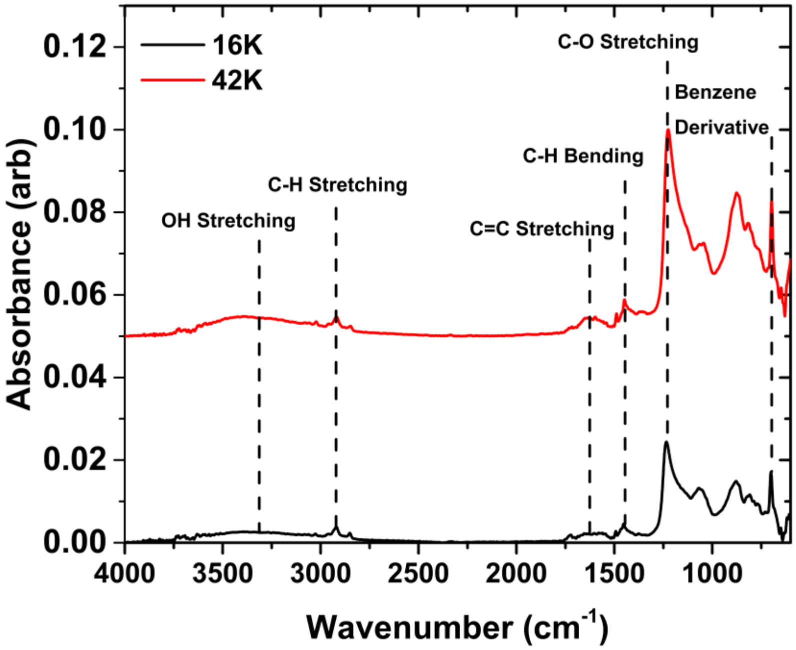

Figure 3.13 GA-ATR-FTIR results of the 1.5 wt% 16K and 1.5 wt% 42K PS as these were the thickest films obtained in each molecular weight cases with all peaks present in both spectra being attributed to the PS structure.

Similar to the spectra shown in Figure 3.7 the peaks at 292 cm^{-1}, 900 cm^{-1} 1450 cm^{-1} represent the various bending and stretching modes of C-H bonds. These are mainly observed in the polymer backbone but they are also present in the benzene ring side chain. The peak at 1600 cm^{-1} was associated with the cyclic alkene C=C stretching modes. This is solely linked with the benzene ring and was one of the main identifiers of the PS thin films. Alongside this, the band at 700 cm^{-1} was due to the benzene ring derivative. Both peaks confirmed the presence of the PS on the surface of the silicon, as the benzene ring was the main unique structure of the PS polymer. The final peak seen in Figure 3.13 was the band appearing at 1234 cm^{-1} which showed the presence of C-O. This correlated to the bonds grafting the polymer to the silicon which were created in the condensation reaction forming the polymer brush [7,8].

As previously mentioned, there was a correlation between the intensity of the peaks seen in Figure 3.13 and the thickness of the polymer brush. This is due to the larger amount of bonds present within the thicker polymers leading to higher peak intensity. It was clear from Figure 3.13 that the peak intensity seen for the 42K PS brush was greater than that of the 16K brush. This agreed with the ellipsometry results seen in Figure 3.11 and further confirms that the brush fabricated with the larger molecular weight polymer yielded the thicker film.

3.3.2.3 AFM

Finally, AFM was used to ensure that the polymer brushes fabricated were of good quality. Once again, the roughness of each film was calculated. Figure 3.14 shows the AFM images obtained for the thickest brushes for both molecular weights. From each image, it was seen that the films were overall very smooth, and no islanding had occurred. The calculated RMS roughness for the 16K PS brush was 0.2 nm and the 42K PS brush was 0.3nm. These values were extremely low and confirmed that each film was smooth and of good quality.

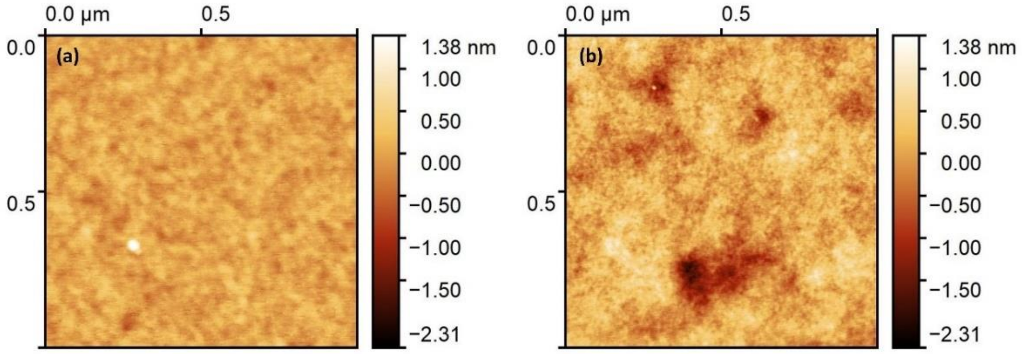

Figure 3.14 AFM images of the thickest films obtained for the (a) 16K and (b) 42K PS. These images show that the PS brushes were of good quality and smooth.

3.3.3 Effect of Oxygen Plasma Processes on Polystyrene Brushes

The beginning of this work focused on the effect that O_2 plasma processes of various lengths and powers had on PS brushes which was conducted using a Henniker Plasma HPT-200 benchtop plasma treater. When designing the plasma processes the main factor that was considered was ensuring maximum hydroxy functionalisation, as this is required for a second layer application, with minimal film breakdown. It was determined that a 200 W and a 150 W plasma process with various durations would be investigated as these would provide the gentle treatment required.

Once treated, contact angle measurements were performed to determine whether functionalisation had occurred. These measurements were taken at several stages after processing, which was done to track the decomposition of the functionalisation as this was not a permanent process. Figure 3.15 shows the contact angle results for each of the powers used and the various treatment times.

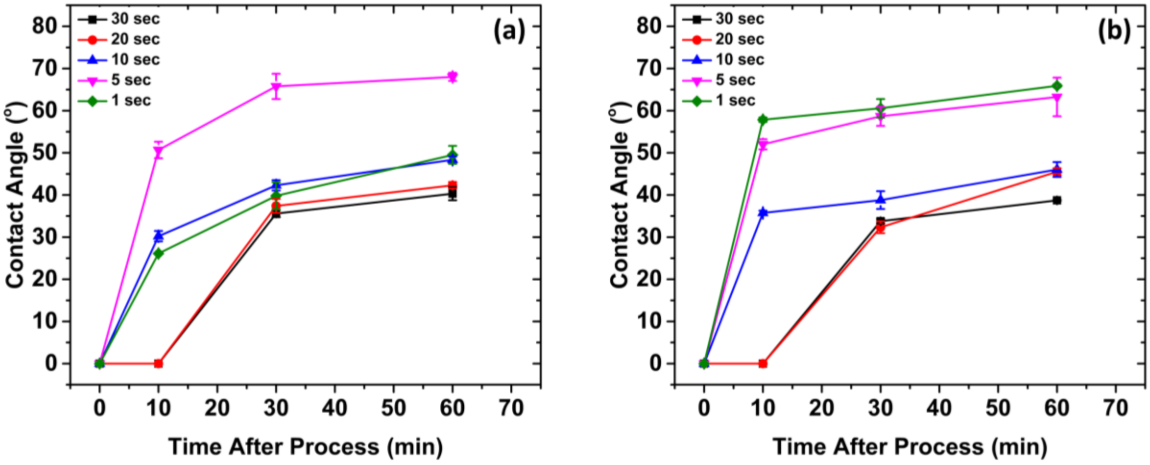

Figure 3.15 Contact angle results of the treated 42K PS films, obtained over a range of times post-processing, for the various durations of the (a) 200 W and the (b) 150 W processes. For all process times it can be seen that functionalisation was achieved for both process powers.

From the contact angle results seen in Figure 3.15 above, it was shown that for both power settings, across all process lengths, there was functionalisation seen immediately after the treatment. This was because the contact angle for each of the processes was approximately 0°, which indicates successful hydroxy functionalisation of the PS surface [12]. This was a promising result as it meant second layer application was possible. The decay of the treatment can also be seen from these results. It was clear that the longer treatment times of 30 and 20 seconds yields a longer functionalisation period as the contact angle remains at 0° after 10 minutes post processing. When comparing this to the shorter treatment times of 1, 5 and 10 seconds there was a faster increase in the contact angle data indicating a faster decay in the functionalisation. However, when comparing these results to the contact angle of untreated PS, which is approximately 90° [5], there was a decrease in all cases. This indicated that while there was a decay in the functionalisation, complete decay was not seen within the first hour after treatment. From this data, it was determined that for optimal results the second layer application would have to be done straight after plasma processing.

Once the contact angle measurements were taken and functionalisation was confirmed ellipsometry was used to measure the degree of polymer breakdown caused by the oxygen treatments. Figure 3.16 shows the ellipsometry results for all films after the O_2 plasma treatments. It can be seen that for both plasma power levels the longer process times of 30 and 20 seconds lead to almost complete polymer removal. This made these longer processes unsuitable for the purpose of this work. As the process times decreased there was also a decrease in the film breakdown as the film thickness before processing was approximately 12 nm. This meant that these shorter processes would be more suitable for the second layer application as they successfully functionalised the surface with minimal film breakdown.

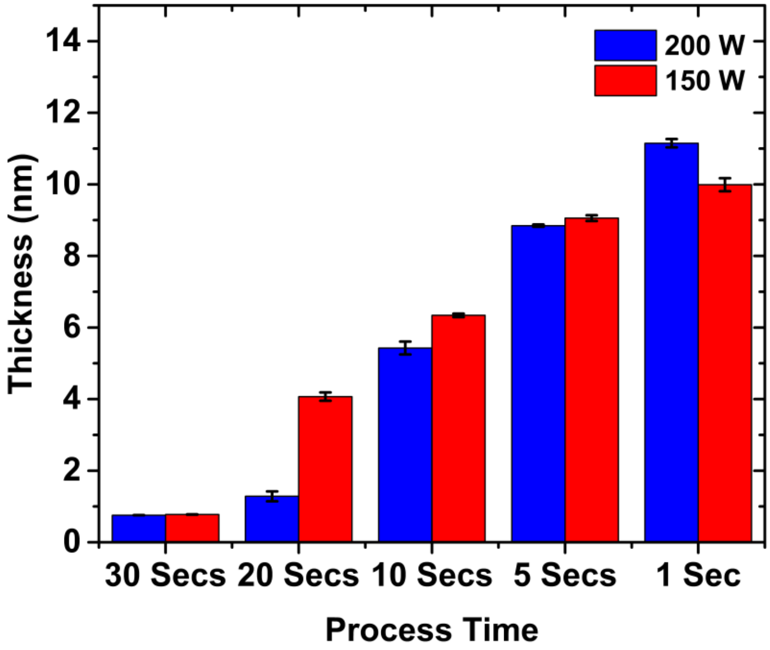

Figure 3.16 Ellipsometry results of the 42K PS films post plasma treatment for the various process times at the powers of 200 W and 150 W. This data shows that almost complete polymer removal occurred for the longer process times, whereas there was only approximately 1 nm removed for the shorter treatment periods.

Once the optimal plasma process conditions were determined, AFM was used to determine the quality of the films after treatment, as well as to calculate their roughness. Figure 3.17 shows the AFM images for both powers at the lower processing times. Initially looking at these images there was no clear indication of a decrease in the film quality. However, the appearance of small objects on the surface of the films was noticed. These were identified as AFM tip artefacts and have no relation to the film quality. The roughness of each film was also very low. They were as follows; the 200 W treatment for 5 seconds had a roughness of 0.8 nm, the 200 W treatment for 1 second had a roughness of 0.3 nm, the 150 W treatment for 5 seconds had a roughness of 0.9 nm and finally the 150 W treatment for 1 second had a roughness of 0.6 nm. These values were all extremely low and indicated that the processes caused very little damage to the film's surface, meaning that the second layer application would be applied to a good quality film.

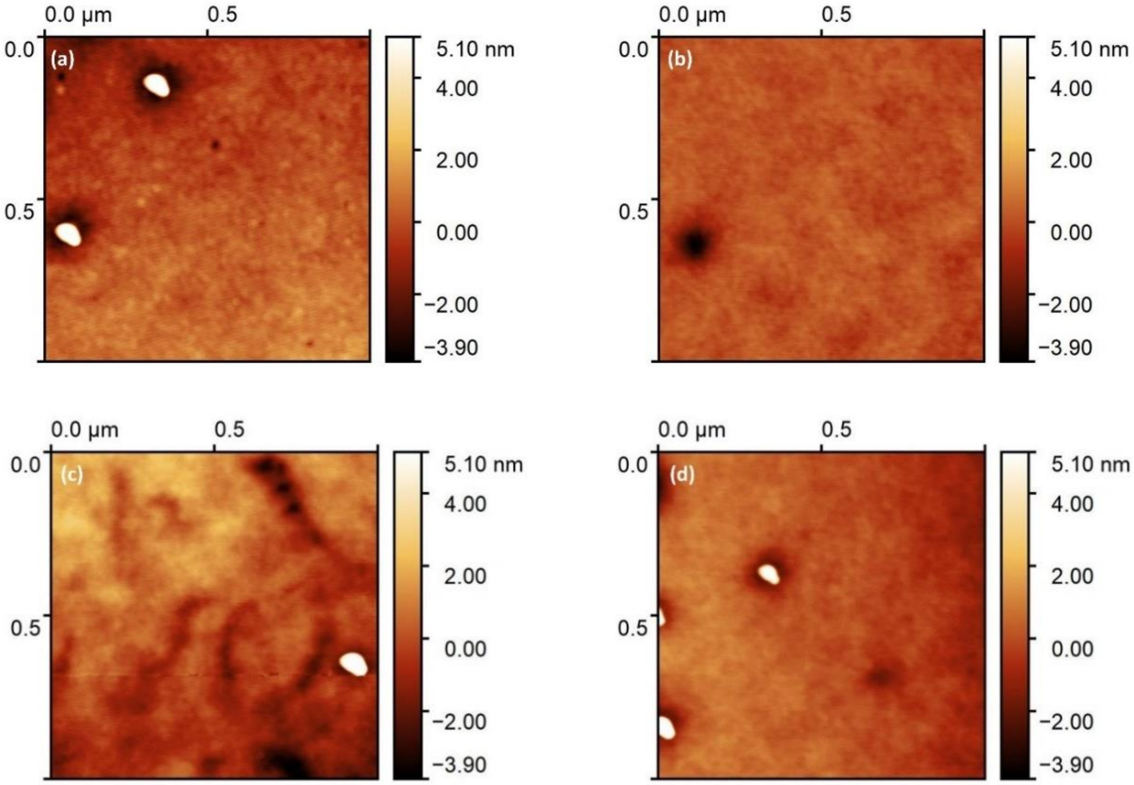

Figure 3.17 AFM images of 42K PS prior to the plasma processes (a) 200 W for 5 seconds, (b) 200 W for 1 second, (c) 150 W for 5 seconds and (d) 150 W for 1 second. These images show no damaged caused by the plasma treatment used for the functionalisation of these polymer films.

Finally, GA-ATR-FTIR was used to confirm that the treatments were not causing any permanent chemical changes within the PS films. Figure 3.18 shows the GA-ATR-FTIR results for all films processed at the shorter time intervals. From these results, all major peaks associated with the PS structure are there in all cases. These include the peaks at 292 cm^{-1}, 900 cm^{-1}, and 1450 cm^{-1} which correlate with the bending and stretching modes of the C-H bond. These bonds are mainly seen within the polymer’s backbone. The peak at 1600 cm^{-1} was associated with the cyclic alkene C=C stretching modes which were present within the benzene ring, side chain, this peak shows that PS is present on the surface of the substrate for all cases. The band appearing at 700 cm^{-1} was due to the benzene ring derivative once again confirming the presence of PS for all the films measured. Finally, the final peak seen is the band appearing at 1234 cm^{-1} which shows the presence of C-O. As there are no other distinct peaks present it was clear that there was no permanent chemical change to the films. This meant that when a second layer was applied the film as a whole would remain pure PS.

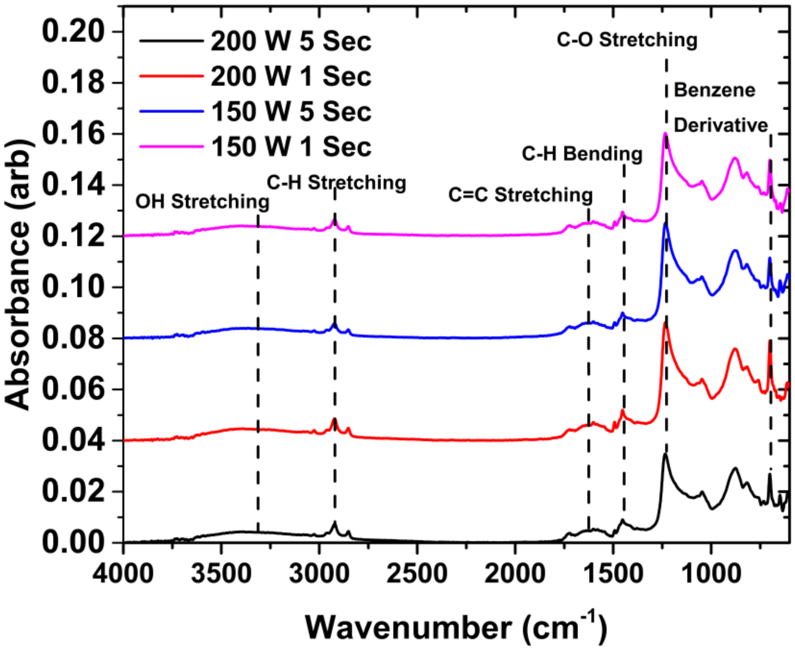

Figure 3.18 GA-ATR-FTIR results for the 42K PS films post plasma treatment for the shorter process times at powers of 200 W and 150 W. These spectra show that no permanent chemical changes were caused by the plasma process.

3.3.3.1 Second Layer Application

Once the optimised plasma processes were determined a second layer of PS solution was applied. The same 1.5 wt% 42K PS solution that was used for the initial brush fabrication was used for the second application. The anneal time and temperature for these second layers were varied; this was to ensure optimal grafting. The temperatures and times used were listed in section 3.2.3. Figure 3.19 shows the ellipsometry results for the films after the second application.

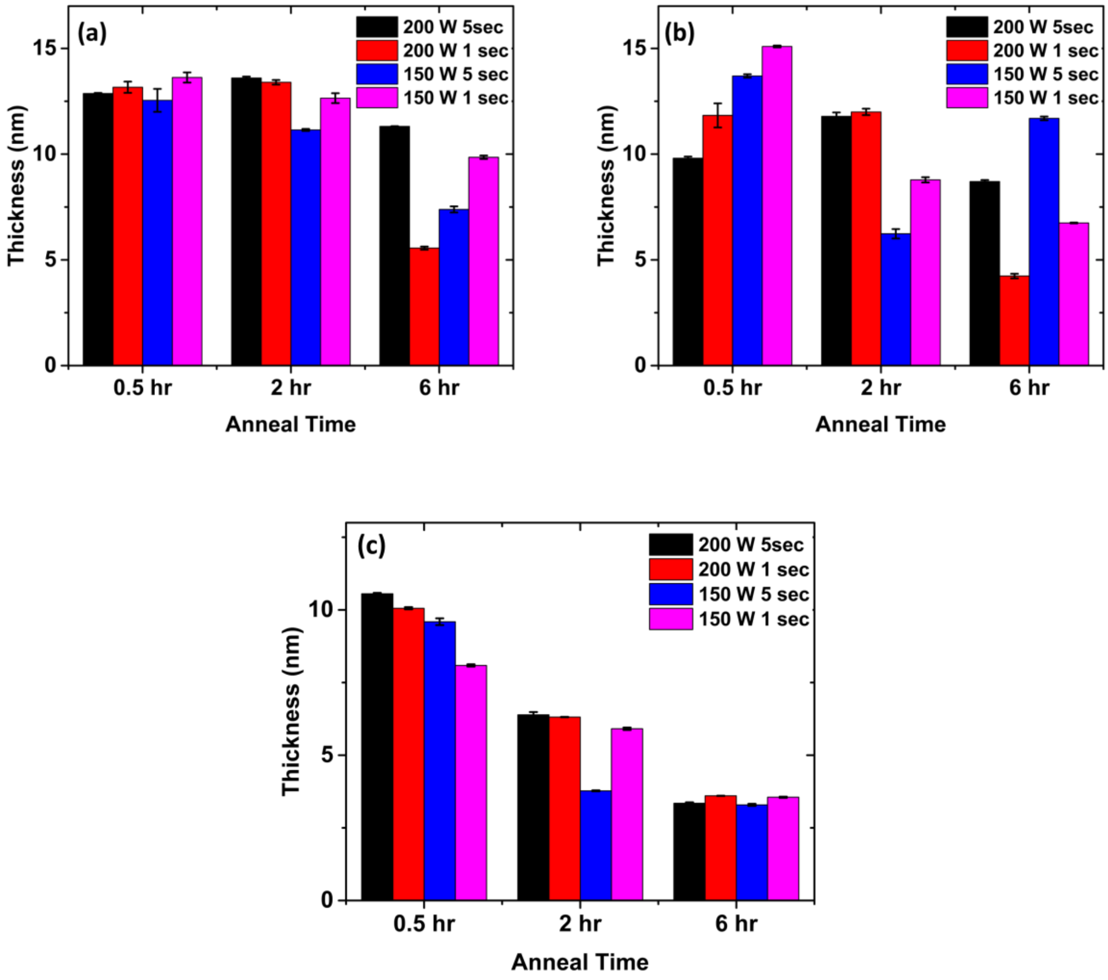

Figure 3.19 Ellipsometry results of the 42K PS films after a second layer application of the original 42K PS fabricating solution, annealed at (a) 200°C, (b) 230°C and (c) 250°C for 0.5hr, 2hr and 6hr. This data shows no significant increase in the PS brush thickness post second layer application.

Comparing these results to those in Figure 3.16 it is clear that there is no significant increase in the thickness of the films because before the second layer was applied they had a thickness of approximately 10 nm and after the second layer application, the maximum thickness seen across the three temperatures was 15 nm. This means that while there was a small amount of additional growth there was not as much as would be expected. It would have been thought that with the second layer application being the same process as the first the thickness of the brush should have doubled. This lack of growth could be due to insufficient grafting or film breakdown caused by the second solution application. As the thickness increase was so small this method of polymer brush fabrication was deemed unsuccessful as it would be very time consuming to reach the desired thicknesses.

3.4 Conclusions

The controllability of brush thickness for the polymers PMMA and PS through the variation of molecular weight and solution concentration has been presented. Firstly, the relationship between the solution concentration and thickness was illustrated for each molecular weight. Using ellipsometry it was shown for both polymers that an increase in weight percentage caused an increase in thickness for all molecular weight cases. The optimal weight percentage for both polymers and for all molecular weights was shown to be 1.5 wt%. Secondly, the relationship between thickness and molecular weight was shown. For both polymers, it was seen that an increase in molecular weight also led to an increase in overall brush thickness, with the 160K PMMA and 42K PS yielding the thickest films. It was also seen when directly comparing the thickest films fabricated for the two polymers that a much higher molecular weight was needed for the PMMA than the PS to yield a similar film thickness. This was due to the physical properties of each polymer because PMMA is known to be more flexible than PS meaning thicker films are more difficult to make [10]. XRR was used in the case of the PMMA films to determine the density of these brushes. It was shown that with an increase in molecular weight there was a decrease in the grafting density. This was due to chain bending in the higher molecular weight films reducing the number of grafting sites on the silicon substrate thus reducing the grafting density. Finally, GA-ATR-FTIR was used to confirm the presence of each polymer on the surface of the silicon. AFM was also conducted which showed that all films were of good quality and smooth.

Following on from this the stepwise growth of PS films using an oxygen plasma process was investigated. The powers 200 W and 150 W were used at a range of processing times between 1 and 30 seconds. It was shown via contact angle and ellipsometry measurements that the use of an oxygen plasma for a short time could successfully functionalise the surface of the PS brush with minimal breakdown of the film itself. AFM showed that the roughness of the films post plasma treatment did not go up and the films remained of good quality. Finally, GA-ATR-FTIR was conducted to show that the plasma treatment did not change the film permanently and that it remained pure PS. Once it was determined that both plasma powers at the low process times yielded successful functionalisation and minimal damage the second layer of the polymer solution was applied. Using ellipsometry it was determined that the second layer application was unsuccessful and that there was no significant increase in polymer layer thickness. It was therefore concluded that this was not a viable method for increasing brush thickness.

3.5 References

(1) Azzaroni, O.; Szleifer, I. *Polymer and Biopolymer Brushes: For Materials Science and Biotechnology*; 2017. https://doi.org/10.1002/9781119455042.

(2) Taylor, G. N.; Wolf, T. M. Oxygen Plasma Removal of Thin Polymer Films. *Polym. Eng. Sci.* **1980**, *20* (16), 1087–1092. https://doi.org/10.1002/PEN.760201610.

(3) Vesel, A.; Primc, G.; Zaplotnik, R.; Mozetič, M. Applications of Highly Non-Equilibrium Low-Pressure Oxygen Plasma for Treatment of Polymers and Polymer Composites on an Industrial Scale. *Plasma Phys. Control. Fusion* **2020**, *62* (2), 024008. https://doi.org/10.1088/1361-6587/AB5B50.

(4) Vesel, A.; Semeni~, T. Etching Rates of Different Polymers in Oxygen Plasma. *Mater. Technolgies* **2012**, *46*, 227–231.

(5) Lundy, R.; Yadav, P.; Selkirk, A.; Mullen, E.; Ghoshal, T.; Cummins, C.; Morris, M. A. Optimizing Polymer Brush Coverage To Develop Highly Coherent Sub-5 Nm Oxide Films by Ion Inclusion. *Chem. Mater.* **2019**, *31* (22), 9338–9345. https://doi.org/10.1021/acs.chemmater.9b02856.

(6) Melting and decomp. temp’s https://pslc.ws/fire/howwhy/thermalp.htm (accessed Jul 26, 2021).

(7) Infrared Spectroscopy Absorption Table - Chemistry LibreTexts https://chem.libretexts.org/Ancillary_Materials/Reference/Reference_Tables/Spectroscopic_Parameters/Infrared_Spectroscopy_Absorption_Table (accessed Jul 23, 2021).

(8) IR Spectrum Table https://www.sigmaaldrich.com/IE/en/technical-documents/technical-article/analytical-chemistry/photometry-and-reflectometry/ir-spectrum-table (accessed Jul 23, 2021).

(9) Balani, K.; Verma, V.; Agarwal, A.; Narayan, R. Physical, Thermal, and Mechanical Properties of Polymers. *Biosurfaces* **2015**, 329–344. https://doi.org/10.1002/9781118950623.APP1.

(10) Ali, U.; Karim, K. J. B. A.; Buang, N. A. A Review of the Properties and Applications of Poly (Methyl Methacrylate) (PMMA). *Polym. Rev.* **2015**, *55* (4), 678–705. https://doi.org/10.1080/15583724.2015.1031377.

(11) Fitting of x-ray reflectivity data — GenX 3.6.21 documentation https://aglavic.github.io/genx/doc/tutorials/xrr_fitting.html (accessed Jun 11, 2023).

(12) Huang, F.; Wei, Q.; Wang, X.; Xu, W. Dynamic Contact Angles and Morphology of PP Fibres Treated with Plasma. *Polym. Test.* **2006**, *25* (1), 22–27. https://doi.org/10.1016/J.POLYMERTESTING.2005.09.017.

4 Investigation into the Effect of Polymer Brush Thickness on their Blocking or Infiltrating Properties

4.1 Introduction

The focus of the work presented in this chapter is on the effect that brush thickness has on the ability of both PS and PMMA to inhibit and accept infiltration respectively. As previously discussed in chapter 3 understanding how the parameters such as molecular weight and brush thickness effects a polymers properties, such as infiltration, is vital for a further understanding on how they would act in a BCP system. The first section of this chapter demonstrates the fabrication of Al_2O_3 films through the infiltration of PMMA brushes using an ALD base VPI process. The use of ALD for the infiltration of polymer brushes as well as the fabrication of patterned substrates through ASD has been previously reported [1–4]. It is well known that these types of oxide films can be fabricated through a wide variety of deposition techniques such as ALD [5–7] which do not require the additional step of PMMA film fabrication and infiltration. However, the importance of this work is in looking at how the parameters of thickness and molecular weight effects the infiltration process and therefore the resultant oxide. This information is required for BCP lithography as if these parameters were altered within a BCP system a better estimation on the quality of the resulting pattern could be made. Similarly in the case of the PS the way in which thickness effects its blocking capabilities is investigated, and as in the case of the PMMA this knowledge is vital for further BCP research as well as looking at how these films compare to conventional ASD deactivation films such as SAMs.

PMMA is widely known in the field of BCP lithography for its ability to be infiltrated [8]. This work aims to investigate whether a thicker PMMA brush has a larger uptake of infiltrating precursor and thus the capacity to fabricate a thicker resultant oxide film. In this study, three PMMA brushes of increasing thickness were exposed to a VPI process using TMA as the infiltrating precursor. The variation in thickness of the PMMA brushes was achieved through the increase in the molecular weight of the polymer. It is for this reason that the temperature at which the VPI process was carried out was studied. HAXPES measurements were used to evaluate the infiltration mechanisms of the PMMA, as well as looking at the Al uptake within the films post infiltration. From initial data it was observed that there was negligible increase in the amount of Al uptake with the increase in PMMA thickness. Following on from this study a comparison was made between the well-known polymer removal and metal oxidation processes of UV ozone and an ICP O_2 plasma [9–11]. Through the use of HAXPES it was determined that there was very little difference in the removal processes, with the O_2 plasma deemed a more suitable option as it is faster and more efficient. Finally, the thickness of the resultant oxide was measured using ellipsometry. These results showed that there was an increase in the oxide thickness with polymer thickness, demonstrating the effect that PMMA thickness has on its Al uptake.

On the other hand, PS is a polymer well-known for its ability to block the deposition of materials [12,13]. Similarly, in the case of the PS study three brushes of varying thickness were subjected to a conventional HfO_2 ALD process over a range of cycles. This work looks at how increasing the brush layer's thickness improves the number of cycles that can be effectively blocked. Through the use of in-situ XPS, it was shown that with an increase in the film's thickness there was a significant gain in the PS brush layer's ability to block HfO_2 deposition. This offers the possibility that PS could be used as a standalone material for area-deactivation in area-selective ALD processes, in the same way that SAMs are often used.

4.2 Experimental Details

4.2.1 Materials

Blanket silicon with native oxide was provided by our industrial collaborators (Intel). The polymers, hydroxy-terminated polystyrene (PS-OH) (of two molecular weights, specifically Mw = 16 kg mol^{-1} (16K) , PDI = 1.09 and Mw = 42 kg mol^{-1} (42K), PDI = 1.06) and hydroxy-terminated poly(methyl methacrylate) (PMMA-OH) (of three molecular weights, specifically Mw = 6 kg mol^{-1} (6K), PDI = 1.25; Mw = 45 kg mol^{-1} (45K) , PDI = 1.15 and Mw = 160 kg mol^{-1} (160K) , PDI = 1.15) were purchased from Polymer Source Inc. Canada and used as received. Toluene (anhydrous, 99.8%) and isopropyl alcohol (≥ 99.7%, FCC, FG) were purchased from Sigma Aldrich and used as received. Deionized water (resistivity = 18.2 MΩ cm) was also used.

4.2.2 Polymer Brush Fabrication

PS and PMMA brushes were fabricated using the grafting to method as outlined in Chapter 3. PS brushes were fabricated using a 0.2 wt% 42K, 0.2 wt% 16K and a 1.5 wt% 42K solution as this provided a range of suitable thicknesses for comparison. These samples were annealed at 200°C for 2 hours. PMMA brushes were fabricated using a 1.5 wt% 6K, 1.5wt% 45K and a 1.5 wt% 160K. The 1.5 wt% 6K samples were annealed at 200°C for a total of 2 hours while the 1.5 wt% 45K and 1.5 wt% 160K samples were annealed at 230°C for 30 minutes.

4.2.3 In-situ ALD and XPS characterisation of PS brushes

ALD processing and in-situ XPS analysis was conducted in a custom design Oxford Instruments Flexal ALD (base pressure 5 x 10-^{7} mbar) and a Scienta Omicron XPS (monochromatic Al Kα X-ray source, base pressure 5 x 10^{-9} mbar) with a 128 channel Argus CU detector. These systems were coupled using a fast-transfer robotic handler which was kept under vacuum with transfer taking approximately 1 minute. This setup allowed for XPS analysis to be conducted on processed samples in-situ without risk of atmospheric contamination.

PS samples were placed on a 100 mm steel carrier-wafer for ALD and XPS loading and transfer. This wafer allowed for sufficient heat transfer during the ALD process. Prior to this, all PS brush were exposed to a N_2 gas flow which removed any dust and surface impurities from the sample. Once loaded into the ALD system the samples were left to heat up to the processing temperature of 250°C for 20 minutes with the chamber under flow of 200 standard cubic centimetres per minute (sccm) of Ar gas to ensure good thermal conductivity. The PS samples were then exposed to a standard thermal ALD process using a hafnium chloride ($HfCl_4$) precursor with water as the co-reactant. The temperature of 250°C was chosen as it was a suitable deposition temperature for the chosen precursor outlined by the manufacturer of the FlexAl system. Using this temperature ensured the prevention of unwanted precursor decomposition or condensation. This temperature was also below the breakdown temperature of the PS brushes which is approximately 300°C and 400 °C [14]. The ALD process began by admitting the $HfCl_4$ precursor for a total of a 2 second dose time this was done using an Ar carrier gas at 200 sccm. Following on from this a 7 second purge, using Ar gas, was conducted to remove any unreacted precursor from the chamber. As this was a conventional thermal ALD process this was then followed by a 2 second water dose which allowed for the full reaction process to occur. The ALD cycle was then completed with a 15 second purge again done with Ar gas to remove any unreacted particles. This was repeated for the desired number of cycles during which the samples were removed in vacuum for XPS analysis. This allowed for the deposition to be monitored throughout the ALD process. All XPS data analysis was conducted using the CasaXPS software.

4.2.4 VPI and HAXPES Analysis of PMMA Brushes

VPI processing was conducted in the same Oxford Instruments FlexAl ALD system as described in section 4.2.3. Samples were exposed to a N_2 gas flow which removed any dust and surface impurities from the sample. Samples were then placed on a 100 mm steel carrier wafer for loading into the ALD system. In this experiment two deposition temperatures of 100ºC and 200ºC were used, both of which are below the degradation temperature of the polymer of 300ºC [15]. It is noted that unlike a conventional ALD process used in the PS study, this VPI process does not include a co-reactant. At the beginning of this process TMA was admitted to the chamber for a dose time of 0.1 seconds. Ar (200 sccm) was once again used as the carrier gas. Following this the chamber was then isolated from pumping, known as the hold step, which was achieved by the automatic closing of the valve used to regulate the pressure within the ALD chamber. This hold was done for 1 minute. It is to be noted that when the valve is in the closed position it does not provide a perfect vacuum seal between the chamber and the pumps therefore there is a gradual pressure decrease in the chamber during this hold step. This was then followed by an Ar (200 sccm) purge for 20 seconds. This process was repeated for a total of 1200 cycles to ensure sufficient polymer infiltration.

HAXPES analysis was performed at the National Synchrotron Light Source II in Brookhaven National Laboratory using the SST-2 beamline [16]. Spectra were acquired with a photon beam energy of 2 keV. A Si(111) crystal monochromator was used.

4.2.5 UV Ozone and O_2 Plasma Polymer Removal.

UV ozone and O_2 plasma treatments were used for the removal of the PMMA brushes as well as to convert the infiltrated TMA into Al_2O_3. O_2 plasma treatments were conducted using an ICP source within the ALD chamber. Samples were heated to 200°C with the chamber constantly being flushed with a 200 sccm flow of Ar. Once heated the samples were exposed to a 40 minute 300 W O_2 plasma. The flow of the O_2 was 100 sccm, and the pressure during the plasma process was 40 mTorr. This is the same plasma process used for the removal of the PS brushes in the HfO_2 study.

The UV ozone process was carried out in a Novascan PSD Pro Series Digital UV Ozone System coupled with an OES – 1000D Ozone Elimination System. Samples were placed into the system and heated to 200 °C and processed in the UV Ozone system for 12 hours to ensure sufficient polymer removal.

4.1.1 Additional Characterisation Techniques

Ellipsometry data was recorded using a J.A. Woolam XLS-100 ellipsometer. All data analysis was performed with the CompleteEASE software using a multi-layer model. This type of modelling was used to not only take into account the polymer films and the resultant oxides but also the silicon substrate as well as the silicon oxide intermediate layer. Within this model three layers were inputted, the silicon substrate, a 2 nm silicon oxide layer and finally either the respective polymer layer or the resultant aluminium oxide layer. The optical constants for each layer were obtained from the CompleteEase software from pre-determined models as the films in this study are well known and analysed. In all cases, three measurements were taken from different points on the sample and an average of these was calculated. The standard error of this was also determined.

4.2.6 Acknowledgements

The author would like to thank Mr Kyle Shiel and Dr Matthew Snelgrove for their assistance in sample processing and data collection. The author would also like thank Dr Conan Weiland of Brookhaven National Laboratory for his assistance in the HAXPES data acquisition.

4.3 Results

4.3.1 Infiltration of PMMA of various Molecular Weights and Thicknesses

The way in which the thickness, and hence molecular weight, of the polymer PMMA effects its ability to infiltrated by Al using a VPI process is presented. From Chapter 3 it was clearly shown that an increase in PMMAs molecular weight and solution concentration resulted in an increase in the brush thickness. For this work a 1.5 wt% solution of 6K, 45K and 160K PMMA was used for the fabrication of the brushes as this was shown to yield the thickest film in each molecular weight case. This allowed for a suitable thickness variation across the three samples for the investigation. Figure 4.1 shows the ellipsometry results for the PMMA brushes used, where a clear increase in thickness with respect to the molecular weight can be seen.

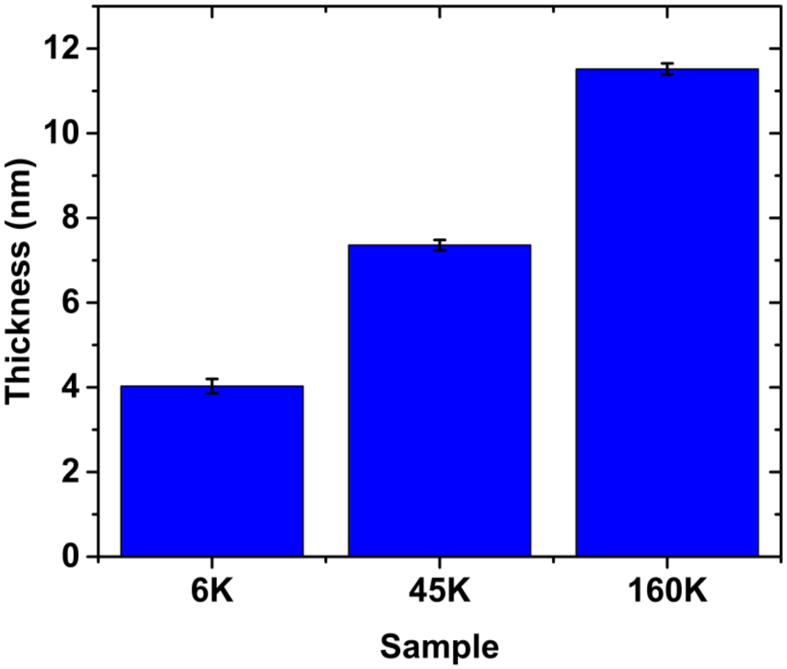

Figure 4.1 Ellipsometry results of the 1.5 wt% 6K, 45K and 160K PMMA films before infiltration. This data shows a clear increase in the brush thickness with increasing molecular weight, yielding a suitable range of thicknesses for investigation.

As discussed in section 4.2, the PMMA films were exposed to an Al VPI process at two different temperatures of 100ºC and 200ºC using TMA as the precursor. This temperature variation was employed to determine the optimal infiltration temperature for the various molecular weights, the results of which were analysed using HAXPES. Figure 4.2 shows the C1s high resolution spectra of the 6K, 45K and 160K PMMA pre and post infiltration for the different infiltration temperatures.

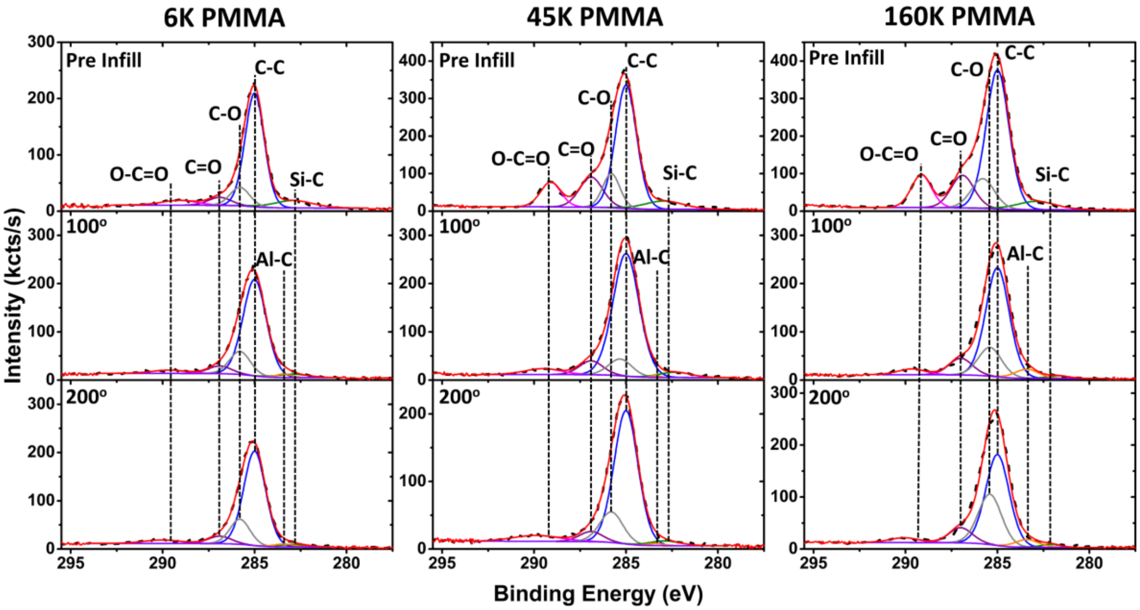

Figure 4.2 C1s high resolution HAXPES data showing the 6K, 45K and 160K PMMA pre and post Al infiltration at both processing temperatures. All peaks associated with the PMMA structure can be seen in all molecular weight cases with a large decrease in the C=O post infiltration indicating successful infiltration.

When examining the pre infiltrated PMMA brushes in the case of all molecular weights the main peak seen is that at 285 eV which is attributed to the carbon backbone of the polymer [17]. There are also peaks seen at 286.9 eV, 287.66 eV and 289.1 eV which correspond to the C-O, C=O, and O-C=O bonds respectively [18]. This agrees with the PMMA structure seen in Figure 1.11 and XPS analysis conducted in the field. The final peak seen within the pre infiltrated spectra is at 282.9 eV which attributed to Si-C bonds [7]. When comparing this to the post infiltrated films at both infiltration temperatures, firstly it is clear that there is a major decrease in the contribution of the C=O and O-C=O peaks with a slight increase in the C-O peak. This is the point at which the TMA interacts with the PMMA causing the C=O to break down, allowing it to then bind to the free electrons within the O atom. This also leads to the formation of more C-O bonds thus causing the C-O peak intensity to increase. This decrease in C=O indicates that infiltration was in fact successful. However, as there is still a contribution from these peaks this indicates that the films were not fully infiltrated. This could be due to infiltration occurring in the first few nanometres of the film close to the surface inhibiting precursor penetration further down into the film. Finally, in the post infiltrated film there is a new peak seen at 283.4 eV which is attributed to Al-C bonds. These bonds can be seen within the TMA precursor structure but they also could be caused by breakdown of the TMA allowing for the Al to bind with C atoms within the polymer [19,20]. This once again shows that polymer infiltration was successfully achieved.

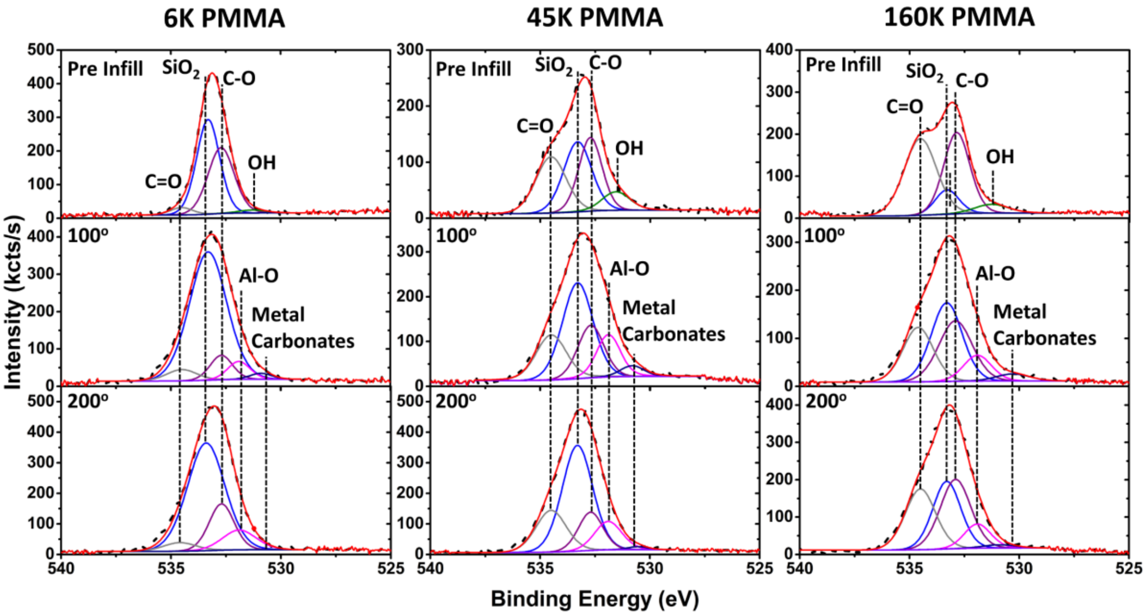

Figure 4.3 O1s high resolution HAXPES data showing the 6K, 45K and 160K PMMA pre and post Al infiltration. A clear decrease in the amount of C=O post infiltration once again indicates the point at which Al interacts with the polymer. The addition of the Al-O peak post infiltration also indicates successful infiltration.

Figure 4.3 shows the high resolution O1s spectra for the three different molecular weight PMMA films. These spectra were analysed for further insight into the interaction between the PMMA films and the TMA precursor. Firstly, all spectra pre and post infiltration show a clear peak at 533.3 eV which is related to the SiO_2 from the underlying substrate [21,22]. There are also clear contributions seen from peaks at 532.7 eV and 534.5 eV which correspond to the C-O and C=O seen in the polymer film respectively [23]. These peaks have a much larger contribution in the pre infiltrated films when compared to the films post infiltration at both temperatures. Once again, a decrease in the C=O peak can be seen agreeing with the C1s spectra in Figure 4.2, indicating that the C=O peak reduction corresponds to the point at which the PMMA interacts with the TMA precursor. Again, this peak is not completely quenched showing that the polymer films were not fully infiltrated. A peak is seen at

531.5 eV from all the pre infiltrated films indicates the presence of unreacted hydroxy groups on the surface of the PMMA [24]. Finally, for the films post infiltration, at both processing temperatures, a peak at 531.9 eV can be seen [2]. This is associated with Al-O bonds indicating once again that infiltration of the PMMA brushes was successful for all thicknesses. However, there is little variation in the intensity of this peak across the different molecular weights and infiltrating temperatures indicating that there is potentially little difference in the Al uptake between the different PMMA brushes.

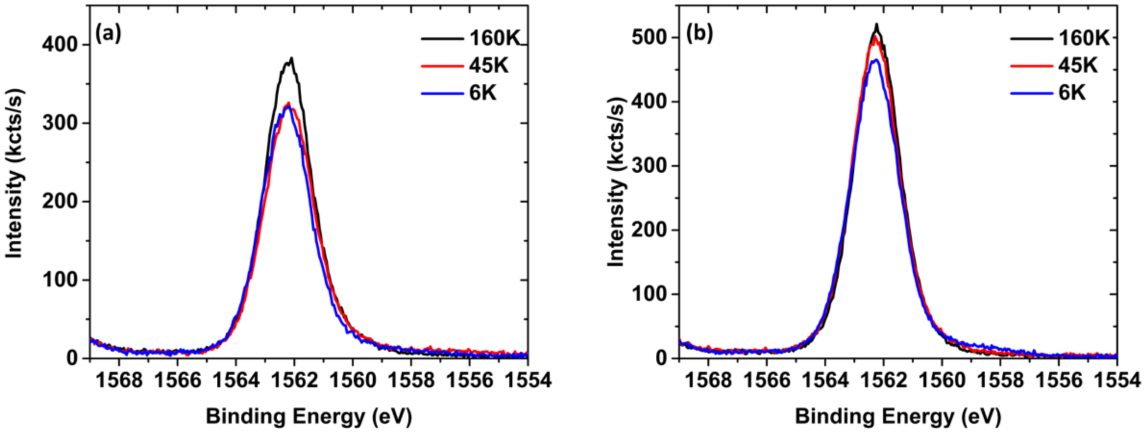

Figure 4.4 Al1s high resolution spectra for the 6K, 45K and 160K post (a) 100°C and (b) 200°C infiltrations. These spectra show negligible differences between the Al uptake across the different PMMA thickness with a small increase across the processing temperatures.

To further investigate the difference in Al uptake across the different molecular weight films and thus the different thickness, a direct comparison of the Al1s intensity was made, the results of which can be seen in Figure 4.4. It is clear that for 100°C processing temperature there is a small difference in the Al1s intensity between the 160K PMMA and the two other molecular weights. However, in the case of the 200 °C processing temperature there is a marginal difference in intensity when comparing the 6K to the 45K and 160K brushes. This was not expected as with the thicker brush it was believed there would be larger uptake. As stated previously infiltration occurring in the first few nanometres of the PMMA brushes could be inhibiting complete infiltration throughout the films. This is in agreement with the presence of the C=O peak post infiltration as not all bonds had reacted. There is also the potential for Al physisorption occurring on the thinner PMMA films thus leading to a larger Al1s signal. When looking at the two different process temperatures however, there is an increase in Al1s intensity in the films infiltrated at 200°C when compared to the ones infiltrated at 100°C in all molecular weight cases. It was then determined that the 200°C was more successful at infiltrating the PMMA brushes and would be used for future VPI processes.

Following on from the Al infiltration of the films, a study was conducted to compare two possible polymer removal techniques, a UV ozone and an ICP O_2 plasma process. This was carried out to examine which would be more successful and efficient at producing Al_2O_3 thin films from the infiltrated PMMA. It was also performed to investigate further whether the thicker PMMA brushes lead to a thicker resultant oxide since from the results seen from the films post infiltration there appeared to be little difference in Al uptake.

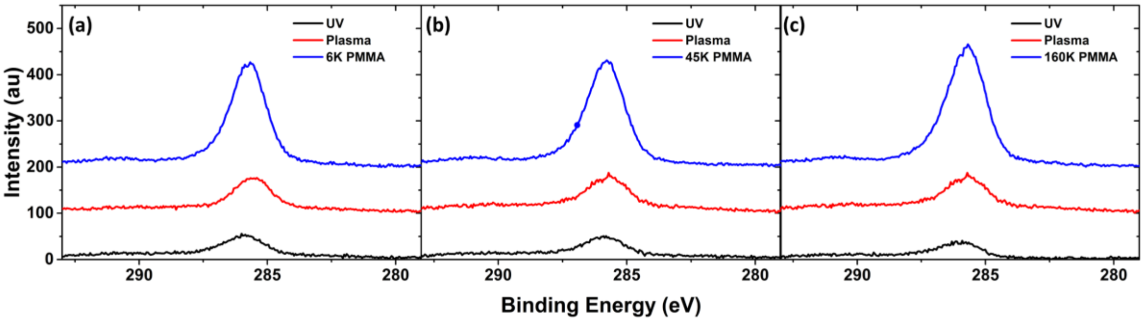

Figure 4.5 C1s spectra for the (a) 6K, (b) 45K and (c) 160K PMMA films before and after polymer removal via UV ozone and O_2 plasma treatments. A clear decrease in C1s intensity is seen post polymer removal showing both processes successfully removed the films from the silicon substrate.

Figure 4.5 shows the C1s spectra for the three different molecular weight films post infiltration as well as the Al_2O_3 films fabricated using the PMMA brushes post polymer removal. From this figure there is a clear decrease in the amount of carbon seen on the Al_2O_3 films post polymer removal compared to the PMMA brushes post infiltration. This shows that both methods successfully remove the polymer film. In saying this, there is still a small amount of carbon present on the Al_2O_3 films, this is attributed to adventitious carbon caused by atmospheric exposure after the removal processes. There is a slightly larger amount seen on Al_2O_3 films fabricated using the ICP O_2 plasma removal process. This is most likely because the surfaces of substrates treated using an O_2 plasma can become more reactive than that of substrates treated using UV ozone. This allows for a larger amount of carbon within the atmosphere to react with these substrates.

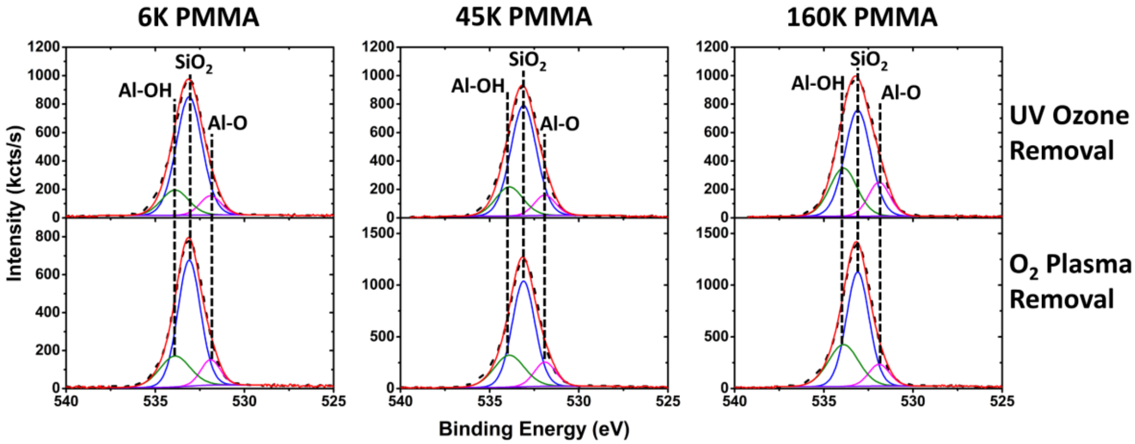

Figure 4.6 O1s high resolution spectra for the Al_2O_3 films fabricated using the three different molecular weight PMMA brushes after UV ozone and O_2 plasma treatments. Here clear contributions can be seen from the Al_2O_3 films with larger peak intensities seen in the films fabricated using the thicker PMMA brushes.

Following on from this the O1s high resolution spectra were studied. This was done to investigate the chemical environment of the oxygen atoms in the Al_2O_3 films and to examine whether the polymer removal process had any influence on these thin films. Figure 4.6 shows the O1s high resolution spectra for the Al_2O_3 films fabricated using the infiltrated 6K, 45K and 160K PMMA brushes using the two different polymer removal techniques. From each spectra there are three peaks seen at 531.9 eV, 533.3 eV and 533.9 eV which are associated with the Al-O, SiO_2 substrate and Al-OH bonds respectively [2]. This shows that for all molecular weight cases, the PMMA brushes could be successfully used in the fabrication of Al_2O_3 films. It is also clear that there is no variation in the peak structure for each of the O1s spectra indicating no difference in the way in which the two polymer removal techniques oxidise the infiltrated Al.

When comparing the intensity of the O1s constituent peaks for the films fabricated with the 6K, 45K and 160K PMMA there is a larger contribution from the Al-O and Al-OH peaks in the films fabricated using the higher molecular weight PMMA. This shows that the resultant oxide films fabricated with the thicker PMMA brushes are thicker than those fabricated with the thinner PMMA brushes. This increase is more prevalent in the Al_2O_3 films oxidised using the ICP O_2 plasma process than those which used the UV ozone. This indicates that a larger amount of Al was oxidised forming the resultant Al_2O_3 films fabricated using the higher molecular weight PMMA brushes which were subsequently removed using the ICP O_2 plasma. This could be due to the more aggressive nature of the O_2 plasma process, but it is noted that the Al_2O_3 films fabricated using the plasma process have large Al contributions indicating a thicker resultant oxide.

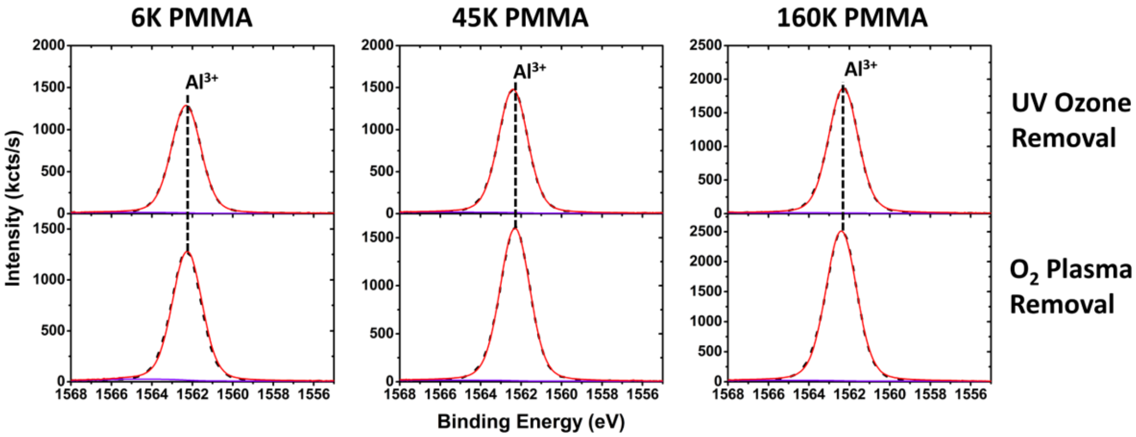

Figure 4.7 Al1s high resolution spectra for the three Al_2O_3 films fabricated using the different molecular weight PMMA brushes after UV ozone and O_2 plasma treatments. The increase in intensity with respect to the molecular weight of the polymer shows that the thickness of the Al_2O_3 films increases with the thickness of the fabricating PMMA.

Finally, to further show any effect that the polymer removal process may have on the resultant Al_2O_3 films the Al1s high resolution spectra were analysed, the results of which can be seen above in Figure 4.7. The fits of these spectra show only one contributing peak which is associated with the Al^{3+} seen at 1562.3 eV [25]. There is clearly no variation in the spectra compositions or peak structures when comparing the two different removal processes, once again confirming that the polymer removal process has no effect on the resultant oxide film. As the O_2 plasma process is significantly faster than that of the UV ozone it was deemed the more favourable option for the removal of the PMMA brushes. There also is a clear increase in Al1s intensity for the O_2 plasma process when comparing the polymer removal processes indicating that the UV ozone process could potentially be fabricating less dense films than that of the O_2 plasma thus making it a better choice.

From Figure 4.7 a clear increase in Al1s intensity with respect to the fabricating polymer molecular weight can be seen. This indicates that the higher molecular weight and therefore thicker PMMA brushes had a larger uptake of Al which was not as clearly seen as the previous post infiltrated film results.

Finally, ellipsometry measurements of the resultant Al_2O_3 films for both removal processes were measured the results of which can be seen in Figure 4.8 below. It is clear that the films which were fabricated using an ICP O_2 plasma removal process are thicker for all fabricating polymer molecular weight cases than those using the UV ozone removal process. This is thought to be due to the O_2 plasma being more effective at oxidising the Al within the polymer film thus creating a denser and thicker brush. It is also clear that there is an increase in the final film thickness with respect to the fabricating polymer molecular weight (and therefore polymer film thickness), with the thicker PMMA brushes fabricating a thicker resultant Al_2O_3 film. These results confirm that the thickness of a PMMA brush does effect its ability to be infiltrated by Al through a VPI process, with thicker films having a larger uptake resulting in thicker oxide films.

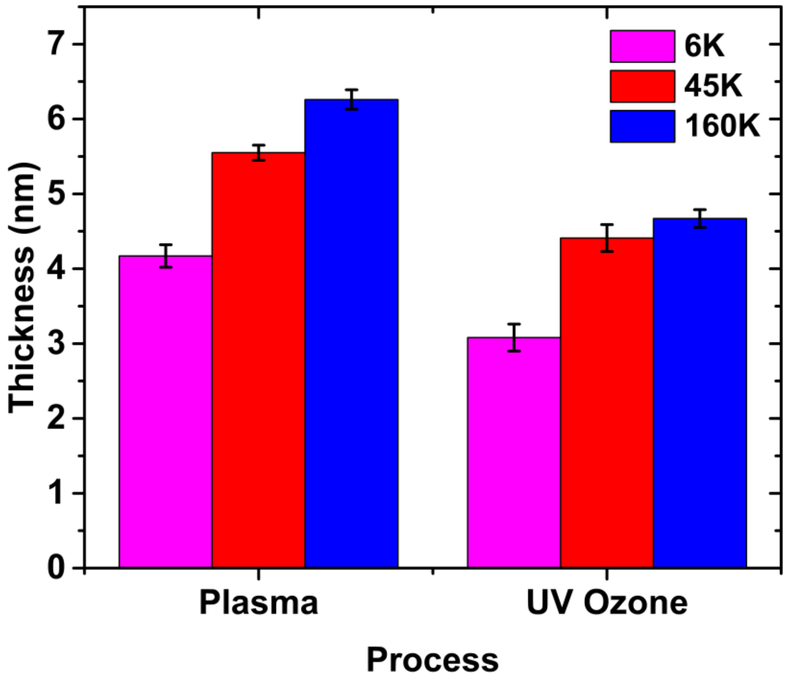

Figure 4.8 Ellipsometry results for the Al_2O_3 films post polymer removal via UV ozone and O_2 plasma treatments. This shows a clear increase in the resultant oxide thickness with respect to the molecular weight of the fabricating PMMA as well an increase in thickness with respect to the polymer removal process.

4.3.2 Effect of PS brush thickness on blocking capability for a hafnium oxide ALD process

As was the case for the PMMA study detailed above, three PS polymer brushes were fabricated at a range of thicknesses. The combinations of molecular weights and weight percentages used were as follows: 42K 0.2 wt%, 16K 0.2 wt% and 42K 1.5 wt%. These combinations were chosen as from Chapter 3 they were shown to provide a suitable thickness range for this study. Figure 4.9 shows the ellipsometry results for these films with the thickness values obtained being approximately 3 nm, 5 nm, and 11 nm respectively.

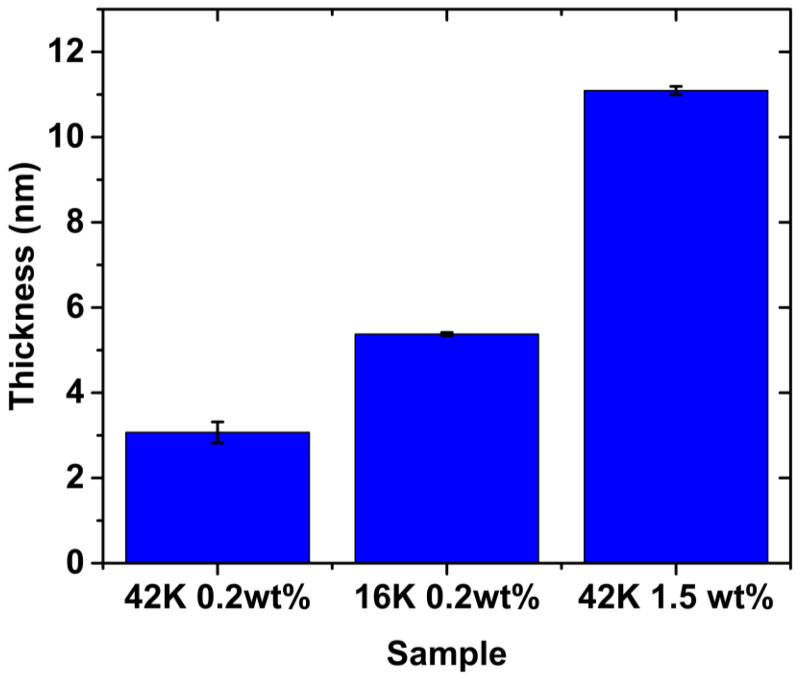

Figure 4.9 Ellipsometry results for the PS samples used for the Hf study showing the range of thicknesses that were investigated. The molecular weight and solution concentration varies for each sample so this range could be obtained.

Once the thickness of these films was determined they were placed in the ALD reaction chamber, with a Si reference sample, and were exposed to the HfO_2 process described in section 4.2.3. The three PS polymer brushes were first subjected to a total of 120 cycles. This was done sequentially meaning that throughout the deposition process the samples were periodically transferred, in vacuum, to the XPS system. This allowed for the detailed analysis of the films throughout the entire ALD process. Using the XPS data, the Hf concentrations were calculated for each sample. This allowed for the tracking of the Hf deposition on each sample as well as a silicon reference sample throughout the ALD process. These results can be seen below in Figure 4.10 (a).

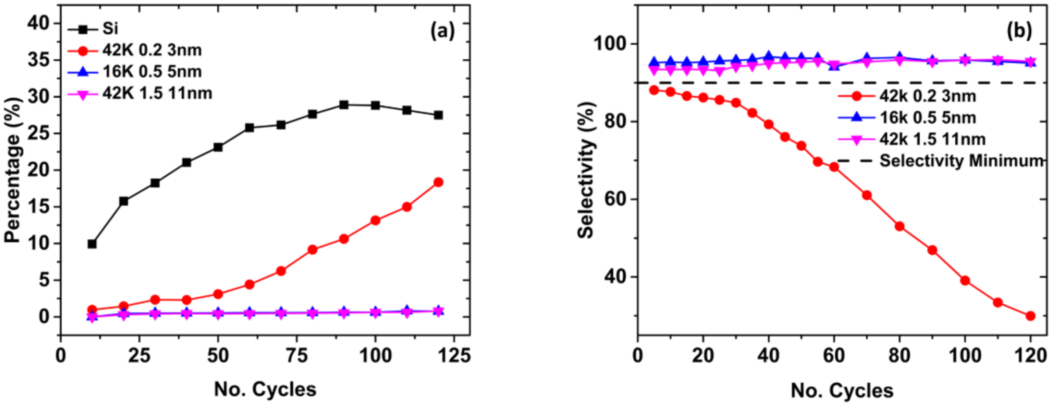

Figure 4.10 Calculated compositions from XPS data for the (a) Hf 4f for each PS brush and a silicon reference sample, as well as (b) the calculated selectivity of these films comparing them to the selectivity minimum reported in the literature. This data shows a definite increase in the percentage Hf and a decrease in the selectivity for the thinnest PS brush.

When examining the Hf4f peak profiles throughout the ALD deposition shown in Figure 4.10 (a), it is clear that there is a rise in the percentage of Hf present on the 42K 0.2 wt% film, this being the thinnest of the three tested brushes. After approximately 60 cycles the amount of Hf deposition begins to rapidly increase on the thinnest brush. The total Hf percentage on this film however never reached the same value as that deposited on the Si reference. This showed that while the sample had the weakest blocking capabilities it still inhibited deposition. The two thicker PS brushes, films fabricated with the 0.5 wt% 16K PS and the 1.5 wt% 42K PS, see no increase in the Hf percentage throughout the ALD process meaning that no deposition occurred on these thicker brushes. When comparing these results, it is clear that the thickness has a contributing factor to the PS brush's ability to block a HfO_2 ALD process. It is notable that the molecular weight used to fabricate the thinnest brush is the same as that of the thickest film so this difference in blocking efficacy can solely be attributed to the thickness of the brush and not the polymer's molecular weight.

Through the use of the XPS data the selectivity of each of the films was also calculated. This illustrates the quality of the films as well as showing that they provided sufficient blocking capabilities for the use in ASD. Selectivity was evaluated using the adapted standard selectivity equation defined by Gladfelter [26]. This equation is as follows:

$$S_{PS} = \frac{I_{Si} - I_{PS}}{I_{Si} + I_{PS}} \qquad \text{Eqn(4.1)}$$

Where I_{Si} and I_{PS} represent the intensity (peak area under the curve in cts^{-1}) of the Hf4f core level for the PS and Si samples. The results of these calculations can be seen in Figure 4.10 (b). There is a consensus in the field of ASD that for a selective process to be considered successful a selectivity of 90% or more must be achieved [27]. It is clear that the 0.5 wt% 16K and the 1.5 wt% 42K films satisfied this requirement, showing a selectivity of above 0.9 for the total 120 cycles. Whereas the thinnest PS brush shows a steady decline in selectivity throughout the ALD process once again showing the thickness dependence on the PS's blocking efficacy.

As previously stated, for the two thickest PS brushes there was no Hf deposition seen over the first 120 cycles. To further test the blocking efficacy of these films the experiment was repeated using the same parameters but for a total of 325 cycles. Once again this was done sequentially to monitor the HfO_2 deposition throughout the ALD process. Figure 4.11 shows both the calculated Hf concentration of these films and their respective selectivity. From Figure 4.11 (a) a clear increase in Hf percentage can be seen for the 0.5 wt% 16K PS film. This occurred after approximately 150 cycles of the ALD process. Similar to the results seen for the thinnest PS brush there is also a decrease in the 0.5 wt% 16K PS films selectivity shown in Figure 4.11 (b) at the point deposition began. However, from this data it is also clear that the 1.5 wt% 42K PS brush, which was the thickest film tested, once again had no indication of HfO_2 deposition with no decrease in selectivity also. From this it was concluded that the thickest film could block up to 325 cycles of a HfO_2 ALD process, and through the use ellipsometry measurements performed on the Si reference sample, it was determined that this process results in approximately 19 nm of HfO_2 deposition.

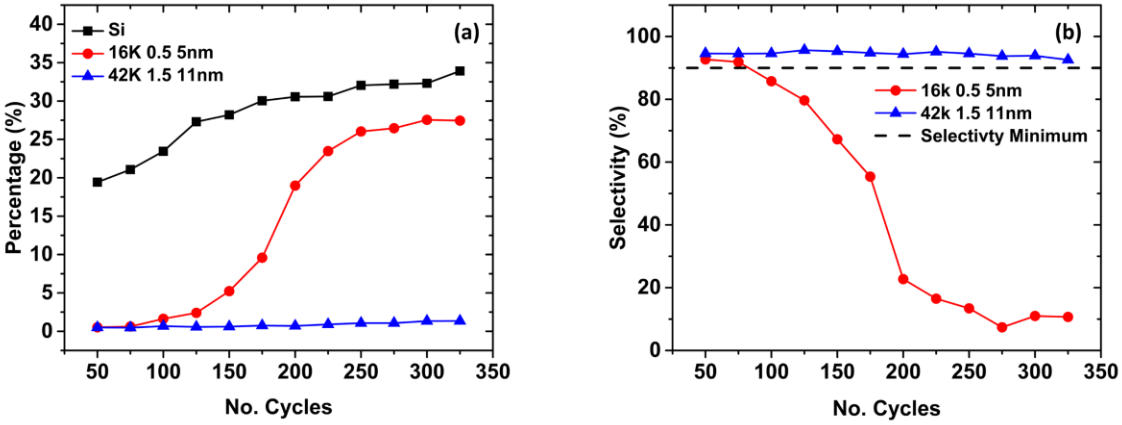

Figure 4.11 Calculated compositions from XPS data for the (a) Hf 4f for each PS brush and a silicon reference sample as well as (b) the calculated selectivity of these films comparing them to the selectivity minimum seen in literature. This data shows a definite increase in the percentage Hf and a decrease in the selectivity for the thinner of the two PS brushes.

To determine the cause of HfO_2 deposition on the thinner PS brushes, the ratio of the Si2p to the C1s was calculated for both ALD processes, the results of which are shown below in Figure 4.12. From this data it is clear that in both the 120 and 325 cycle cases, there is a clear drop in this calculated ratio at the point at which the 0.2 wt% 42K PS and the 0.5 wt% 16K PS allow Hf deposition. This drop is indicative of carbon breakdown which means that throughout the ALD process these thinner brushes are slowly breaking down thus eventually allowing HfO_2 deposition after a sufficient number of process cycles.

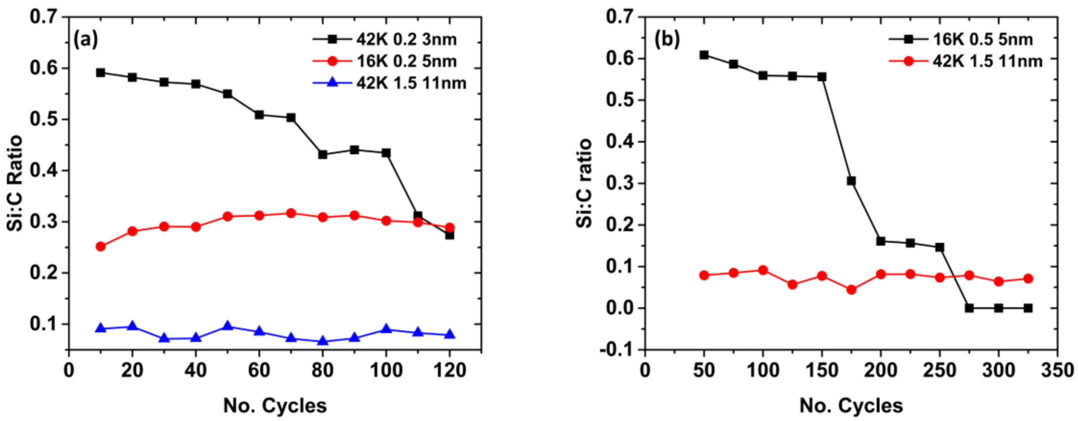

Figure 4.12 Calculated Si2p to C1s intensity ratios for the (a) 120 cycles and (b) the 325 cycle ALD processes. In both cases a significant drop in this ratio can be seen for both of the thinner PS brushes at the point at which Hf deposition occurred. This shows that the PS films were breaking down during the ALD process facilitating Hf deposition.

To further establish this proposed explanation, detailed fitting of the C1s spectra was conducted for each of the polymer films throughout the ALD process, the results of which are shown in Figure 4.13. When looking at the 1.5wt% 42K PS, which was the thickest film studied, there is no change in the peak structure throughout the 325 cycle process. The only peaks observed within this spectrum are the C-C and C-O at 285 eV and 286 eV respectively. The C-C contribution originates from the PS structure itself shown in Figure 1.11 whereas the C-O comes from the tethering of the polymer chains to the silicon substrates which forms during the condensation reaction in the grafting-to fabrication process. It is clear from Figure 4.13 that there is no change in this peak structure throughout the ALD process indicating no breakdown of the polymer, which was as expected. Comparing this to the 0.2 wt% 42K PS and the 1.5 wt% 16K PS films a clear broadening of the C1s peak can be seen over the course of the ALD process. This shows an increased contribution from the C-O peak within both spectra. This indicates breakdown in the polymer film as proposed previously because the C-O bond originates from the binding of the PS chains to the Si substrate so as the film is being broken down this leads to a stronger contribution from those bonds within the C1s peak. It is proposed that physisorption of the $HfCl_4$ precursor preferentially occurs at regions of polymer film breakdown. This initial physisorption thus allows for active regions for further Hf deposition enabling the HfO_2 to grow.

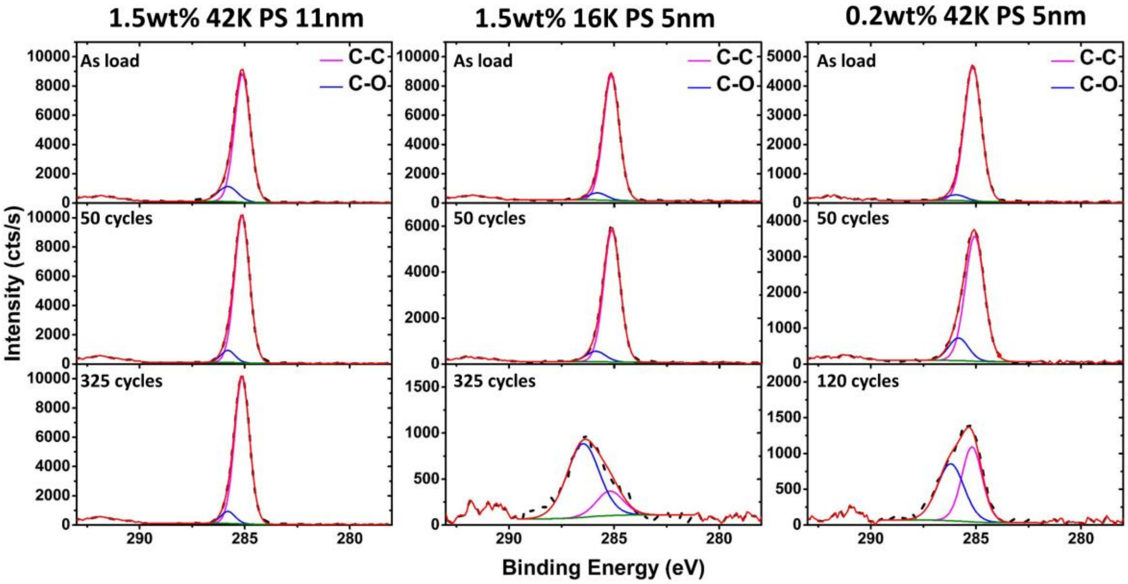

Figure 4.13 C1s high resolution XPS spectra for the three different PS brush thicknesses over the course of the ALD process. For the 3 nm and 5 nm brushes there is a clear broadening of the peak which is indicative of polymer breakdown compared to that of the 11 nm film where no broadening can be seen.

Once both ALD processes were carried out the PS brushes were exposed to an ICP O_2 plasma, which, as illustrated in the PMMA study, is a very effective polymer removal process. This was done to investigate whether the deposited HfO_2 on the thinner PS brushes seen in previous results was removed along with the PS brushes. This polymer removal process was performed on the 3 nm film after the total 120 cycles and the 5 nm and 11 nm films after the 325 cycles. Figure 4.14 shows the Hf4f high resolution XPS spectra for each of the polymer thicknesses post polymer removal and a Si reference. From this figure there is a clear increase in Hf4f intensity with respect to decreasing PS thickness. This shows that the HfO_2 layer was not removed with the polymer during the ICP O_2 plasma process. However, this data does also illustrate once again the dependence that PS brush thickness has on its ability to block an HfO_2 ALD process since it is clear that there is no Hf present on the substrate which had the 11 nm PS brush present.

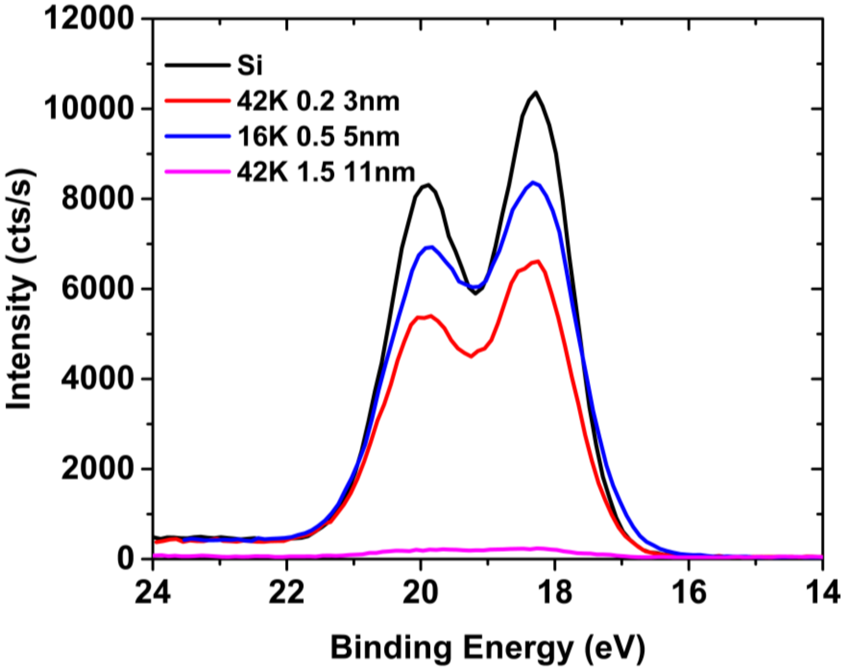

Figure 4.14 Hf4f spectra of the three different thickness PS brush and Si reference post plasma removal. This shows that the Hf is not removed with the polymer using an O_2 plasma process and shows how no deposition occurs on the thickest PS film.

Overall, from these results it can be concluded that the thickness of a PS brush has a large effect on its ability to block an HfO_2 ALD process with a thicker brush being more favourable. This result is very important for the field of ASD research because current methods used for area deactivation, such as SAMs which was discussed in section 1.2.7, have significantly longer fabrication times compared to polymer brushes.

4.4 Conclusions

The effect that PMMA and PS brush layer thickness have on their ability to be either infiltrated or to block infiltration, respectively, has been presented. Firstly, the relationship between PMMA thickness and its uptake of Al through a VPI process was shown. The process temperature dependence on the Al uptake was also investigated. Through the use of HAXPES it was seen that for all PMMA thicknesses and VPI process temperatures each brush was successfully infiltrated. This was demonstrated through the fitting of the C1s and O1s high resolution spectra for each polymer thickness and process temperature, pre and post infiltration. Prior to infiltration clear peaks associated with C=O and C-O bonds could be seen in both the C1s and O1s high resolution spectra, both of which are present within the PMMA structure. Once infiltration was carried out there was a clear decrease in the C=O peak indicating that this was the point at which the TMA precursor had interacted with the PMMA. There was also the appearance of an Al-C and Al-O bonds seen within the C1s and O1s spectra respectively. The Al1s intensity was then compared to examine whether there was an increase in Al with respect to thickness for each processing temperature. There was no significant difference observed between the different PMMA thicknesses, however there was an increase when comparing the two infiltration temperatures with the 200ºC process being more suitable as it provided the energy to create a larger amount of free volume within the polymer films creating more space for infiltration.

Following on from this, a study into the relative efficiencies of the two polymer removal processes – UV ozone or an ICP O_2 plasma – was carried out. The purpose of this experiment was to examine whether there was any variation in the resultant oxide thickness with respect to the fabricating PMMA brush film thickness, since no such relationship was established for the infiltrated polymers. Once again using HAXPES, the data showed that both removal processes successfully removed the polymer film, as well as oxidising the infiltrated Al, fabricating Al_2O_3 thin films. When comparing the Al1s high resolution spectra for samples subjected to the two processes there was a clear increase in intensity with respect to the fabricating polymer thickness, as well as a small increase in intensity, for the UV ozone process compared to the ICP O_2 plasma process. Because the plasma process was shorter it may be viewed as the favourable polymer removal process from an industrial perspective. Ellipsometry was then used to confirm the increase in oxide thickness with respect to the fabricating polymer thickness. From this data it was clear that there was an increase in Al_2O_3 thickness with respect to the thickness of the fabricating PMMA with the thicker brushes creating a thicker resultant oxide.

Finally, the relationship between PS brush thickness and its blocking capabilities for an HfO_2 ALD process was demonstrated. Using in-situ XPS, a distinct correlation between the thickness of the PS brush and their blocking efficacy was demonstrated. This was shown through the calculation of the Hf concentration on each of the PS brushes throughout the course of the ALD processes. From this it was shown that there was significantly less HfO_2 deposition on the thickest 11 nm PS film when compared to the 3 nm and 5 nm films, with no significant deposition after a total of 325 cycles. Through the fitting of the C1s XPS spectra it was shown that deposition on the thinner PS brushes was caused by film breakdown as there was a clear broadening of the C1s peak with larger contributions seen from the C-O peak signal from the silicon substrate-polymer interface region. Finally, these films were exposed to an ICP O_2 plasma process to see whether removing the polymer film also removed the deposited HfO_2 layer. Comparing the Hf4f intensities showed that the HfO_2 was not removed during the removal of the PS brush. It, however, did illustrate once again the relationship between PS thickness and its blocking efficacy as there was an increase in Hf intensity with decreasing PS brush layer thickness.

From the results presented in this chapter we can conclude that the thickness of the PMMA and PS polymer brushes have a significant effect on their ability to either be infiltrated and enable, or to block, the vapour phase deposition of Al_2O_3 and HfO_2, respectively.

4.5 References

(1) Snelgrove, M.; McFeely, C.; Shiel, K.; Hughes, G.; Yadav, P.; Weiland, C.; Woicik, J. C.; Mani-Gonzalez, P. G.; Lundy, R.; Morris, M. A.; McGlynn, E.; O’Connor, R. Analysing Trimethylaluminum Infiltration into Polymer Brushes Using a Scalable Area Selective Vapor Phase Process. *Mater. Adv.* **2021**, *2* (2), 769–781. https://doi.org/10.1039/d0ma00928h.

(2) Snelgrove, M.; McFeely, C.; Mani-Gonzalez, P. G.; Lahtonen, K.; Lundy, R.; Hughes, G.; Valden, M.; McGlynn, E.; Yadav, P.; Saari, J.; Morris, M. A.; O’Connor, R. Aluminium Oxide Formation via Atomic Layer Deposition Using a Polymer Brush Mediated Selective Infiltration Approach. *Appl. Surf. Sci.* **2020**, *515*. https://doi.org/10.1016/j.apsusc.2020.145987.

(3) de Paula, C.; Bobb-Semple, D.; Bent, S. F. Increased Selectivity in Area-Selective ALD by Combining Nucleation Enhancement and SAM-Based Inhibition. *J. Mater. Res.* **2021**, *36* (3), 582–591. https://doi.org/10.1557/S43578-020-00013-4.

(4) Bobb-Semple, D.; Zeng, L.; Cordova, I.; Bergsman, D. S.; Nordlund, D.; Bent, S. F. Substrate-Dependent Study of Chain Orientation and Order in Alkylphosphonic Acid Self-Assembled Monolayers for ALD Blocking. **2020**. https://doi.org/10.1021/acs.langmuir.0c01974.

(5) George, S. M. Atomic Layer Deposition: An Overview. *Chem. Rev.* **2010**. https://doi.org/10.1021/cr900056b.

(6) Verlaan, V.; Van Den Elzen, L. R. J. G.; Dingemans, G.; Van De Sanden, M. C. M.; Kessels, W. M. M. Composition and Bonding Structure of Plasma-Assisted ALD Al 2O3 Films. *Phys. Status Solidi Curr. Top. Solid State Phys.* **2010**, *7* (3–4), 976–979. https://doi.org/10.1002/pssc.200982891.

(7) Iatsunskyi, I.; Kempiński, M.; Jancelewicz, M.; Vacuum, K. Z.-; 2015, undefined. Structural and XPS Characterization of ALD Al2O3 Coated Porous Silicon. *Elsevier*.

(8) Cianci, E.; Nazzari, D.; Seguini, G.; Perego, M. Trimethylaluminum Diffusion in PMMA Thin Films during Sequential Infiltration Synthesis: In Situ Dynamic Spectroscopic Ellipsometric Investigation. *Adv. Mater. Interfaces* **2018**, *5* (20), 1801016. https://doi.org/10.1002/ADMI.201801016.

(9) Vig, J. R. UV/Ozone Cleaning of Surfaces. *J. Vac. Sci. Technol. A* **1985**, *3* (3), 1027–1034. https://doi.org/10.1116/1.573115.

(10) Vesel, A.; Semeni~, T. Etching Rates of Different Polymers in Oxygen Plasma. *Mater. Technolgies* **2012**, *46*, 227–231.

(11) Taylor, G. N.; Wolf, T. M. Oxygen Plasma Removal of Thin Polymer Films. *Polym. Eng. Sci.* **1980**, *20* (16), 1087–1092. https://doi.org/10.1002/PEN.760201610.

(12) Cummins, C.; Weingärtner, T.; Morris, M. A. Enabling Large-Area Selective Deposition on Metal-Dielectric Patterns Using Polymer Brush Deactivation. *J. Phys. Chem. C* **2018**, *122* (26), 14698–14705. https://doi.org/10.1021/acs.jpcc.8b04092.

(13) Coffey, B. M.; Lin, E. L.; Chen, P.-Y.; Ekerdt, J. G. Area-Selective Atomic Layer Deposition of Crystalline BaTiO3. *Chem. Mater.* **2019**, *31* (15), 5558–5565. https://doi.org/10.1021/ACS.CHEMMATER.9B01271.

(14) Jiang, N.; Sen, M.; Endoh, M. K.; Koga, T.; Langhammer, E.; Bjo, P.; Tsige, M. Thermal Properties and Segmental Dynamics of Polymer Melt Chains Adsorbed on Solid Surfaces. **2018**. https://doi.org/10.1021/acs.langmuir.8b00122.

(15) Ferriol, M.; Gentilhomme, A.; Cochez, M.; Oget, N.; Mieloszynski, J. L. Thermal Degradation of Poly(Methyl Methacrylate) (PMMA): Modelling of DTG and TG Curves.

(16) NSLS-II | Beamline 7-ID-2 (SST2) Spectroscopy Soft and Tender 2 https://www.bnl.gov/nsls2/beamlines/beamline.php?r=7-ID-2 (accessed May 27, 2023).

(17) Snelgrove, M.; Mani-Gonzalez, P. G.; Bogan, J.; Lundy, R.; Rueff, J. P.; Hughes, G.; Yadav, P.; McGlynn, E.; Morris, M.; O'Connor, R. Hard X-Ray Photoelectron Spectroscopy Study of Copper Formation by Metal Salt Inclusion in a Polymer Film. *J. Phys. D. Appl. Phys.* **2019**, *52* (43), 435301. https://doi.org/10.1088/1361-6463/AB35B2.

(18) Pletincx, S.; Marcoen, K.; Trotochaud, L.; Fockaert, L.-L.; Mol, J. M. C.; Head, A. R.; Karslioğlu, O.; Bluhm, H.; Terryn, H.; Hauffman, T. Unravelling the Chemical Influence of Water on the PMMA/Aluminum Oxide Hybrid Interface In Situ. https://doi.org/10.1038/s41598-017-13549-z.

(19) Furlan, A.; Jansson, U.; Lu, J.; Hultman, L.; Magnuson, M. Structure and Bonding in Amorphous Iron Carbide Thin Films. *J. Phys. Condens. Matter* **2015**, *27* (4), 045002. https://doi.org/10.1088/0953-8984/27/4/045002.

(20) Miller, D. J.; Biesinger, M. C.; McIntyre, N. S. Interactions of CO2 and CO at Fractional Atmosphere Pressures with Iron and Iron Oxide Surfaces: One Possible Mechanism for Surface Contamination? *Surf. Interface Anal.* **2002**, *33* (4), 299–305. https://doi.org/10.1002/SIA.1188.

(21) Bogan, J.; Lundy, R.; McCoy, A.; O'Connor, R.; Byrne, C.; Walsh, L.; Casey, P.; Hughes, G. In-Situ Surface and Interface Study of Atomic Oxygen Modified Carbon Containing Porous Low-κ Dielectric Films for Barrier Layer Applications. *J. Appl. Phys.* **2016**, *120* (10). https://doi.org/10.1063/1.4962371/143014.

(22) Byrne, C.; Brennan, B.; McCoy, A. P.; Bogan, J.; Brady, A.; Hughes, G. In Situ XPS Chemical Analysis of MnSiO3 Copper Diffusion Barrier Layer Formation and Simultaneous Fabrication of Metal Oxide Semiconductor Electrical Test MOS Structures. *ACS Appl. Mater. Interfaces* **2016**, *8* (4), 2470–2477. https://doi.org/10.1021/ACSAMI.5B08044/ASSET/IMAGES/MEDIUM/AM-2015-08044M_0013.GIF.

(23) Oxygen | XPS Periodic Table - IE.

(24) Tanaka, S.; Taniguchi, M.; Tanigawa, H. XPS and UPS Studies on Electronic

Structure of Li 2 O.

(25) Faraci, G.; La Rosa, S.; Pennisi, A. R.; Hwu, Y.; Margaritondo, G. Al Intermediate Oxidation States Observed by Core Level Photoemission Spectroscopy. *J. Appl. Phys.* **1995**, *78* (6), 4091–4098. https://doi.org/10.1063/1.359866.

(26) Gladfelter, W. L. Reviews Selective Metallization by Chemical Vapor Deposition. *Chem. Mater* **1993**, *5*, 1372–1388.

(27) Parsons, G. N.; Clark, R. D. Area-Selective Deposition: Fundamentals, Applications, and Future Outlook. *Chemistry of Materials*. American Chemical Society June 23, 2020, pp 4920–4953. https://doi.org/10.1021/acs.chemmater.0c00722.

5 Comparison of Al uptake in the polymers PMMA, P2VP and PEO

5.1 Introduction

A detailed investigation into the Al uptake of the polymers PMMA, P2VP and PEO as well as a comparison of their infiltration mechanisms is presented. Section 1.2.5 discussed the separation and size of the nanostructures formed within a BCP structure and the dependency of these parameters on the Flory Huggins parameter (χ) which quantifies the degree of incompatibility between two different polymers. As expected, the value of χ is dependent on the polymers used for the fabrication of the BCP structure. PMMA is one of the most widely researched polymers for use in BCP systems because of its ease of infiltration. The χ value for a PMMA block PS system is approximately 0.041 [1]. The infiltration of P2VP has also be shown to be widely successful, similar to PMMA however the P2VP block PS system has a χ value of 0.11 [2]. This means that this BCP structure has the capacity to fabricate smaller nanostructures than that of the PMMA block PS system since a higher χ value leads to smaller domain size. Finally, the PEO block PS system has a χ value of 0.077 which means it will create smaller feature sizes in a BCP system than that of PMMA, but not as small as P2VP [3]. PEO, however, is significantly cheaper than that of PMMA and P2VP making it a favourable choice since it has the ability to create the small feature sizes required for current semiconductor manufacturing without incurring a large cost.

From the above discussion of the various χ values for each of the polymers PMMA, PEO and P2VP it is clear that a detailed understanding of the infiltration of these films as well as a comparison of their material uptake is vital for future BCP lithography work. While there have been many studies conducted looking at the infiltration of these brushes individually a detailed comparison of the three has not been widely studied [4–6]. This comparison is vital for future BCP work as knowing this information will help determine which polymer is suitable for the desired application.

Polymer brushes of the polymers P2VP, PEO and PMMA were fabricated using the same weight percent and molecular weight solution for this study. This ensured a direct comparison of the polymers' infiltration to be made, without the influence of other parameters. These films were then characterised prior to VPI processing using ellipsometry and XRR for the determination of the polymer brush thicknesses as well as density as these can be contributing factors to the uptake of the infiltrating material. Following on from this the three polymer films were exposed to a VPI process where TMA was used as the infiltrating precursor. HAXPES was then used for the analysis of the pre and post infiltrated films and it was seen that the P2VP brush had the largest uptake of Al uptake between the three different polymers. An ICP O_2 plasma process was then carried out for the removal of the polymer brushes as well as the oxidation of the infiltrated Al for fabrication of Al_2O_3 thin films. Once again, the resultant oxide films were analysed using HAXPES to investigate the effect that the infiltrating polymer has on the Al_2O_3 film. It was shown that the fabricating polymer had no effect on the chemical composition of the resultant oxide but as seen previously, the P2VP brush resulted in the thickest Al_2O_3 film, which was confirmed using ellipsometry.

5.2 Experimental techniques

5.2.1 Materials

Blanket silicon with native oxide was provided by our industrial collaborators (Intel). The polymers hydroxy-terminated PMMA (Mw = 6 kg mol^{-1} (6K), PDI = 1.25), hydroxy-terminated P2VP (Mw = 6 kg mol^{-1} (6K), PDI = 1.05) and hydroxy-terminated PEO (Mw = 6 kg mol^{-1} (6K), PDI = 1.02) were purchased from Polymer Source Inc. Canada and used as received. Toluene (anhydrous, 99.8%), tetrahydrofuran (THF) (anhydrous, 99.9%, inhibitor-free) and isopropyl alcohol (≥ 99.7%, FCC, FG) were purchased from Sigma Aldrich and used as received. Deionized water (resistivity = 18.2 MΩ cm) was also used.

5.1.1 Polymer Brush Fabrication

Polymer brush fabrication was conducted using the grafting to technique. All solutions were made at a 0.2 wt% concentration using a 6K molecular weight polymer dissolved in THF and toluene for the P2VP and PMMA/PEO samples respectively. These solutions were then spin casted onto a hydroxy functionalised silicon substrate (functionalised using an O_2 plasma process conducted in Henniker benchtop plasma system). Each sample was annealed at a specific temperature and time as shown in Table 5.1, which was done due to the varying glass transition and decomposition temperatures of each of the polymers used.

Table 5.1 Annealing parameters used for the fabrication of the PMMA, P2VP and PEO brushes.

Polymer	*Anneal Temperature (°C)*	*Anneal Time (mins)*
PMMA	200	30
P2VP	180	30
PEO	200	30

Finally, once annealed each sample was sonicated for 2 x 12 minute sonication periods in the solvent used for the fabrication of the original polymer solution to remove any ungrafted polymer chains.

5.2.2 VPI of Polymer Brushes and Polymer Brush Removal

VPI processing was conducted in an Oxford Instruments Flexal ALD system (base pressure 5 x 10^{-7} mbar). Samples were exposed to a N_2 gas flow which removed any dust and surface impurities from the sample prior to the VPI process. For sample loading each polymer was placed on a 100 mm steel carrier wafer. Once loaded the samples were left for 20 minutes to heat up to the process temperature of 100°C. The precursor used for this process was once again TMA. At the beginning of this process TMA was admitted into the ALD processing chamber using Ar (200 sccm) as the carrier gas for a dose time of 0.1 seconds. This was then followed by the isolation of the process chamber holding the precursor in vacuum for a total of 1 minute. Finally, the chamber was purged using Ar (200 sccm) for 20 seconds. This was repeated for a total of 250 cycles.

5.2.3 Characterisation Techniques

Ellipsometry data was recorded using a J.A. Woolam XLS-100 ellipsometer. All data analysis was performed with the CompleteEASE software using a multi-layer model. This type of modelling was used to not only take into account the polymer films but also the silicon substrate as well as the silicon oxide intermediate layer. Within this model three layers were inputted, the silicon substrate, a 2 nm silicon oxide layer and finally the respective polymer layer. The optical constants for each layer were obtained from the CompleteEase software from pre-determined models as the films in this study are well known and analysed. In all cases, three measurements were taken from different points on the sample and an average of these was calculated. The standard error of this was also determined.

HAXPES analysis was performed at the National Synchrotron Light Source II in Brookhaven National Laboratory using the SST-2 beamline [7]. Spectra were acquired with a photon beam energy of 2 keV. A Si(111) crystal monochromator was used. All data analysis was performed using the CasaXPS software.

XRR measurements took place at the I07 beamline of Diamond Light Source, Didcot, UK. An X-ray beamline with an energy of 10keV ($\lambda = 1.241$Å) and a spot size of 68 x 221 μm was used. Samples were mounted on the diffractometer stage enclosed in a plastic bag filled with argon to prevent surface damage by oxygen and ozone. All data analysis was performed using the GenX software.

5.2.4 Acknowledgements

The author would like to thank Mr Darragh O'Neill for his assistance in sample processing. The author would also like to thank Dr Matthew Snelgrove, Dr Conan Weiland, Mr Shane O'Donnell and Mr Feljin Jose for their help with the data acquisition.

5.3 Results

5.3.1 Polymer Fabrication and Infiltration

At the beginning of this work the thickness of each polymer film was measured using ellipsometry and XRR. This was carried out because the results shown in Chapter 4 illustrate the effect that the thickness of a polymer brush has on its ability to be infiltrated as well as its effect on the resultant oxide thickness. As each polymer was fabricated using the same weight percent solution as well as the same molecular weight this comparison allowed for thickness dependence to be seen just between the polymers. Figure 5.1 shows the ellipsometry results for the PMMA, P2VP and PEO brushes. From this data it is clear that the PMMA resulted in the thickest polymer film followed by the P2VP and then finally the PEO.

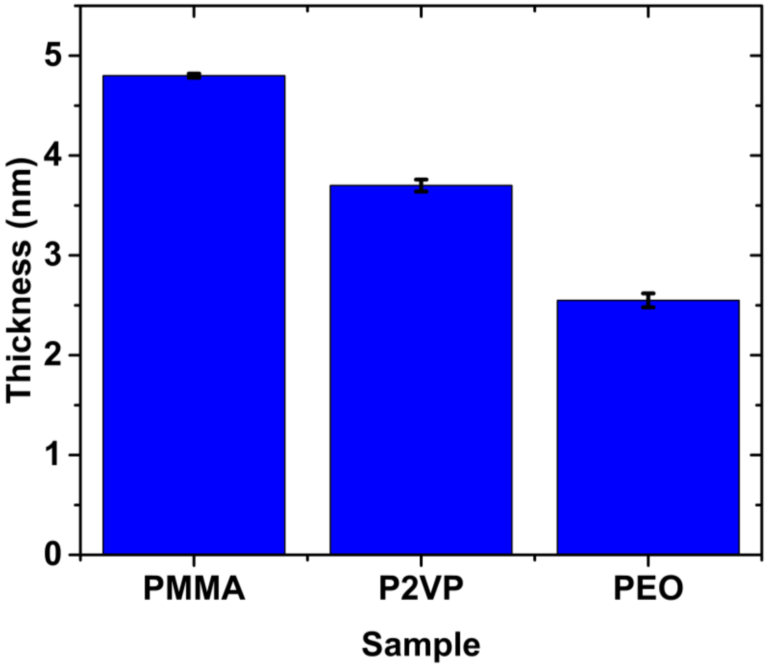

Figure 5.1 Ellipsometry results showing the thickness of the fabricated PMMA, P2VP and PEO brushes before infiltration. This shows that the PMMA brush to be the thickest of the three polymers followed by P2VP and then PEO.

From previous results it would be expected that since the PMMA film is the thickest it would yield the most amount of Al uptake when compared to the thinner brushes. However, due to the polymer's different properties and infiltrating mechanisms this may not be the case.

XRR was then conducted on each of the polymer films to confirm the thickness values observed using ellipsometry as well as to determine the density of the brushes. This is an important factor to take into account because the density of the polymer films could significantly influence their precursor uptake. Figure 5.2 shows the XRR results as well as the simulated fits for each of the polymer brushes.

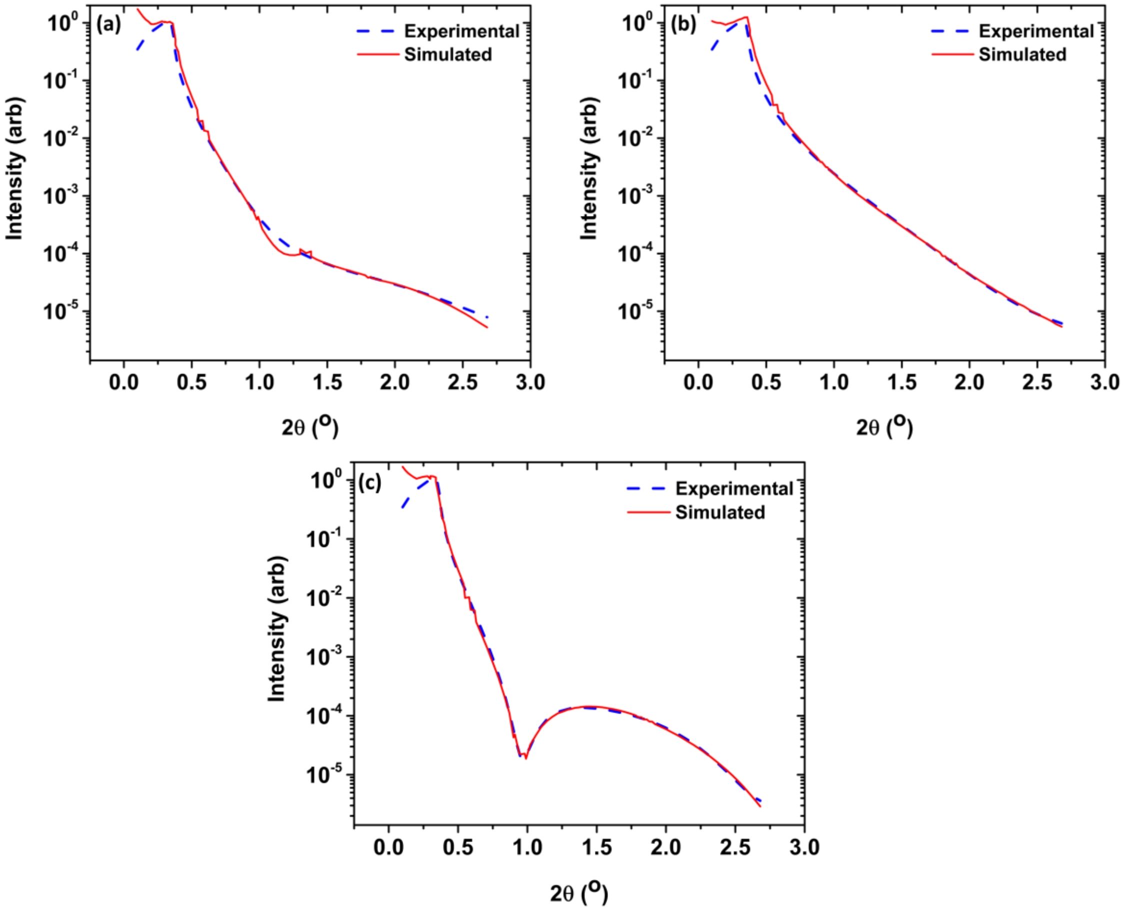

Figure 5.2 XRR results and simulated fits for the (a) P2VP, (b) PEO and (c) PMMA. From the number of oscillations seen within each spectrum once again the PMMA film can be seen to be the thickest brush fabricated.

Through qualitative analysis there is a clear difference in the number of oscillations seen between each of the spectra which relates to the thickness of the polymer film. It is clear that the PMMA brush has the largest and most pronounced oscillations compared to the P2VP and PEO brushes, indicating that it is the thickest of the three films, which is in agreement with the ellipsometry results. The depth of oscillation also indicates that the PMMA is the densest of the three films. This was confirmed through the fitting of the data allowing for further quantitative analysis to be conducted, the results of which can be seen in Table 5.2.

Table 5.2 Quantitative results of the density, thickness and roughness for the PMMA, P2VP and PEO brushes calculated through the use of a simulated fit.

Sample	***Density (g/cm^3)***	***Error (min/max)***	***Thickness (nm)***	***Error (min/max)***	***Roughness (nm)***	***Error (min/max)***
PMMA	1.13	-0.02, 0.03	4.31	-0.42, 0.38	0.84	-0.31, 0.11
P2VP	0.53	-0.05, 0.06	3.7	-0.13, 0.16	0.96	-0.30, 0.19
PEO	0.3	-0.15, 0.40	1.3	-0.10, 0.76	1.12	-0.25, 0.21

These results confirm the qualitative analysis of the XRR data with the PMMA being both the thickest and densest brush fabricated, followed by the P2VP and PEO films. This once again indicates the potential that the PMMA film has for significant Al uptake when exposed to the VPI process.

Following on from the determination of the polymer film thickness and density the films were exposed to the VPI process using TMA as the infiltrating precursor which was outlined in section 5.2.2. Following infiltration, the polymer brushes were analysed using HAXPES which was done to show whether the infiltration of the polymer brushes was successful as well as to determine the Al uptake within each of the polymer films. Figure 5.3 shows the high resolution C1s and O1s spectra of the PMMA brush pre and post Al infiltration.

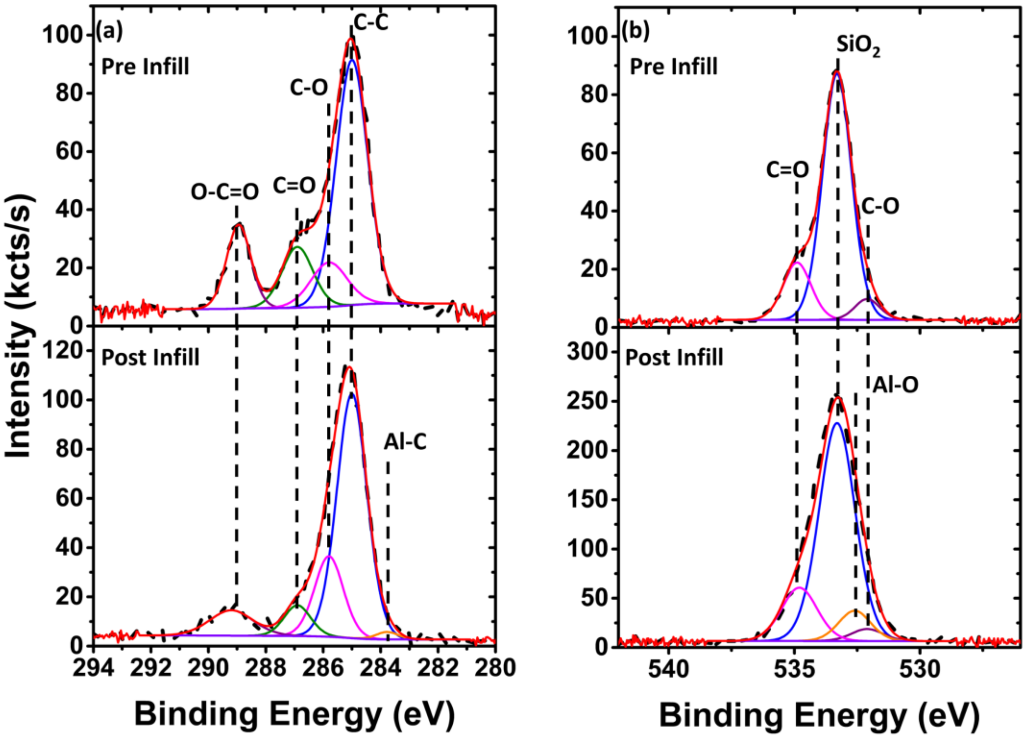

Figure 5.3 HAXPES high resolution spectra of the (a) C1s and (b) O1s for the PMMA brush pre and post infiltration. This shows the successful infiltration of these films through the appearance of the Al-C and Al-O bond signals seen in the C1s and O1s post infiltration spectra, respectively.

From Figure 5.3 (a) the high resolution C1s HAXPES spectra can be seen for the PMMA pre and post infiltration. In both cases there is a large contribution seen from the peak at 285 eV which is attributed to C-C bonds within the backbone of the PMMA chains [8]. The other peaks seen in both spectra are at 285.5 eV, 286.9 eV, and 289.1 eV which correspond to the C-O, C=O and O-C=O bonds respectively [9]. These can all be seen within the PMMA structure in Figure 1.11. When comparing the intensity of these peaks across the pre and post infiltrated PMMA films there is a clear decrease in the intensity of the peaks associated with the C=O structure and an increase in intensity in the C-O bonds post infiltration. This is due to the interaction between the Al precursor and the PMMA film. As discussed in Chapter 4 the way in which PMMA is infiltrated is through the breaking of the C=O bond allowing the infiltrating precursor to interact with the free electrons on the oxygen atom. This therefore creates the decrease in C=O peak signal seen as well as the increase in C-O peak signal. As also observed in Chapter 4, it can be determined that complete infiltration has not occurred within the PMMA film since there is still a contribution from the C=O structure within the post infiltrated spectra. Finally, within the post infiltrated film a peak at 283.7 eV can be seen which is from Al-C bonds present within the TMA structure [10,11]. This bond could also arise from the breakdown of the precursor allowing the Al to bond with the carbon atoms within the polymer structure. Both the decrease in C=O as well as the contribution of Al-C bonds in the post infiltrated spectrum indicate successful infiltration of the film.

Figure 5.3 (b) shows the high resolution O1s spectra of the PMMA films pre and post infiltration. The main peak seen in both spectra is attributed to the SiO_2 present on the substrate seen at 533.3 eV [12,13]. This peak has such a large contribution because the PMMA film is extremely thin. There are also clear contributions from peaks seen at 532.1 eV and 534.8 eV which are from the C-O and C=O bonds respectively [14]. Once again there is a decrease in the C=O contribution post infiltration with a slight increase in the C-O peak. This once again confirms the way in which the TMA precursor interacts with the PMMA film through the breaking of the C=O bond. There is a fourth peak seen in the post infiltrated film at 532.6 eV which is attributed to Al-O bonds [15]. As stated previously the Al within the TMA precursor bonds with the free electrons on the oxygen atom which originate from the breaking of the C=O. The appearance of this peak, as well as the peak due to the Al-C bond in the C1s post infiltrated spectrum, confirm the successful infiltration of the PMMA film.

Figure 5.4 shows the high resolution HAXPES spectra of the C1s and O1s for the P2VP film pre and post infiltration. From the C1s spectra seen in Figure 5.4 (a) the pre and post infiltrated spectra and comprised of the carbon backbone signal, C-C, at 285 eV and two more components seen at 285.5 eV and 286 eV which is from carbon seen within the pyridine ring namely the C=C and the C=N respectively [4,16,17]. There is a fourth peak seen in both the pre and post infiltrated spectra at 286.6 eV which is attributed to C-O [18]. This arises from the interface where the P2VP binds to the SiO_2 substrate, as well as contributions from surface oxidation due to atmospheric exposure. Finally, once again seen in the post infiltrated film there is a peak associated with Al-C bonds at 283.8 eV [10,11]. This indicates that the P2VP films were successfully infiltrated by the Al precursor.

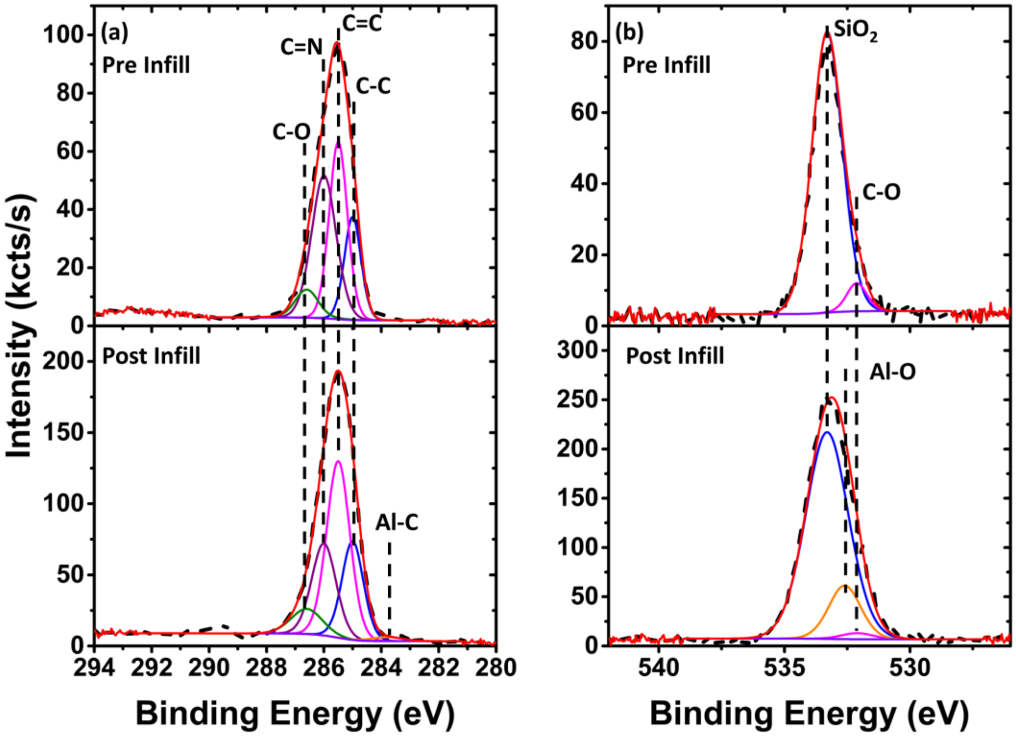

Figure 5.4 HAXPES high resolution spectra of the (a) C1s and (b) O1s of the P2VP brush pre and post infiltration. This shows the successful infiltration of these films through the appearance of the Al-C bond and Al-O bond seen within the C1s and O1s post infiltration spectra, respectively.

Figure 5.4 (b) shows the high resolution O1s spectra of the P2VP film pre and post infiltration. In both O1s spectra the main peak contributing to the fit is the at 533.3 eV which is attributed to the SiO_2 from the substrate [12,13]. There is a second peak seen in both the pre and post infiltrated spectra at 532.1 eV from the C-O bonds at the polymer substrate interface [19]. Finally, at 532.6 eV the peak associated with Al-O can be seen [15]. This confirms the successful infiltration of the P2VP films by the Al precursor.

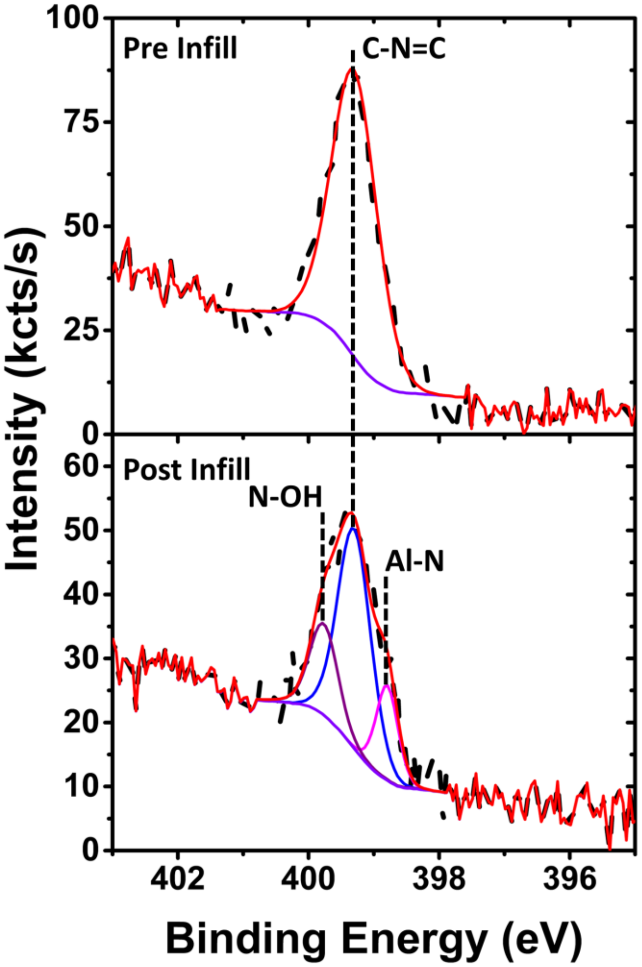

Figure 5.5 High resolution N1s spectra for the P2VP film pre and post infiltration. The fitting of this peak shows clear interaction between the nitrogen within the pyridine ring of the P2VP and the TMA precursor.

Figure 5.5 shows the N1s high resolution spectra for the P2VP brushes pre and post infiltration. Firstly, one common peak can be seen in both the pre and post infiltrated films, located at 399.3 eV, and is attributed to the nitrogen carbon bonds within the pyridine ring [20].

In addition to this, within the post infiltrated spectrum two additional peaks at 398.8 eV and 399.8 eV are present which are attributed to Al-N and N-OH bonds respectively [4,21–23]. The N-OH signal represents regions where the Al has not formed a chemical bond with the nitrogen. Al-N bonds show the infiltration mechanism of the P2VP to be through the interaction of the TMA precursor with the lone pair of electrons located within the nitrogen atom in the pyridine ring [24]. This once again demonstrates the successful infiltration of the P2VP brush by the TMA precursor.

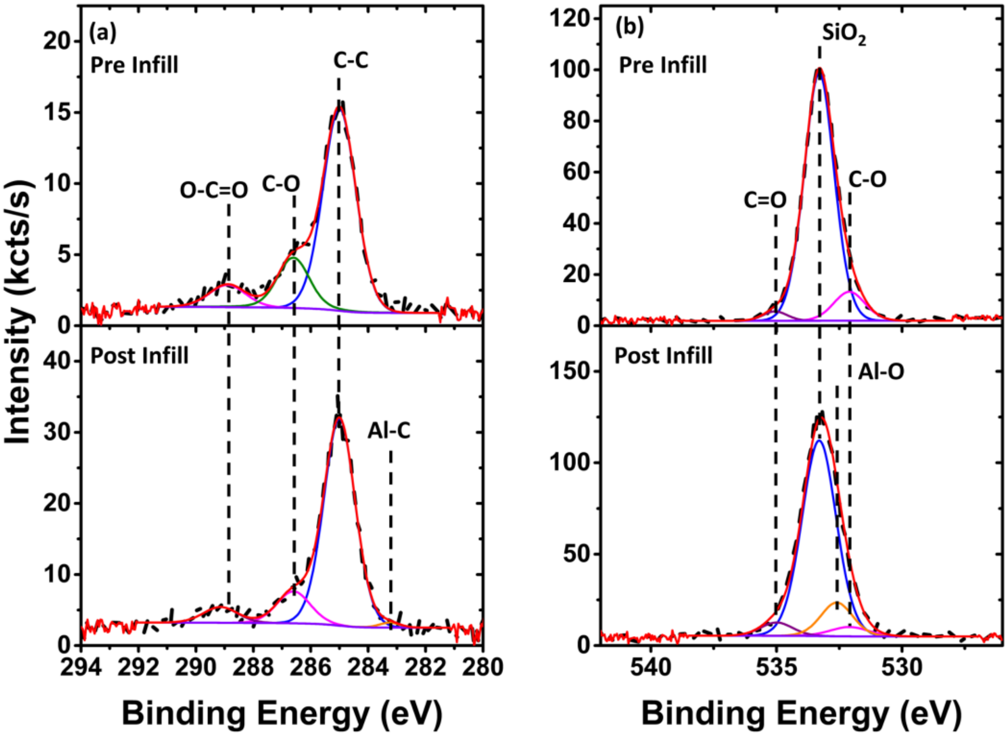

Figure 5.6 HAXPES high resolution spectra of the (a) C1s and (b) O1s of the PEO brush pre and post infiltration. This shows the successful infiltration of these films through the appearance of the Al-C bond and Al-O bond seen within the C1s and O1s post infiltration spectra, respectively.

Figure 5.6 shows the high resolution C1s and O1s spectra for the PEO films pre and post infiltration. The C1s spectra seen in Figure 5.6 (a) show a main peak contribution from the polymer backbone, C-C bonds, at 285 eV [25]. There are two additional peaks seen at 286.6 eV and 288.9 eV which correspond to C-O and O-C=O respectively. Finally, there is a small contribution seen from the Al-C bond within the post infiltrated spectrum at 283.3 eV showing that the film was successfully infiltrated [10,11].

In Figure 5.6 (b) the high resolution O1s spectra for the PEO films pre and post infiltration can be seen. Within both spectra the peak associated with the SiO_2 substrate can be seen at 533.3 eV, along with two other peaks at 532.1 eV and 535 eV, corresponding to the C-O and C=O bonds, respectively [12,25]. Once again, a contribution at 532.6 eV from Al-O bonds can be seen in the post infiltrated spectrum demonstrating that the infiltration of the PEO films was successful [15]. This bond also indicates the infiltration mechanism of the PEO brush. PEO contains an ethoxy group within its structure, which can be seen in Figure 1.11. The oxygen atom within these groups contain lone pairs of electrons thus allowing for the Al infiltration of the PEO brush [26–28].

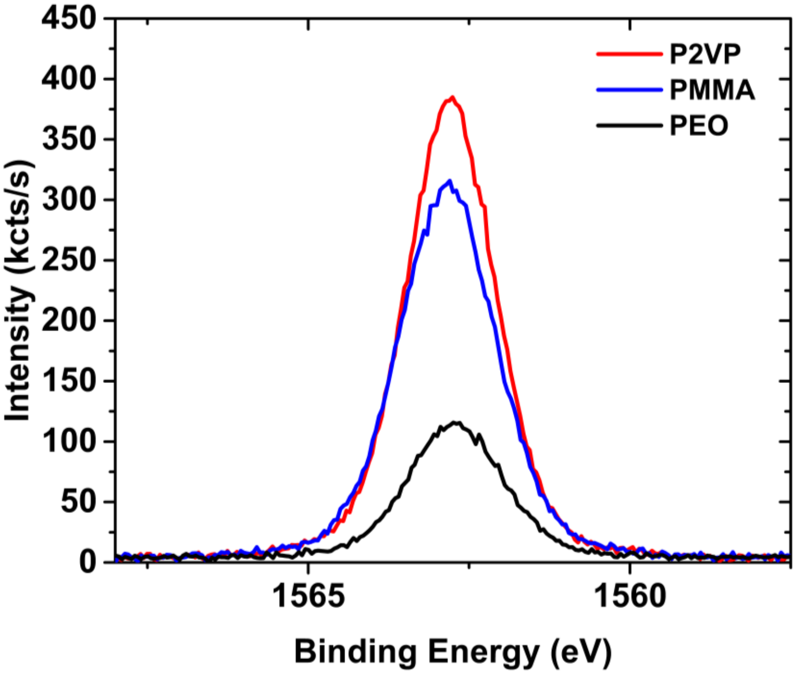

Figure 5.7 Al1s High resolution HAXPES spectra for the post infiltrated P2VP, PMMA and PEO films. There is a clear difference in intensity with respect to the infiltrating polymer with the P2VP having the largest Al uptake followed by the PMMA and PEO.

Following on from the analysis of the C1s and O1s high resolution spectra for each of the polymer films the Al1s was investigated, the results of which can be seen in Figure 5.7 above. Form this data a clear relationship between the Al1s peak intensity, which relates to the amount of Al present, and the fabricating polymer can be seen. It is clear that the P2VP had the largest uptake of Al as it has the largest Al1s intensity. This is followed by the PMMA and then finally the PEO. These results were not expected because, as stated previously, it was theorised that the PMMA brush would have had the largest Al uptake due to the fact that it was both thicker and denser than that of the P2VP. It was seen however that not all the reaction sites within the PMMA film were used since there was still C=O present within the C1s and O1s spectra seen in Figure 5.3. This could be due to steric hindrance caused by the first few nanometres of the PMMA film being infiltrated thus blocking further infiltration deeper within the brush. The larger amount of Al within the P2VP could also be due to more efficient infiltration as the lone pair of electrons of the nitrogen atom within the pyridine ring allow for an easier infiltration mechanism than that of the bond breaking mechanism at work in the PMMA brush. As the PEO relies on a lone pair of electrons for its infiltration this also shows that thickness and density have a contributing factor to the Al uptake since the P2VP brush is thicker and denser than the PEO film. This therefore creates more reaction sites for the Al to infiltrate.

5.3.2 Polymer Removal and Aluminium Oxidation

Following on from the successful infiltration of the PMMA, P2VP and PEO films an ICP O_2 plasma was used for polymer removal as well as the oxidation of the infiltrated Al for the fabrication of Al_2O_3 thin films. This removal process was chosen as it was demonstrated in previous results presented in Chapter 4 that it was the most efficient one for the removal of polymer films. Figure 5.8 shows the C1s high resolution spectra of the three polymer films post infiltration and post O_2 plasma treatment. From this data a clear decrease in C1s intensity can be seen post O_2 plasma treatment, which shows the successful removal of the polymer brush material. The small amount of remaining carbon seen on the samples can be attributed to carbon absorbed during atmospheric exposure of the substrates.

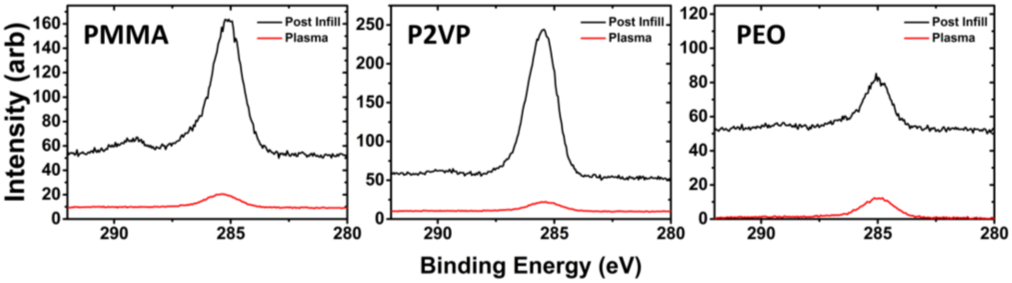

Figure 5.8 C1s high resolution spectra pre and post O_2 plasma treatment for the polymers PMMA, P2VP and PEO. This shows a decrease in the C1s intensity post plasma treatment, showing successful polymer removal.

Following on from this, the O1s high resolution spectra were studied to show that successful fabrication of Al_2O_3 thin films had been achieved. Figure 5.9 shows the high-resolution spectra for the Al_2O_3 films fabricated using the infiltrated PMMA, P2VP and PEO brushes. Each spectrum shows a contribution from a peak located at 533.3 eV attributed to the SiO_2 on the substrate [12,13]. Two other peaks can be seen at 532.6 eV and 534.5 eV which correspond to Al-O and Al-OH bonds within the Al_2O_3 film respectively [15]. This shows that each brush layer system enabled successful fabrication of Al_2O_3 films during the O_2 plasma polymer removal stage.

When comparing the intensity of the O1s constituent peaks, especially the Al-O and Al-OH peaks, there is a clear difference in intensity with respect to the fabricating polymer. The film fabricated using the infiltrated P2VP brush has larger Al-O and Al-OH intensities than that of the other two polymers. This indicates that the Al_2O_3 film fabricated using the P2VP brush is thicker in that of the films fabricated using the PMMA and PEO brushes. This is as expected as it was previously shown that the P2VP film had the largest amount of Al uptake and therefore had the greatest amount of Al present for subsequent oxidation.

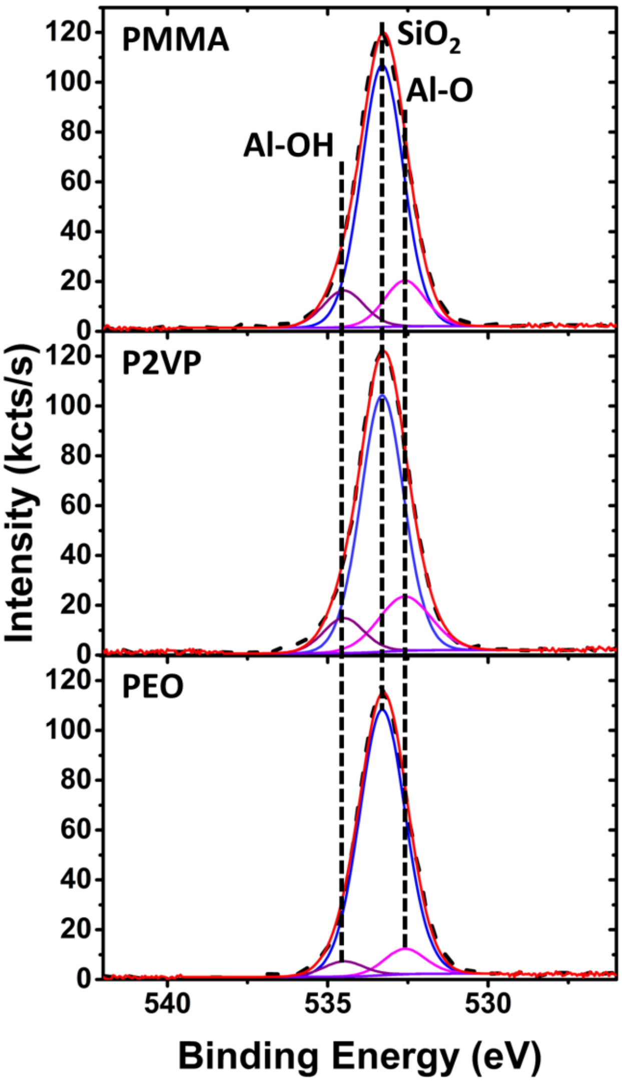

Figure 5.9 High resolution O1s spectra of the Al_2O_3 films fabricated using the PMMA, P2VP and PEO films post O_2 plasma processing. Clear contributions can be seen from the Al_2O_3 films, with the largest peak intensities seen in the P2VP film.

Al1s intensities were then compared to show the difference in the resultant oxide film thickness for each of the fabricating polymer brush layers. Figure 5.10 shows the Al1s high resolution spectra for the Al_2O_3 films fabricated using the infiltrated P2VP, PMMA and PEO brushes. There is a clear difference in the Al1s intensity between the three polymers which indicates a difference in thickness. As seen previously the film fabricated using the infiltrated P2VP brush has the largest Al1s intensity followed by the films fabricated using the PMMA and finally the PEO films. This shows that the P2VP brush resulted in the fabrication of the thickest Al_2O_3 film. Once again this was not the expected result as the P2VP brush was neither the thickest nor densest at the beginning of this experiment. However, due to the efficient infiltration mechanism of the lone pair of electrons on the nitrogen atom within the pyridine ring, this allowed for the largest amount of Al uptake and therefore the fabrication of the thickest resultant oxide film.

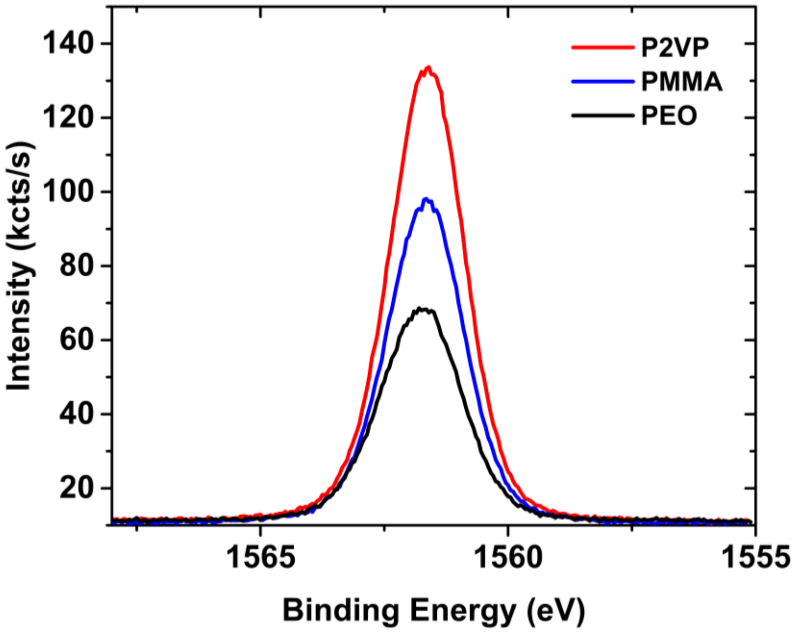

Figure 5.10 High resolution Al1s of the Al_2O_3 films fabricated using the infiltrated P2VP, PMMA and PEO brushes. This clearly shows the relationship between the fabricating polymer brush layer and the resultant oxide thickness since the intensity of the Al1s peak changes with respect to the fabricating polymer type, with the P2VP infiltrated brush resulting in the thickest Al_2O_3 film.

Finally, to complement the data shown in Figure 5.10 ellipsometry was carried out for the Al_2O_3 films post polymer removal, the results of which can be seen in Figure 5.11 below. This data clearly shows that the infiltrated P2VP brush fabricated the thickest resultant oxide film post polymer removal followed by the PMMA film and then finally the PEO. This is in agreement with all previously shown HAXPES data and therefore allows us to conclude that the P2VP brush is the most effective at being infiltrated as part of an aluminium oxide VPI process.

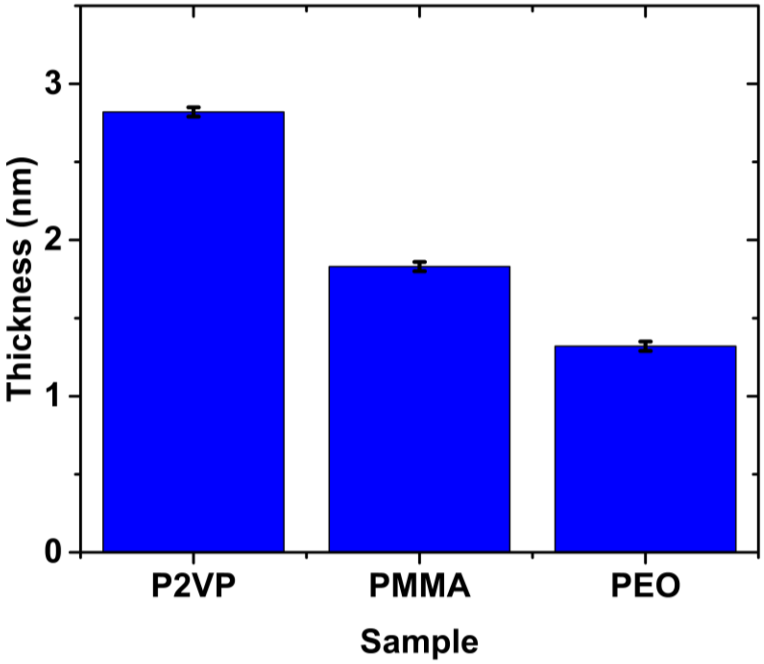

Figure 5.11 Ellipsometry results of the Al_2O_3 *films fabricated using the infiltrated PMMA, P2VP and PEO polymers. These data show good agreement with previous data showing that the P2VP film fabricated the thickest resultant oxide film.*

5.4 Conclusions

A comparison of the Al uptake of the polymers PMMA, P2VP and PEO has been reported, as part of a VPI infiltration process. Firstly, through the use of ellipsometry and XRR it was shown that the PMMA resulted in the thickest and densest polymer film followed by the films made using P2VP and then PEO. As the parameters for the solutions used for the brush fabrication were the same, this showed that this variation was completely polymer dependent indicating the potential that the PMMA polymer has for significant Al uptake.

Through the use of HAXPES it was shown that each of the polymer films were successfully infiltrated with Al post VPI processing. This was demonstrated through the fitting of the C1s and O1s spectra for each of the polymer films as well as the N1s in the case of the P2VP brush. Through this fitting the infiltration mechanisms for each of the polymers was determined. In the case of the PMMA, through the reduction of C=O bond signals in both the C1s and O1s spectra it was clear that the TMA precursor interacted with the polymer through the breaking of this bond. For the P2VP film the appearance of Al-N bonds in the post infiltrated N1s spectrum showed that the TMA bonded with the nitrogen in the pyridine ring of the polymer through its lone pair of electrons. Finally, in the case of PEO, the contribution of Al-O bonds within the post infiltrated film O1s spectra shows that the TMA bonded with the lone pair of electrons on the oxygen atom within the polymer ethoxy group. Al1s spectra showed that the P2VP film had the largest Al uptake post infiltration. This was concluded to be due to the efficient infiltration mechanism of the P2VP compared to that of the PMMA. Because the P2VP and PEO films had similar infiltration mechanisms it was also concluded that the thickness and density of the brush had only a small contributing factor, since the P2VP was both thicker and denser than the PEO film.

Once infiltrated the films were exposed to an ICP O_2 plasma process to both remove the polymer brushes and oxidise the infiltrated Al enabling fabrication of Al_2O_3 thin films. Through the fitting of the O1s HAXPES data it was shown that the infiltrating polymer used had no effect on the chemical composition of the resultant oxide thin films. Finally, through the analysis of the Al1s HAXPES signal post polymer removal, as well as by the use of ellipsometry, it was shown that the P2VP brush layer fabricated the thickest resultant Al_2O_3 film, followed by the PMMA brush, and then the PEO brush.

Overall, the conclusion from these results is that the P2VP brush layer had the highest Al uptake as well as enabling the fabrication of the thickest resultant oxide film. Due to its higher χ value with PS in a BCP system this makes P2VP a very suitable polymer candidate for use in fabricating nanostructures and patterned substrates.

5.5 References

(1) Kressler, J.; Higashida, N.; Shimomai, K.; Inoue, T.; Ougizawa, T. Temperature Dependence of the Interaction Parameter between Polystyrene and Poly(Methyl Methacrylate). *Macromolecules* **1994**, *27* (9), 2448–2453. https://doi.org/10.1021/MA00087A013.

(2) Alberda Van Ekenstein, G. O. R.; Meyboom, R.; Ten Brinke, G.; Ikkala, O. Determination of the Flory-Huggins Interaction Parameter of Styrene and 4-Vinylpyridine Using Copolymer Blends of Poly(Styrene-Co-4-Vinylpyridine) and Polystyrene. **2000**. https://doi.org/10.1021/ma992118.

(3) Frielinghaus, H.; Hermsdorf, N.; Almdal, K.; Mortensen, K.; Messé, L.; Corvazier, L.; Fairclough, J. P. A.; Ryan, A. J.; Olmsted, P. D.; Hamley, I. W. Micro- vs. Macro-Phase Separation in Binary Blends of Poly(Styrene)-Poly(Isoprene) and Poly(Isoprene)-Poly(Ethylene Oxide) Diblock Copolymers. *Europhys. Lett.* **2001**, *53* (5), 680. https://doi.org/10.1209/EPL/I2001-00205-7.

(4) Snelgrove, M.; McFeely, C.; Shiel, K.; Hughes, G.; Yadav, P.; Weiland, C.; Woicik, J. C.; Mani-Gonzalez, P. G.; Lundy, R.; Morris, M. A.; McGlynn, E.; O'Connor, R. Analysing Trimethylaluminum Infiltration into Polymer Brushes Using a Scalable Area Selective Vapor Phase Process. *Mater. Adv.* **2021**, *2* (2), 769–781. https://doi.org/10.1039/d0ma00928h.

(5) Biswas, M.; Libera, J. A.; Darling, S. B.; Elam, J. W. New Insight into the Mechanism of Sequential Infiltration Synthesis from Infrared Spectroscopy. *Chem. Mater.* **2014**, *26* (21), 6135–6141. https://doi.org/10.1021/CM502427Q.

(6) Pielichowski, K.; Flejtuch, K. Non-Oxidative Thermal Degradation of Poly(Ethylene Oxide): Kinetic and Thermoanalytical Study. *J. Anal. Appl. Pyrolysis* **2005**, *73* (1), 131–138. https://doi.org/10.1016/j.jaap.2005.01.003.

(7) NSLS-II | Beamline 7-ID-2 (SST2) Spectroscopy Soft and Tender 2 https://www.bnl.gov/nsls2/beamlines/beamline.php?r=7-ID-2 (accessed May 27, 2023).

(8) Snelgrove, M.; Mani-Gonzalez, P. G.; Bogan, J.; Lundy, R.; Rueff, J. P.; Hughes, G.; Yadav, P.; McGlynn, E.; Morris, M.; O'Connor, R. Hard X-Ray Photoelectron Spectroscopy Study of Copper Formation by Metal Salt Inclusion in a Polymer Film. *J. Phys. D. Appl. Phys.* **2019**, *52* (43). https://doi.org/10.1088/1361-6463/AB35B2.

(9) Pletincx, S.; Marcoen, K.; Trotochaud, L.; Fockaert, L.-L.; Mol, J. M. C.; Head, A. R.; Karslioğlu, O.; Bluhm, H.; Terryn, H.; Hauffman, T. Unravelling the Chemical Influence of Water on the PMMA/Aluminum Oxide Hybrid Interface In Situ. https://doi.org/10.1038/s41598-017-13549-z.

(10) Furlan, A.; Jansson, U.; Lu, J.; Hultman, L.; Magnuson, M. Structure and Bonding in Amorphous Iron Carbide Thin Films. *J. Phys. Condens. Matter* **2015**, *27* (4), 045002. https://doi.org/10.1088/0953-8984/27/4/045002.

(11) Miller, D. J.; Biesinger, M. C.; McIntyre, N. S. Interactions of CO2 and CO at Fractional Atmosphere Pressures with Iron and Iron Oxide Surfaces: One Possible Mechanism for Surface Contamination? *Surf. Interface Anal.* **2002**, *33* (4), 299–305. https://doi.org/10.1002/SIA.1188.

(12) Bogan, J.; Lundy, R.; McCoy, A.; O'Connor, R.; Byrne, C.; Walsh, L.; Casey, P.; Hughes, G. In-Situ Surface and Interface Study of Atomic Oxygen Modified Carbon Containing Porous Low-κ Dielectric Films for Barrier Layer Applications. *J. Appl. Phys.* **2016**, *120* (10). https://doi.org/10.1063/1.4962371/143014.

(13) Byrne, C.; Brennan, B.; McCoy, A. P.; Bogan, J.; Brady, A.; Hughes, G. In Situ XPS Chemical Analysis of MnSiO3 Copper Diffusion Barrier Layer Formation and Simultaneous Fabrication of Metal Oxide Semiconductor Electrical Test MOS Structures. *ACS Appl. Mater. Interfaces* **2016**, *8* (4), 2470–2477. https://doi.org/10.1021/ACSAMI.5B08044/ASSET/IMAGES/MEDIUM/AM-2015-08044M_0013.GIF.

(14) Oxygen | XPS Periodic Table - IE.

(15) Snelgrove, M.; McFeely, C.; Mani-Gonzalez, P. G.; Lahtonen, K.; Lundy, R.; Hughes, G.; Valden, M.; McGlynn, E.; Yadav, P.; Saari, J.; Morris, M. A.; O'Connor, R. Aluminium Oxide Formation via Atomic Layer Deposition Using a Polymer Brush Mediated Selective Infiltration Approach. *Appl. Surf. Sci.* **2020**, *515*. https://doi.org/10.1016/j.apsusc.2020.145987.

(16) Gabka, G.; Bujak, P.; Giedyk, K.; Kotwica, K.; Ostrowski, A.; Malinowska, K.; Lisowski, W.; Sobczak, J. W.; Pron, A. Ligand Exchange in Quaternary Alloyed Nanocrystals – a Spectroscopic Study. *Phys. Chem. Chem. Phys.* **2014**, *16* (42), 23082–23088. https://doi.org/10.1039/C4CP03850A.

(17) Barber, M.; Connor, J. A.; Guest, M. F.; Hillier, I. H.; Schwarz, M.; Stacey, M. Bonding in Some Donor–Acceptor Complexes Involving Boron Trifluoride. Study by Means of ESCA and Molecular Orbital Calculations. *J. Chem. Soc. Faraday Trans. 2 Mol. Chem. Phys.* **1973**, *69* (0), 551–558. https://doi.org/10.1039/F29736900551.

(18) Tien, H. W.; Huang, Y. L.; Yang, S. Y.; Wang, J. Y.; Ma, C. C. M. The Production of Graphene Nanosheets Decorated with Silver Nanoparticles for Use in Transparent, Conductive Films. *Carbon N. Y.* **2011**, *49* (5), 1550–1560. https://doi.org/10.1016/J.CARBON.2010.12.022.

(19) Beamson, G.; Briggs, D. High Resolution XPS of Organic Polymers: The Scienta ESCA300 Database. *J. Chem. Educ.* **1992**, *70* (1), A25. https://doi.org/10.1021/ED070PA25.5.

(20) Watts, J. F. High Resolution XPS of Organic Polymers: The Scienta ESCA 300 Database. G. Beamson and D. Briggs. 280pp., £65. John Wiley & Sons, Chichester, ISBN 0471 935921, (1992). *Surf. Interface Anal.* **1993**, *20* (3), 267–267. https://doi.org/10.1002/SIA.740200310.

(21) Dalmau, R.; Collazo, R.; Mita, S.; Sitar, Z. X-Ray Photoelectron Spectroscopy

Characterization of Aluminum Nitride Surface Oxides: Thermal and Hydrothermal Evolution. *J. Electron. Mater.* **2007**, *36* (4), 414–419. https://doi.org/10.1007/S11664-006-0044-X/METRICS.

(22) Liao, J. X.; Xia, L. F.; Sun, M. R.; Liu, W. M.; Xu, T.; Yang, C. R.; Chen, H. W.; Fu, C. L.; Leng, W. J. Structural Characteristics of 2024 Aluminum Alloy Plasma-Based Ion Implanted with Nitrogen Then Titanium. *Appl. Surf. Sci.* **2005**, *240* (1–4), 71–76. https://doi.org/10.1016/j.apsusc.2004.06.145.

(23) Mani-Gonzalez, P. G.; Snelgrove, M.; Rueff, J. P.; Lundy, R.; Yadav, P.; Bogan, J.; O’Connor, R.; Morris, M.; Hughes, G. Analysis of Al and Cu Salt Infiltration into a Poly 2-Vinylpyridine (P2vP) Polymer Layer for Area Selective Deposition Applications. *J. Phys. D. Appl. Phys.* **2020**, *53* (11). https://doi.org/10.1088/1361-6463/AB60E8.

(24) Snelgrove, M.; Zehe, C.; Lundy, R.; Yadav, P.; Rueff, J.-P.; O’connor, R.; Bogan, J.; Hughes, G.; Mcglynn, E.; Morris, M.; Mani-Gonzalez, P. G. Surface Characterization of Poly 2-Vinylpyridine-A Polymer for Area Selective Deposition Techniques.

(25) Louette, P.; Bodino, F.; Pireaux, J.-J. Poly(Ethylene Oxide) (PEO) XPS Reference Core Level and Energy Loss Spectra. *Surf. Sci. Spectra* **2005**, *12* (1), 59–63. https://doi.org/10.1116/11.20050912.

(26) Bao, W.; Zhao, L.; Zhao, H.; Su, L.; Cai, X.; Yi, B.; Zhang, Y.; Xie, J. Vapor Phase Infiltration of ZnO Quantum Dots for All-Solid-State PEO-Based Lithium Batteries. *Energy Storage Mater.* **2021**, *43*, 258–265. https://doi.org/10.1016/j.ensm.2021.09.010.

(27) Zhang, D.; Li, L.; Wu, X.; Wang, J.; Li, Q.; Pan, K.; He, J. Research Progress and Application of PEO-Based Solid State Polymer Composite Electrolytes. *Front. Energy Res.* **2021**, *9*. https://doi.org/10.3389/FENRG.2021.726738/FULL.

(28) Fenton, D. E.; Parker, J. M.; Wright, P. V. Complexes of Alkali Metal Ions with Poly(Ethylene Oxide). *Polymer (Guildf).* **1973**, *14* (11), 589. https://doi.org/10.1016/0032-3861(73)90146-8.

6 Conclusions and Future Work

6.1 Conclusions

The main conclusions drawn from Chapters 3 – 5 provide a solid foundation for further investigation into the fabrication, infiltration and characterisation of polymer brushes, which is also applicable to BCP research. The main findings of this work include:

Confirmation of the rapid grafting to method for polymer brush fabrication. All results produced by this work show that the grafting to method is a suitable route for the fabrication of highly uniform polymer brushes such as PS and PMMA. Polymer brushes performed as required both for area activation and deactivation. This is relevant as the grafting to method is significantly faster than current ASD methods such as SAMs.

Validation that the solution concentration and molecular weight of the polymers PS and PMMA has an effect of the resulting brush thickness. The way in which the weight percentage and molecular weight of the polymers PMMA and PS effects the resultant thickness of the polymer brush was a key finding of Chapter 3. It has been shown that the disadvantages of the grafting to method are its inability to control thickness and lack of suitability for fabrication of thicker polymer brushes. Through the use of ellipsometry, GA-ATR-FTIR and AFM it was shown that an increase in the concentration of the fabricating solution and molecular weight of the polymers PS and PMMA led to a thicker polymer brush using the grafting to method. It was also shown that by varying the solution concentration one can achieve varying polymer brush thicknesses allowing better thickness control.

Demonstration of the development of a gentle O_2 plasma process for the hydroxy functionalisation of PS brushes. Another key finding within Chapter 3 was to further investigate methods to increasing polymer brush thickness while implementing the grafting to approach. An O_2 plasma process was developed using a Henniker bench top plasma system which hydroxy functionalised the surface of a PS brush with the intention of applying a second layer of PS using the grafting to method. It was shown through the use of contact angle that the PS brush was able to be functionalised using a low power 1 second plasma process. Using ellipsometry and AFM it was determined that this gentle process caused little to no damage to the PS film which was a concern because O_2 plasmas are used for the removal of polymer brushes. Following this a second layer of PS was applied however, using ellipsometry, no significant increase in the brush thickness was seen leading to the conclusion that this method of thicker brush fabrication was unsuccessful.

Experimental proof that the thickness of the polymer brush materials PMMA and PS has an effect on the brush layer infiltration and blocking efficacy, respectively. The main focus of Chapter 4 was a study of the way in which the polymer brush thickness effected its infiltrating and blocking properties. It was shown in the case of the PMMA films, through the use of an Al based VPI process, that the thickness of the brush had an effect on the amount of Al uptake. Through the use of HAXPES it was confirmed that the thicker polymer brushes had a slightly larger Al uptake, however post polymer removal it was seen that the thicker fabricating brush led to a thicker resultant oxide. Similarly, in the case of the PS films, through the use of an HfO_2 ALD process, using XPS it was shown that the thicker PS brushes were more effective at blocking an ALD process. Both studies show a clear relationship between the thickness of the polymer brush layers and their infiltrating or blocking properties.

Comparison of a UV ozone or ICP O_2 plasma process for the removal of PMMA brushes and Al oxidation. Chapter 4 also reported a detailed comparison of a UV ozone and an ICP O_2

plasma-based process for the removal of polymer brushes. Through the use of HAXPES both processes were shown to be successful at removing the PMMA films. However, it was seen that the plasma-based process resulted in thicker Al_2O_3 films post polymer removal and because this process is significantly faster than the UV ozone process it is considered superior, especially for the use in industrial settings.

Verification that the polymer used for the fabrication of Al_2O_3 thin films effects the resultant thickness of that film. Chapter 5 reports a detailed comparison of the Al uptake within the polymer brush materials P2VP, PMMA and PEO, through the exposure of these films to a VPI process. Using HAPXES it was shown that the P2VP films had the largest uptake of Al, followed by the PMMA films and finally the PEO films. It was proposed that this was due both to an efficient infiltration mechanism via the interaction of the TMA precursor with the nitrogen lone pair, and the overall thickness and density of the P2VP. Using an ICP O_2 plasma these brushes were removed and the thickness and chemical composition of the resultant oxide films were determined. It was seen that the fabricating polymer had no effect on the Al_2O_3 chemical state however it was shown that the resultant oxide film fabricated using the P2VP brush was the thickest. Because P2VP is known for its ability to create small nanostructures within a BCP system this was a significant and favourable result since it was clearly the most efficient brush layer in terms of infiltration.

6.2 Future Work

Based on the results and the associated conclusions from chapters 3 – 5, there are several interesting areas for potentially fruitful further research. The first of these is further investigations into higher χ value polymers. It was shown that P2VP had a larger amount of infiltrating material uptake compared to PEO, which also has a higher χ value with PS than does PMMA. While this is an important result P2VP has been shown to have its limitations. For example, it was noted at the AMBER Institute in Trinity College Dublin that higher molecular weight P2VP material (i.e. above 6K) results in the formation of crystal islanding instead of a coherent film. This was attributed to weak intermolecular interactions or π-π stacking between the pyridine molecules inside the solution. This limits the ultimate thickness that the P2VP films can achieve. It is for this reason that further investigation into the infiltration of higher χ value polymers such as poly-DL-lactide is required. This may open up further avenues for the fabrication of smaller nanostructures within a BCP system than that currently reported using PMMA.

Similar to the suggestion above for further investigation into more suitable infiltrating polymers, more work should be carried out on the identification and study of other polymers (as opposed to PS) suitable for blocking deposition. An example of another polymer suitable for the inhibition of material deposition is polynorbornene. As previously discussed, the Flory Huggins parameter is influenced by all polymers present within the BCP system. This means that it not only is altered through the variation of the infiltrating polymer but also the blocking polymer, allowing for varying feature size to be achieved through changing the polymer combinations. Identifying and studying the properties of more blocking polymers allows for a larger number of combinations to be made within a BCP structure, thus potentially allowing for more control over the self-assembled nanostructure size.

Finally, the way in which the polymer thickness as well as the polymer type influences the electrical properties of the resultant oxide film should be studied. This work showed the effect that these parameters had on the thickness of the resulting oxide film. However, it is important to know the electrical characteristics of these films because one of the main applications of these fabricated oxides within the semiconductor industry is their use as a gate oxide in MOSFET devices. It is for this reason that the electrical characterisation, such as IV and CV sweeps for the determination of the leakage currents and breakdown voltages of these films is proposed, to develop a better understanding of the effect that the polymer thickness as well as the polymer type has on the key device-relevant properties of the resultant oxide.